

**GALVANIC CORROSION POTENTIAL AND MATERIAL AND BOND
PROPERTIES OF
TITANIUM REINFORCING BARS**

by

Shawn LeRoy Platt

B.S. in Civil Engineering, University of Pittsburgh, 2014

M.S. in Civil Engineering, University of Pittsburgh, 2015

Submitted to the Graduate Faculty of
Swanson School of Engineering in partial fulfillment
of the requirements for the degree of
Doctor of Philosophy

University of Pittsburgh

2018

UNIVERSITY OF PITTSBURGH
SWANSON SCHOOL OF ENGINEERING

This dissertation was presented

by

Shawn LeRoy Platt

It was defended on

March 19, 2018

and approved by

Andrew Bunger, PhD, Assistant Professor

Department of Civil and Environmental Engineering

Julie Vandebossche, PhD, Associate Professor

Department of Civil and Environmental Engineering

Brahim Benmokrane, PhD, Professor

University of Sherbrooke, Department of Civil Engineering

Dissertation Director: Kent A. Harries, PhD

Bicentennial Board of Visitors Fellow, Associate Professor

Department of Civil and Environmental Engineering

Copyright © by Shawn LeRoy Platt

2018

**GALVANIC CORROSION POTENTIAL AND MATERIAL AND BOND
PROPERTIES OF
TITANIUM REINFORCING BARS**

Shawn LeRoy Platt, PhD.

University of Pittsburgh, 2018

The use of titanium reinforcing bars for concrete has been proposed. The primary advantage of titanium is its corrosion resistance enhancing concrete element performance and permitting reduced cover in near-surface mounted applications. Like steel, titanium exhibits an elastic behaviour to a proportional limit, a definable yield value, and exhibits a great deal of ductility. Grade 5 titanium exhibits yield strength approximately twice that of ASTM A615 steel and an extensional modulus about 55% of steel.

In this study, the effects of coupling titanium and A615 steel in concrete are investigated considering the potential for galvanic corrosion. This study provides evidence that there are no apparent galvanic effects of coupling titanium and A615 reinforcing bars. The study goes on to characterize geometric and material and fatigue properties of titanium reinforcing bars. Bond characteristics of the titanium bars were assessed using ASTM D7913 pull-out tests, ASTM A944 beam-end tests and concrete prism tension tests. The nature of reinforcing bar bond to concrete is such that deformed bars exhibit very similar patterns of bond stress-slip behaviour. Provided adequate deformations are provided, the bond-slip relationship is dominated by concrete behaviour. The bond performance of the titanium bars was similar to that of A615 bars and, as expected, affected by the rib ratio. The bond behaviour of titanium is similar to that of

steel bars and the calculated development lengths are essentially in the ratio of yield strengths of the materials. Crack widths are proportional to modular ratio, while spacing is inversely proportional to the stiffness of the initial bond-slip response. Therefore, a lower modulus bar will exhibit larger crack widths unless bond characteristics are improved proportionally.

An analytical study is presented to evaluate current design paradigms in relation the properties of titanium reinforcing bars. A combination of ACI 318 provisions for strength and ACI 440.1R provisions for serviceability are necessary when designing with titanium. The resulting hybrid design approach is illustrated in a series of benchmark flexural designs. Recommendations and limitations for the design of titanium reinforced flexural members are presented.

TABLE OF CONTENTS

ACKNOWLEDGMENTS	xv
NOMENCLATURE.....	xvi
1.0 INTRODUCTION	1
1.1 DESIGN WITH TITANIUM REINFORCING BARS	1
1.2 ORGANIZATION OF THESIS	3
1.3 DISCLAIMER	5
2.0 GALVANIC CORROSION IN REINFORCED CONCRETE	6
2.1 GALVANIC CORROSION OF STEEL COUPLED WITH TITANIUM.....	9
2.1.1 Objective of Study	11
2.2 GALVANIC CORROSION TEST PROGRAM.....	12
2.2.1 Test Specimens	12
2.2.2 Materials.....	14
2.2.3 Conditioning Protocol	16
2.2.4 Specimen Monitoring	20
2.2.4.1 Half-cell potential (based on ASTM C876 10.3).....	20
2.2.4.2 Macrocouple Current (based on ASTM G102-89).....	22
2.2.4.3 Measurement of Reinforcing Bar Mass Loss	23
2.3 GALVANIC CORROSION TEST RESULTS	23
2.3.1 Prior to Conditioning	23
2.3.2 During Conditioning.....	25
2.3.2.1 Half Cell measurements.....	25

2.3.2.2	Macrocouple measurements.....	28
2.3.3	Following Conditioning.....	31
2.3.4	Mass Loss of Electrically Connected Bars	33
2.4	SUMMARY OF GALVANIC CORROSION TEST PROGRAM.....	34
3.0	TITANIUM REINFORCING BAR MECHANICAL AND GEOMETRIC CHARACTERIZATION	36
3.1	MECHANICAL PROPERTIES OF REINFORCING BARS	36
3.1.1	Experimentally determined mechanical behavior of bars in this study ...	38
3.1.2	Fatigue Behavior	40
3.1.3	Ductility Characterization	43
3.2	GEOMETRIC CHARACTERIZATION.....	46
3.2.1	Cross Sectional Area	48
3.2.2	Deformation Geometry	49
3.2.3	Lug Height Variation	51
3.2.4	Variation of Lug Geometry Along Single 3.66 m Length of Bar	53
3.2.5	Discussion of Observed Deformations	54
3.3	SUMMARY OF MATERIAL AND GEOMETRIC CHARACTERIZATION OF TITANIUM REINFORCING BARS	55
4.0	BOND CHARACTERIZATION.....	57
4.1	EFFECTS OF RIB GEOMETRY ON BOND	61
4.2	BOND CHARACTERIZATION TEST PROGRAM	66
4.3	PULL-OUT TESTING.....	67
4.3.1	Test Specimens.....	69
4.3.2	Test Set-up and Protocol.....	70
4.3.3	Test Results	72
4.3.4	Bar X and Bar Y Results.....	79

4.3.5	Discussion and Summary of Pull-out Test Results	81
4.4	BEAM END TESTING	82
4.4.1	Test Specimens	83
4.4.2	Test Set-up and Protocol.....	84
4.4.3	Test Results	86
4.4.4	Discussion and Summary of Beam-End Test	93
4.5	PRISM TENSION TESTING.....	95
4.5.1	Test Specimens and Test Method.....	97
4.5.2	Prism Test Results	98
4.5.3	Discussion and Summary of Prism Test	99
4.6	SUMMARY OF BOND CHARACTERIZATION OF TITANIUM REINFORCING BARS.....	102
4.6.1	Bond and Development Length Recommendation for Titanium Bars...	103
5.0	NSM TITANIUM REINFORCED SLAB TESTS.....	104
5.1.1	Preparation of test slabs.....	108
5.1.2	Testing of slabs.....	112
5.1.3	Slab Concrete Properties	114
5.1.4	Test Results	116
5.1.4.1	Bar Slip of Slab TiNSM-1.....	126
5.1.4.2	Slab TiNSM-2	129
5.1.4.3	Stapled slabs TiNSM-3 and TiNSM-4.....	132
5.2	SUMMARY OF SLAB TESTS.....	136
6.0	ANALYTICAL AND BENCHMARKING STUDY.....	138
6.1	DESIGN WITH TITANIUM REINFORCING BARS	142
6.1.1	Design with Titanium	143
6.1.2	Design for Flexural Strength	144

6.1.2.1	Material Resistance Factors, ϕ	144
6.1.3	Design for Serviceability	145
6.1.3.1	Minimum Reinforcement Requirements and Crack Control.....	146
6.1.3.2	Minimum Depth Recommendations.....	148
6.1.3.3	Calculations of Deflections	149
6.2	BENCHMARK DESIGN EXAMPLES	150
6.2.1	One-way Slab Design.....	151
6.2.1.1	Slab Design 1.....	151
6.2.1.2	Slab Design 2.....	151
6.2.1.3	Discussion of One-way Slab Designs	152
6.2.2	Simple Flexural Beam Design.....	156
6.2.3	Repair/ Retrofit Examples	159
6.2.3.1	NSM Retrofit of Simple Span Beam.....	159
6.3	COST COMPARISON.....	163
7.0	CONCLUSIONS AND RECOMMENDATIONS.....	165
7.1	CONCLUSIONS	165
7.1.1	Galvanic Corrosion Study.....	166
7.1.2	Titanium Bar Geometric and Material Properties.....	166
7.1.3	Bond Characteristics of Titanium Bars.....	167
7.1.4	NSM Titanium Reinforcement of Slabs.....	169
7.2	DESIGN OF TITANIUM REINFORCED CONCRETE	170
7.2.1	Recommendations for ACI 318-compliant design using titanium reinforcing bars	171
7.2.1.1	NSM Applications	172
	REFERENCES CITED.....	173

LIST OF TABLES

Table 2.1 Behavior of Steel-Titanium galvanic couples in marine environments.....	11
Table 2.2 Test matrix	14
Table 2.3 Typical weekly conditioning schedule	18
Table 2.4 Steel bar mass loss	32
Table 3.1 Mechanical properties of reinforcing bars	39
Table 3.2 Fatigue test results	42
Table 3.3 Geometry of #5 titanium bars	48
Table 3.4 Deformation (lug) geometry of #5 A615 steel and titanium bars.....	50
Table 3.5 Measured lug heights for titanium bars	53
Table 3.6 Variation of lug geometry along length of bars X and Y	54
Table 4.1 Concrete batch mix designs and material properties	67
Table 4.2 Pull-out test matrix indicating number of samples tested.....	69
Table 4.3 Summary of pull-out test	73
Table 4.4 Summary of pull-out test for Bars X and Y	80
Table 4.5 Beam-end test matrix indicating number of samples tested	83
Table 4.6 Summary of beam-end test	87
Table 4.7 Summary of avg. bond stress ¹ determined at slip of 0.009 mm	94
Table 4.8 Summary of maximum avg. bond stress ¹ and corresponding development length from Equation 2	94

Table 4.9 Crack history, widths and spacing for prism tension tests.....	100
Table 5.1 Demonstration tests.....	106
Table 5.2 Concrete slab properties.....	115
Table 5.3 Summary of tested slabs	117
Table 5.4 Summary of predicted capacities of NSM-reinforced slabs	119
Table 6.1 Design paradigms for steel and GFRP-reinforced concrete	139
Table 6.2 Proposed calculations for the average effective moment of inertia.....	141
Table 6.3 Reinforcing bar properties used in benchmark designs	143
Table 6.4 Comparable designs for one-way slab 1 (Section 6.2.1.1)	154
Table 6.5 Comparable designs for one-way slab 2 (Section 6.2.1.2)	155
Table 6.6 Comparable designs for rectangular beam (Section 6.2.2).....	158
Table 6.7 Comparable NSM designs for rectangular beam retrofit (Section 6.2.3.1)	161
Table 6.8 Cost comparison for typical bridge deck.	164

LIST OF FIGURES

Figure 2.1 Examples of stress cells [Askeland and Wright 2015].....	7
Figure 2.2 Corrosion potentials in flowing sea water [Atlas Steels 2010]	10
Figure 2.3 Minimum dimensions of NSM ‘slots’ [ACI 440.2R-17 Fig. 14.3].....	12
Figure 2.4 Specimens prior to conditioning.....	13
Figure 2.5 Specimens in conditioning tank (photo taken before conditioning begun).....	17
Figure 2.6 Typical weekly temperature/RH log	18
Figure 2.7 Temperature/RH log.....	19
Figure 2.8 Half-cell potential equipment and testing.....	21
Figure 2.9 Grouping of specimens by macrocouple current prior to start of conditioning	25
Figure 2.10 Half-cell potential history showing average and one standard deviation.....	26
Figure 2.11 Half-cell potential values of segmented bars in concrete (Poursaee 2011).....	28
Figure 2.12 Average macrocouple history.....	29
Figure 2.13 Macrocouple current following conditioning.....	30
Figure 2.14 Average mass loss over 152 mm length due to corrosion of all specimens	32
Figure 2.15 Mass loss for 12.6 mm representative sections of ASTM A615 bars	33
Figure 2.16 Interaction plot for current.....	35
Figure 3.1 Idealized characteristics of typical stress-strain curve [Kelly et al. 2014]	38
Figure 4.1 Transfer of forces from concrete to reinforcement.....	58
Figure 4.2 Descriptions of lug angles and spacing [Rehm 1961].....	61

Figure 4.3 Rib ratios of bars used in present study.....	63
Figure 4.4 The distribution of tangential tensile stresses [Tepfers 1973].....	64
Figure 4.5 Description of the lug angles influence on radial pressure [Vos 1983]	65
Figure 4.6 ASTM D7913-14 test specimens.....	70
Figure 4.7 ASTM D7913-14 test set-up	71
Figure 4.8 Average bond stress-slip relationships	75
Figure 4.9 Bond stress-slip relationships for specimens tested with batch 1 concrete.....	76
Figure 4.10 Bond stress-slip relationships for specimens tested with batch 2 concrete.....	76
Figure 4.11 Bond stress-slip relationships for specimens tested with batch 3 concrete.....	77
Figure 4.12 Bond stress-slip relationships for nominal and measured bar geometries	78
Figure 4.13 Normalized bond stress-slip relationships.....	79
Figure 4.14 Bond stress-slip relationships for five specimens from Bar X.....	81
Figure 4.15 Summary of bond stress-slip relationships for five specimens from Bar X.....	81
Figure 4.16 ASTM A944-10 test specimen details and fabrication.....	84
Figure 4.17 ASTM A944-10 test set-up	85
Figure 4.18 Beam-end test results.....	89
Figure 4.19 Radial cracking at loaded face.....	90
Figure 4.20 Beam-end crack patterns and progression.....	92
Figure 4.21 Crack development and internal strains in direct tension test	96
Figure 4.22 Prism specimens following testing showing crack patterns	100
Figure 5.1 Details of laboratory control specimen and test arrangement [McCabe 2013]	104
Figure 5.2 Cross sections and elevations of repaired slabs.....	107
Figure 5.3 Preparation of straight bar NSM repair specimens.....	110
Figure 5.4 Preparation of staple NSM repair specimens	111
Figure 5.5 Test Set-Up and Instrumentation [adapted from McCabe et al. 2014].....	113

Figure 5.6 Summary of Moment-Curvature results from slab flexure tests	118
Figure 5.7 Summary of Moment-Curvature results with RESPONSE predicted results	120
Figure 5.8 Summary of Slab A test results reproduced from McCabe [2013]	121
Figure 5.9 Summary of test results for TiNSM-1	122
Figure 5.10 Summary of test results for TiNSM-2	123
Figure 5.11 Summary of test results for TiNSM-3	124
Figure 5.12 Summary of test results for TiNSM-4	125
Figure 5.13 Crack distribution on the soffit of TiNSM-1	127
Figure 5.14 Bond performance of single straight bar NSM in Slab TiNSM-1	128
Figure 5.15 TiNSM-2 (4- #5 straight titanium bars).....	130
Figure 5.16 TiNSM-2 midspan (4 - #5 straight titanium bars).....	131
Figure 5.17 TiNSM-3 (1 - #5 titanium staple).....	133
Figure 5.18 TiNSM-4 (4 - #5 titanium staples)	134
Figure 5.19 Generalized capacity envelope of the damaged slab with and without staple repair	136

ACKNOWLEDGMENTS

Journeys are meant to be savored and enjoyed. This journey has been special in so many ways; in part due to the acceptance that a journey is never truly over. As one ends, another begins. Along the way we gather moments in time that help to shape our perceptions and focus our goals. These moments are ever changing and should never be taken for granted.

I would like to thank Dr. Kent Harries for his unwavering support and friendship during this journey. He has helped to mentor and guide me through the years and thank you will never be enough. He has helped to sculpt this journey as well as providing me with the tools to begin the next one. I would also like to thank the committee members for their time and effort. Their commitment to the success of this research has been greatly appreciated.

A special thanks to my family Shantel and Logan, as they have stayed by my side, motivating me at every turn. Their endearing love and support has meant the world to me. The support from faculty members has truly been wonderful and my deepest appreciation is extended to Dr. John Oyler for his friendship and guidance over the years. He has been a beacon for many students and a cherished friend and colleague. Friends and colleagues like Charles Hager and Tianqiao Liu, who were instrumental in laboratory testing and manufacturing, and were invaluable during this research providing both logistical and moral support for which I will be forever grateful.

I would also like to thank Perryman Co. (Washington PA) without whom this journey would have been quite different. Their support is greatly appreciated.

NOMENCLATURE

A_b	Area of the reinforcing bar
$A_{s,min}$	Minimum area of longitudinal reinforcement
b_w	Web width
b_w	Web width
c_b	Smaller of: center of bar to surface of concrete
C_E	Environmental reduction factor for various fiber types and exposure conditions
d_{agg}	Maximum aggregate size
d_b	Bar diameter
E_c	Elastic modulus of the concrete
E_f	Elastic modulus of the FRP bars
E_R	Elastic modulus of the reinforcement
E_s	Elastic modulus of the steel bars
E_t	Elastic modulus of the titanium bars
e_{th}	Thermal coefficient of expansion
f_{fu}^*	(FRP) Guaranteed tensile strength
f_c'	Compressive strength of concrete
f_f	Stress in FRP reinforcement in tension
f_F	Design stress in FRP tension reinforcement at ultimate limit state
f_{fe}	(FRP) Bar stress that can be developed for embedment length
f_{fr}	(FRP) Required bar stress
f_{fu}	(FRP) Design tensile strength considering reductions for service environment
f_r	Modulus of rupture
f_u	Ultimate strength of the reinforcement
f_{us}	Ultimate strength of the steel reinforcement
f_{ut}	Ultimate strength of the titanium reinforcement
f_y	Yield strength of the reinforcement
f_{ys}	Yield strength of the steel reinforcement
f_{yt}	Yield strength of the titanium reinforcement
I	Moment of inertia of the cross section about a designated axis
I_{cr}	Moment of inertia of the fully cracked transformed section

I_e	Effective moment of inertia
I_g	Moment of inertia of the gross cross section
k_1	Bar-location factor
k_2	Concrete density factor
k_3	Bar size factor
k_4	Bar fibre factor
k_5	Bar surface profile factor
l_b	Bonded length, the length of bar in contact with the concrete
l_d	Development length, the length required to achieve yield
l_e	Embedded (bonded) length, the length of bar in contact with the concrete
M_a	Applied moment at the critical section
M_{cr}	Cracking moment
n	Number of bars being developed along a plane of splitting
P_u	Maximum tensile load
s	Maximum center-to-center spacing of transverse reinforcement within l_d
ν	Poisson ratio
w_c	Weight of concrete in
ε	Strain
ε_{cu}	Assumed maximum useable compression strain in the concrete (0.003)
ε_{fu}^*	Guaranteed/tested maximum strain
ε_t	Tensile strain in extreme layer of longitudinal tension reinforcement
ε_{yR}	Yield strain of the reinforcement
λ	Taken as 1 for normal weight concrete
μ_{avg}	Average bond stress
ρ	Density
ρ_b	Balanced reinforcement ratio
ρ_R	Reinforcement ratio
Φ_{cr}	Section curvature at cracking
ψ_e	Epoxy-coating factor
ψ_s	Bar size factor
ψ_t	Bar-location factor

This dissertation is presented primarily with SI units except where maintaining native US units is consistent with cited source material or is considered critical to understanding or presentation. Reinforcing bar sizes are given exclusively by their US designation (i.e., #X, where X is eighths of inch nominal diameter). This avoids confusion with ‘soft’ and ‘hard’ SI conversions of bars sizes. The following are the nominal SI geometric properties of US bar sizes

Bar Size	nominal diameter		cross section area	
	in.	mm	in ²	mm ²
#3	0.375	9.52	0.11	71
#4	0.500	12.70	0.20	129
#5	0.625	15.86	0.31	200
#6	0.750	19.00	0.40	284
#7	0.875	22.22	0.60	387
#8	1.000	25.40	0.79	509
#9	1.125	28.58	1.00	645

1.0 INTRODUCTION

Titanium reinforcing bars for concrete rehabilitation have been proposed and demonstrated in laboratory tests and in a single field application [Higgins et al. 2015 and 2017; Adkins and George 2017]. The primary advantage of titanium is its resistance to corrosion. It is felt that titanium reinforcing bars may have a market in concrete and masonry repair applications [Adkins and George 2017, Osofero et al. 2014], particularly in unique environments and in connection with historic structures since titanium is generally inert in most environments and is noncorroding. The investigation of titanium reinforcing bars for reinforced concrete and for near-surface mounted (NSM) repair of concrete and masonry structures involves several unique issues and provides an opportunity for further research into aspects of reinforced concrete design that remain contentious.

1.1 DESIGN WITH TITANIUM REINFORCING BARS

Reinforced concrete design criteria are based on either strength or serviceability limit states. With the introduction of different materials, consideration must be made as to how these materials impact extant design standards, or whether existing standards may be adopted for new materials at all. It has been shown that while the use of higher strength materials is not

prohibited, their use greatly impacts the performance and therefore the serviceability of a structure [e.g., Shahrooz et al. 2011]. Existing codes and standards must be re-evaluated to not only permit these newer and higher strength materials but must be adapted in order to embrace their performance characteristics.

The stress-strain and other fundamental material behaviors of titanium are similar in form to those of steel. Like steel, titanium exhibits an elastic behavior to a proportional limit, a definable yield value followed by some degree of strain hardening and exhibits a great deal of ductility. Ti6Al-4V (grade 5 titanium) exhibits yield strength approximately twice that of ASTM A615 reinforcing steel and an extensional modulus about 55% of steel. Thus, the yield strain of Ti6Al-4V is on the order of 0.008, approximately four times greater than A615 steel. The essentially elastic-plastic stress-strain behavior of titanium is both an advantage and a disadvantage when considering titanium as an alternative to steel reinforcement. It is an advantage in the sense that engineers are comfortable with the behavior profile of the material. The softer response, however, affects the assumed reinforced concrete behavior and can be a significant disadvantage when considering serviceability criteria. The behavior of reinforcing steel, particularly under service loads, is a function of axial (tensile) stiffness, EA ; thus, to directly replace steel with titanium, twice as much titanium as steel is required. Typically, this will not be practical. The alternative design paradigm used for glass fibre-reinforced polymer (GFRP) reinforcing bars [ACI 440.1R-15] – whose behavior is elastic to failure and whose modulus ranges from 20% to 50% that of steel – may be appropriate for titanium-reinforced concrete or for using titanium as a retrofitting reinforcement.

1.2 ORGANIZATION OF THESIS

The application of titanium reinforcing bars for concrete raises several questions, primarily as to how titanium bars will perform in an environment such as that present in new or existing reinforced concrete structures. The presence of chlorides from salt water and deicing agents provides the ideal electrolytic environment to promote galvanic corrosion between titanium and existing steel reinforcing bars. A galvanic cell, if present, will accelerate corrosion of the steel as has been observed in marine applications [Bomberger et al. 1954]. Therefore, a corrosion study, presented in Chapter 2, investigating the potential for galvanic corrosion was the first conducted. Galvanic corrosion is a “show stopper”. If reinforcing steel, in the presence of titanium exhibits galvanic corrosion (i.e., the presence of titanium drives corrosion of the steel), there is little likelihood that titanium will prove a practical reinforcing or repair material. This study also included stainless steel and carbon fiber reinforced polymer (CFRP) reinforcing bars in order to place the performance of titanium in context with other accepted reinforcing bar materials (glass fiber reinforced polymer (GFRP) is not included in the galvanic study since glass is an insulator). Results indicated no impediment to the use of titanium reinforcing bars with respect to galvanic corrosion potential.

The reported research program continued with extensive material and geometric characterization of titanium reinforcing bars provided by a local manufacturer, presented in Chapter 3. The bars reported in Chapter 3 are used in the subsequent experimental program described in Chapters 4 and 5 and serve as the basis for prototype designs presented in Chapter 6. Deformation geometry was extensively investigated. Pilot investigations of the fatigue behavior and the bendability of titanium reinforcing bars is also presented in Chapter 3.

The smooth titanium staples demonstrated by Higgins et al. [2015 and 2017] suffer from a few potential drawbacks: a) the smooth bars have little bond and therefore provide limited crack control over their length likely rendering long staple applications inefficient; and b) titanium must be bent at temperatures on the order of 500oC meaning the staples, must be prefabricated. Deformed titanium bars potentially overcome both concerns: a) deformations provide uniform bond over the length of the bar which b) can also be used to provide standard development length anchorage of straight bars. Nonetheless, in comparison to steel-reinforcement, the lower modulus of titanium will affect bond performance and serviceability considerations including crack spacing, crack width and deflection of members. The higher strength of titanium will require greater development lengths to achieve the yield stress. The experimental program, reported in Chapter 4, therefore assessed the bond characterization and apparent development length of titanium reinforcing bars in order to establish bases for design and detailing with titanium bars.

Chapter 5 reports a pilot study of titanium NSM repair of highway bridge slabs. This study addresses design of the titanium NSM reinforcement based both on equivalent strength and stiffness of the steel reinforcing bars ‘replaced’ by the NSM reinforcement. The study also compares straight bars and titanium staples.

Chapter 6 presents a series of benchmark designs – founded in both steel – and GFRP-reinforced concrete design paradigms conducted to establish the design space for titanium reinforcing bars. Economic considerations are also discussed based on these designs but are not a primary focus of this work.

1.3 DISCLAIMER

This document presents engineering design examples; use of the results and/or reliance on the material presented is the sole responsibility of the reader. The contents of this document are not intended to be a standard of any kind and are not intended for use as a reference in specifications, contracts, regulations, statutes, or any other legal document. The opinions and interpretations expressed are those of the author and other duly referenced sources. The designs presented have not been implemented nor have they been sealed by a professional engineer.

2.0 GALVANIC CORROSION IN REINFORCED CONCRETE

Galvanic corrosion is a primary cause of corrosion affecting steel-reinforced concrete. Galvanic corrosion in steel-reinforced concrete is more likely to play an important role in the corrosion of large areal structures such as bridge decks and arises from differences in aeration (oxygen), alkalinity (carbonation) or salt (chloride) concentration; all resulting in uneven passivation of the reinforcement [Gulikers and Schlangen 1996]. In particular, patching operations have been found to drive galvanic corrosion cells since the patch and the substrate concrete represent different environments (in particular, the substrate may contain chlorides accumulated over years, while the patch is chloride-free) [Gulikers and Van Mier 1992]. The extensive use of de-icing salts is believed to result in the disproportionate instance of damage to bridge structures attributed to galvanic corrosion in North America [Song and Shayan 1998]. Nonetheless, there are relatively few systematic studies of galvanic corrosion cells in steel-reinforced concrete.

The extensive issues with corrosion have led some to use stainless steel reinforcing bars in susceptible structures. Due to the cost of stainless steel, it is often only used for top-slab reinforcing while conventional ‘black’ steel is used elsewhere. Installation of reinforcement often requires field bending. The cold work performed in the field to bend a stainless-steel bar will introduce high residual stresses at the bend. These regions with different local stress or high-energy regions behave like anodes to the lower-stressed, or cathodic areas (Figure 2.1a). This is due to the formation of carbides at the grain boundaries which remove chromium from the

austenite adjacent to the grain boundaries. This action results in a lower energy state adjacent to the grain boundaries making them cathodic (Figure 2.1b). This difference in localized metal composition produces stress cells that will produce stress corrosion by galvanic corrosion [Askeland and Wright 2015]. Thus, even the use of supposedly inert stainless-steel bars can, in some cases, result in corrosion damage to a structure.

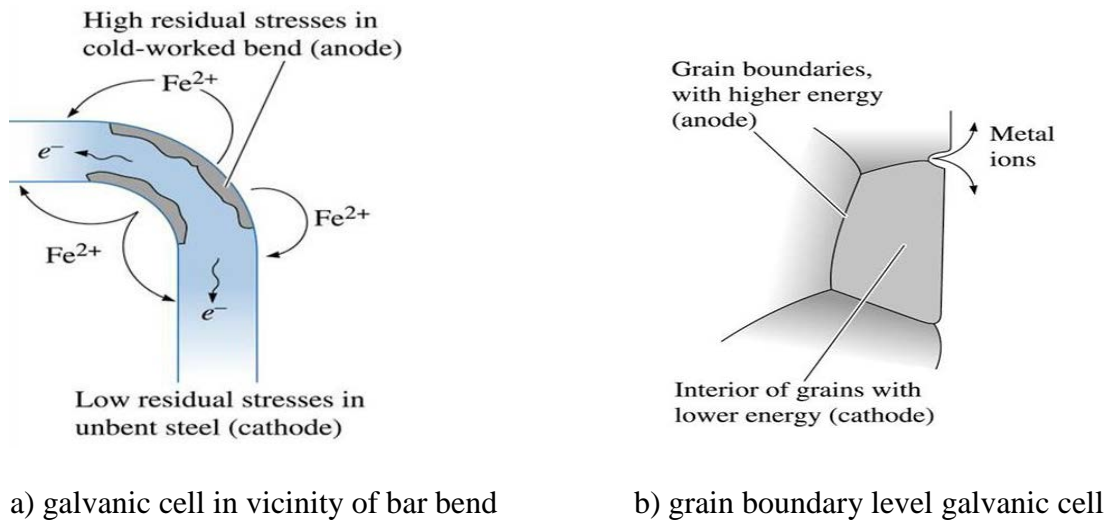


Figure 2.1 Examples of stress cells [Askeland and Wright 2015].

This use of dissimilar materials raises the potential for galvanic corrosion to accelerate the corrosion of the black steel in the reinforced concrete system. A number of studies have investigated this effect. Provided both the black and stainless steels remain passive, the use of stainless steel has not been found to increase the risk of corrosion of the black steel [Pérez-Quiroz et al. 2008; Bertolini and Pedferri 2002; Knudsen and Skovsgaard 2001; Klinghoffer et al. 2000; Cochrane 1999]. Hope [2001] concluded that although corrosion of black steel would occur in a galvanically-coupled system when the concrete is contaminated with chlorides or carbonated, the rate of corrosion would not be appreciably different than if black steel alone were

present. Indeed, Qu et al. [2003] and Broendby [1999] concluded that coupling black steel and stainless-steel results in lower corrosion rates than coupling black steel in a chloride-laden environment. Webster [1997] and Seibert [1998], on the other hand, indicate that galvanic corrosion will take place when stainless and black steel are electrically coupled and recommend that these materials be electrically isolated from one another. Stainless steel reinforcing bars are accepted as an alternative reinforcement in highly corrosive environments and by most bridge owners in North America.

Similar questions of the potential for galvanic corrosion are raised when using carbon fiber reinforced polymer (CFRP) composite materials in repair of steel-reinforced concrete. ACI 440.2R-17 states: "...CFRP is conductive. To avoid potential galvanic corrosion of steel elements, carbon-based FRP materials should not come in direct contact with steel." PCA [1970] recommends that nonferrous metals (copper, zinc, aluminum and lead) in contact with concrete should be electrically isolated from the reinforcing steel. In the presence of chlorides, galvanic corrosion is also likely for nickel and cadmium coated steel reinforcement [PCA 1970]. In a well-established commercial application, galvanic coupling is used to protect reinforcing steel from corrosion through the use of sacrificial zinc anodes in a process known as 'cathodic protection' (e.g., vector-corrosion.com).

2.1 GALVANIC CORROSION OF STEEL COUPLED WITH TITANIUM

Most data on galvanic corrosion with titanium relates to the materials in a marine environment. A low-velocity, poorly aerated sea-water environment is not dissimilar to the environment in chloride-laden concrete. Coastal steel-reinforced concrete structures, in addition to those subject to de-icing salts, exhibit significant amounts of galvanic corrosion.

In most environments, titanium will be the cathodic member of a galvanic couple. In terms of voltage potential in moving seawater versus a saturated calomel reference electrode [Laque 1975], titanium has a potential of 0V; mild steel has a potential of -0.65V, making steel the active anode in a titanium-steel cell. By comparison, stainless steel has a potential near -0.5V when active. Figure 2.2 shows an example of corrosion potentials of various materials in flowing sea water. When electrically coupled, the more noble metals on the left side of the figure will be cathodic whereas those on the right, which are less noble, will be anodic and therefore the corroding element in the galvanic cell.

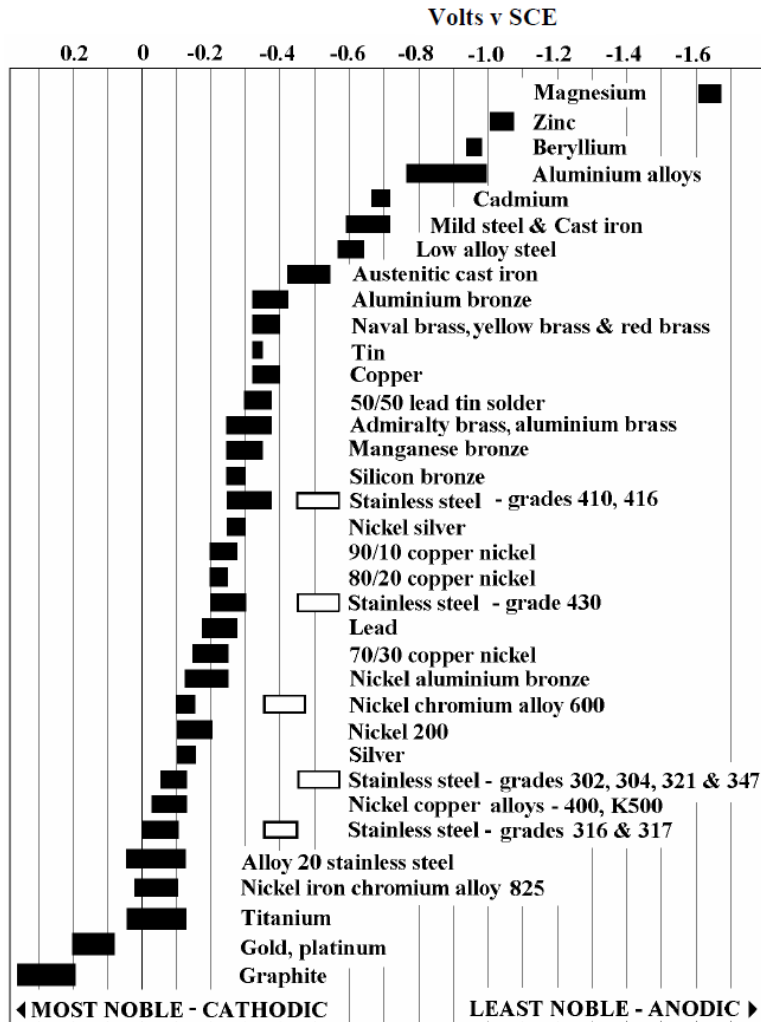


Figure 2.2 Corrosion potentials in flowing sea water [Atlas Steels 2010]

In a marine environment, titanium has been shown to have an accelerating effect on the corrosion rate of mild steel when galvanically connected (Table 2.1). If the surface area of titanium is small in relation to the area of steel, the accelerating effect is negligible. However, if the area of the titanium greatly exceeds the area of steel severe corrosion may result [Cotton and Downing 1957; Bomberger et al. 1954].

Table 2.1 Behavior of Steel-Titanium galvanic couples in marine environments.

	Cotton and Downing [1957]		Bomberger et al. [1954]	
Areal ratio: Steel:Ti (anode:cathode)	10:1	1:10	7:1	1:7
test condition	immersed in aerated sea water for 2500 hours		half tide (wet-dry) 193 days	
uncoupled corrosion rate, mpy	4.2	5.1	6.10	
coupled corrosion rate, mpy	6.0	28.5	12.32	17.24
increase due to coupling	1.42	5.59	2.02	2.83
test condition	3% salt mist for 5000 hours		half tide (wet-dry) 369 days	
uncoupled corrosion rate, mpy	30.5	14.7	8.60	
coupled corrosion rate, mpy	-	19.4	12.20	12.90
increase due to coupling	-	1.32	1.42	1.50
test condition			shore rack 360 days	
uncoupled corrosion rate, mpy			6.13	
coupled corrosion rate, mpy			9.82	-
increase due to coupling			1.60	

mpy = mils per year = 0.001 in./year)

2.1.1 Objective of Study

The objective of the reported study is to assess the effects of coupling titanium and black steel in typical concrete. The titanium is 1) embedded in the concrete; 2) ‘potted’ in an epoxy resin prior to embedment in concrete; and 3) ‘potted’ in a cementitious repair mortar prior to embedment in concrete. The potted specimens are intended to better replicate conditions in a real repair scenario in which the titanium will be used as NSM reinforcement. In order to place the use of titanium in context, duplicate specimens having stainless steel and CFRP reinforcing bars are also tested.

2.2 GALVANIC CORROSION TEST PROGRAM

2.2.1 Test Specimens

Sixty-two (62) 152 x 152 x 152 mm (6 x 6 x 6 in.) concrete prisms were formed as summarized in Table 2.2. Each prism has a single #4 (12.7 mm (0.5 in.) diameter) ASTM A615 Grade 60 black steel bar embedded a distance d from the concrete surface to which the NSM ‘repair’ is made (see Table 2.2). A 12.7 mm (0.5 in.) diameter titanium (Ti), CFRP or 2205 stainless steel (SS) NSM bar is embedded along one side of the concrete prism into NSM ‘slots’ having dimensions recommended by ACI 440.2R-17 for NSM CFRP (Figure 2.3). The NSM bars were ‘potted’ in advance (rather than having to cut and install all NSM bars following concrete placement).

Additional specimens having titanium NSM strips (Tis) of the same area (129 mm² (0.2 in²)) were also tested since such strips reduce installation cost in NSM applications. In the strip applications, the width of the slot was only $2.5a_b$, rather than the $3a_b$ shown in Figure 2.1. All bar specimens are shown, prior to placement in concrete, in Figure 2.4a. Specimens following placement of concrete are shown in Figure 2.4b.

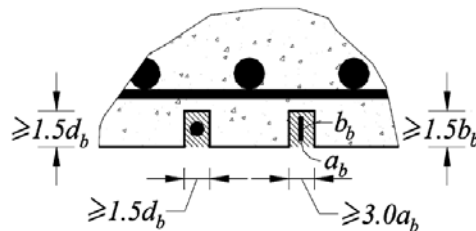


Figure 2.3 Minimum dimensions of NSM ‘slots’ [ACI 440.2R-17 Fig. 14.3]



a) plain and ‘potted’ NSM bars prior to being placed in concrete

left to right:

- ASTM A615 “black steel”
- Ti bar
- Ti bar embedded in epoxy
- Ti bar embedded in cementitious grout
- CFRP bar
- CFRP bar embedded in epoxy
- CFRP bar embedded in cementitious grout
- SS bar
- SS bar embedded in epoxy
- SS bar embedded in cementitious grout
- Ti strip
- Ti strip embedded in epoxy
- Ti strip embedded in cementitious grout

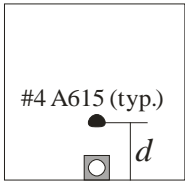
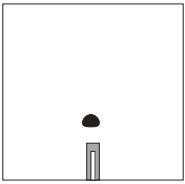
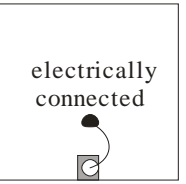
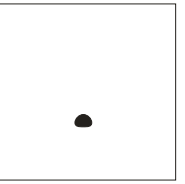
b) 152 mm cube specimens ($d = 102$ mm shown). Embedded NSM bars are at top of each specimen.

Figure 2.4 Specimens prior to conditioning.

Control specimens having the NSM and black steel bars electrically coupled (Figure 2.5c) and specimens having no NSM bar were also prepared. The detailed test matrix is provided in Table 2.2. Two replicates of each specimen were made. Specimen identification is as follows:

M-N-d-s-E				
M = Material	N = NSM embedment	d	s = replicate specimen	E = electrically connected?
Ti = Ti bar Tis = Ti strip C = CFRP SS = stainless steel	C = concrete G = grout E = epoxy	2 = 51 mm (2.0 in.) 4 = 102 mm (4.0 in.)	a b	E = yes blank = no

Table 2.2 Test matrix

152 x 152 x 152 mm (6 x 6 x 6 in.) concrete prisms having single #4 A615 embedded bar				
NSM Material	Ti, CFRP and SS	TiS	Ti, CFRP, SS and TiS	none
NSM dimension	12.7 mm dia. (0.5 in.)	25.4 x 5.1 mm (1 x 0.2 in.)	12.7 mm dia. and 25.4 x 5.1 mm	
area of NSM	129 mm ² (0.2 in ²)	129 mm ² (0.2 in ²)	129 mm ² (0.2 in ²)	-
surface area of NSM	39.9 mm ² /mm (1.57 in ² /in)	61 mm ² /mm (2.4 in ² /in)	39.9 mm ² /mm and 61 mm ² /mm	
surface area ratio NSM:A615	1.0	≈1.5	1.0 and ≈1.5	-
<i>d</i>	51 and 102 mm (2.0 and 4.0 in.)	51 and 102 mm (2.0 and 4.0 in.)	electrically connected	-
NSM1: epoxy bonding agent	SIKADUR 30	SIKADUR 30	-	-
slot dimension	19 x 19 mm (0.75 x 0.75 in.)	38 x 12.7 mm (1.5 x 0.5 in.)	-	-
NSM2: cementitious bonding agent	SIKAGROUT 212	SIKAGROUT 212	-	-
slot dimension	19 x 19 mm (0.75 x 0.75 in.)	38 x 12.7 mm (1.5 x 0.5 in.)	-	-
NSM3: embedded in concrete	concrete	concrete	concrete	-
specimens	36 specimens	12 specimens	8 specimens	6 specimens

2.2.2 Materials

Concrete – Sakrete 5000 premixed concrete was used. This mix reports a cement (Type I/II) content of 10-30%. For the purposes of calculation, 20% cement content was assumed. 4.55 L (10 lb.) water was mixed per 80 lb. (36.4 kg) bag of concrete resulting in a presumed water/cement (*w/c*) ratio of 0.63.

To replicate a chloride-laden concrete which may be typical of an older bridge or parking structure or a structure located in a sea water environment, 252 g of laboratory grade (95% w/w) Calcium Chloride Dihydrate (Fisher Scientific S25221A) was dissolved (prior to concrete mixing) into the mix water per bag of concrete. This is equivalent to 4.3% CaCl_2 by weight of cement based on industry-standard CaCl_2 flake (77%) equivalence and on 20% cement content per bag.

Specimens were cured in a standard laboratory environment for more than 28 days prior to beginning conditioning. At 28 days, standard compression [ASTM C39-16] tests were performed in order to quantify the concrete used. The compressive strength, f'_c , was found to be 29.5 MPa (4280 psi) (COV = 0.10) and the modulus, $E_c = 22.2$ GPa (3220 ksi) (COV = 0.04).

Black Steel – ASTM A615 Grade 60 #4 bars, having a nominal diameter of 12.7 mm (0.5 in.) and area of 129 mm² (0.2 in²), were used. The yield strength, f_y , was experimentally determined to be 476 MPa (69 ksi).

Titanium bars – smooth 6Al-4V titanium bars having a diameter of 12.7 mm (0.5 in.) were provided by Perryman Company. The yield strength was experimentally determined to be 1019 MPa (148 ksi).

Titanium strips – 25.4 x 6.4 mm 6Al-4V titanium strips were provided by the manufacturer. In order to have the same cross-sectional area as the bars, these were machined to a width of 5.1 mm for use in this study. The yield strength was experimentally determined to be 931 MPa (135 ksi).

CFRP – ‘Aslan 200’ sand-coated CFRP reinforcing bars having a nominal diameter of 12.7 mm (0.5 in.) were provided by Hughes Bothers (Seward NE). These bars have a guaranteed tensile strength of 2070 MPa (300 ksi) and tensile modulus of 124 GPa (18,000 ksi).

Stainless Steel – Grade 2205 Duplex #4 bars were provided by Salit Specialty Rebar (Niagara Falls NY). The yield strength was experimentally determined to be 579 MPa (84 ksi).

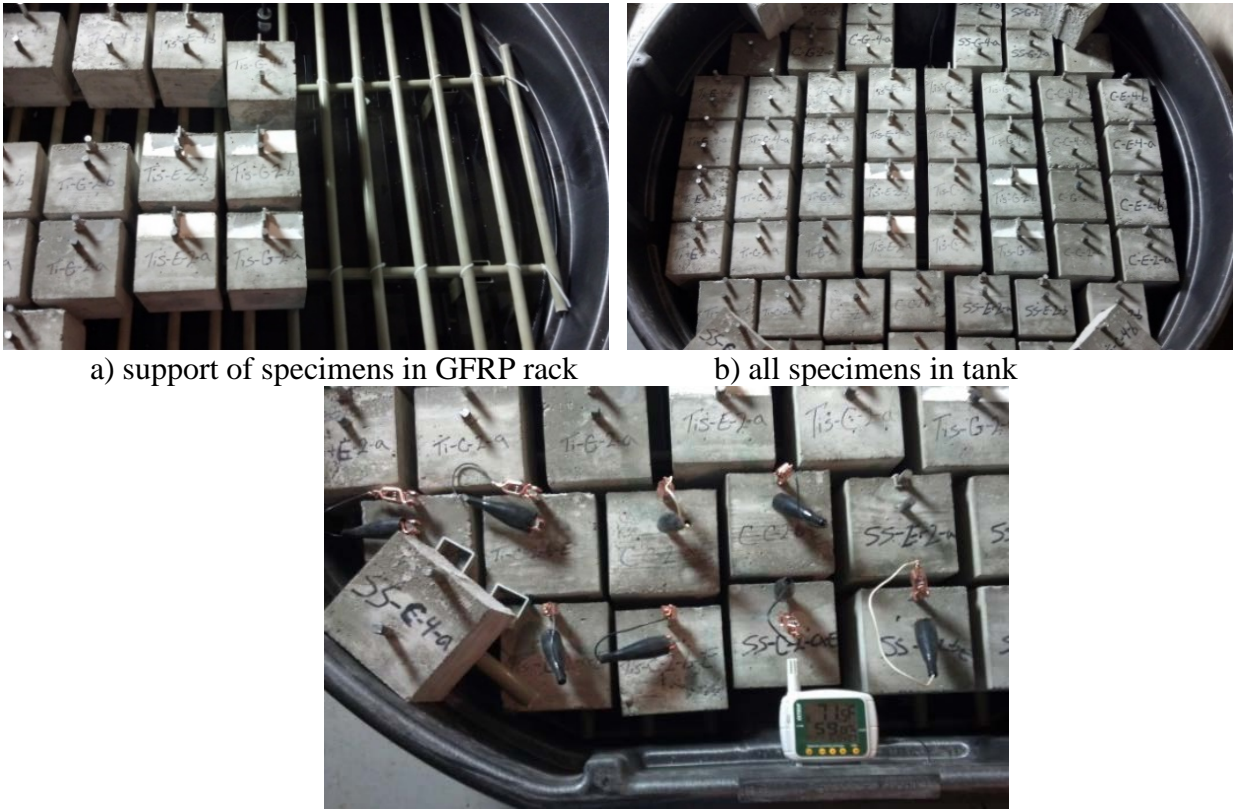
NSM Epoxy –SIKADUR30 was used. This is a commercially available two-part structural adhesive, based on a combination of epoxy resins and proprietary filler. The adhesive is commonly used to bond structural reinforcement in NSM applications.

NSM cementitious grout – SikaGrout 212 was used. This is a commercially available one part flowable shrinkage compensating cementitious grout. The grout is commonly used in concrete repair applications and to bond steel reinforcement anchors.

2.2.3 Conditioning Protocol

Following 35-days laboratory cure, specimens were placed in a covered water-filled plastic tank (Figure 2.5). The specimens were supported on a non-corrosive, non-conductive GFRP rack above the water level (Figure 2.5a). A thermostat-controlled tank heater was used to raise the water temperature and therefore the temperature/humidity in the covered tank. The tank heater turned on at 27°C (80°F) and shut off at 49°C (120°F) water temperature resulting in variation of conditioning environment temperature and RH as indicated in Figures 2.6 and 2.7. When heated and covered, air temperature surrounding the specimens varied between 29 and 35°C (85 and 95°F) and relative humidity (RH) was typically logging 99.9%. When unheated and not covered, the specimens were in an air-conditioned ambient laboratory environment in which temperature remained approximately 21±2°C (70 ±4°F) and RH varied as low as 25%. The environment was typically cycled on a 1-2-1-3-day cycle as shown in Table 2.3. Conditioning began April 7, 2015

and lasted 746 days (April 26, 2017). The temperature and humidity in the tank was monitored on an hourly basis using an Extech 42280 temperature/RH logger (seen in Figure 2.5c). A typically weekly log is shown in Figure 2.6. The complete log, showing 7 April 2015 through 4 March 2017 (697 days) is shown in Figure 2.7. The data logger failed to capture the final 49 days of conditioning.



a) support of specimens in GFRP rack b) all specimens in tank
c) electrically coupled specimens and T/RH sensor

Figure 2.5 Specimens in conditioning tank (photo taken before conditioning begun).

Table 2.3 Typical weekly conditioning schedule

Monday	Tuesday	Wednesday	Thursday	Friday	Saturday	Sunday
dry	wet	wet	dry	wet	wet	wet
tank uncovered, no heat, specimens permitted to dry	tank covered, heater engaged	tank covered, heater engaged	tank uncovered, no heat, specimens permitted to dry	tank covered, heater engaged	tank covered, heater engaged	tank covered, heater engaged

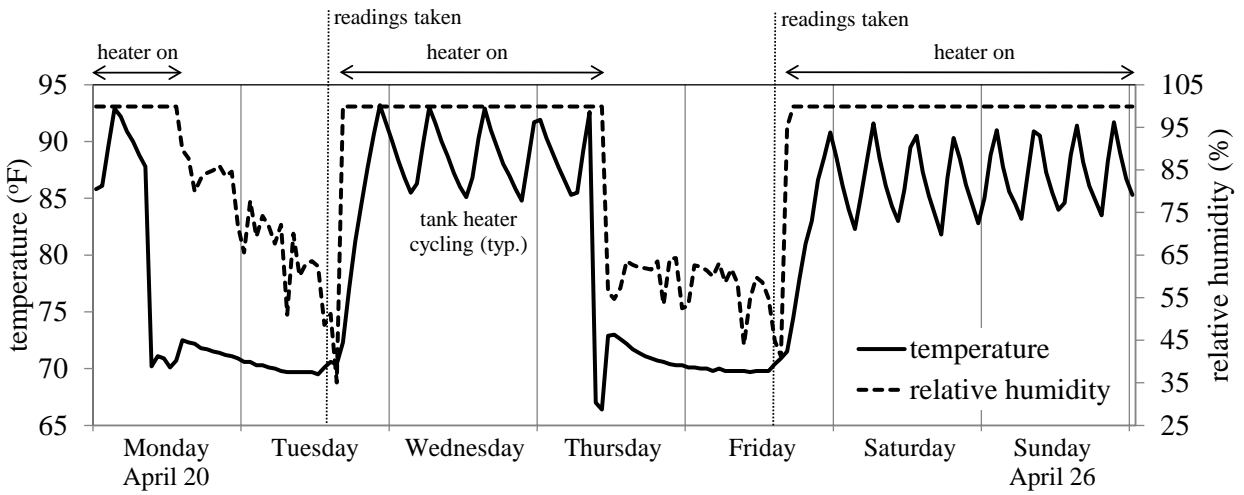


Figure 2.6 Typical weekly temperature/RH log

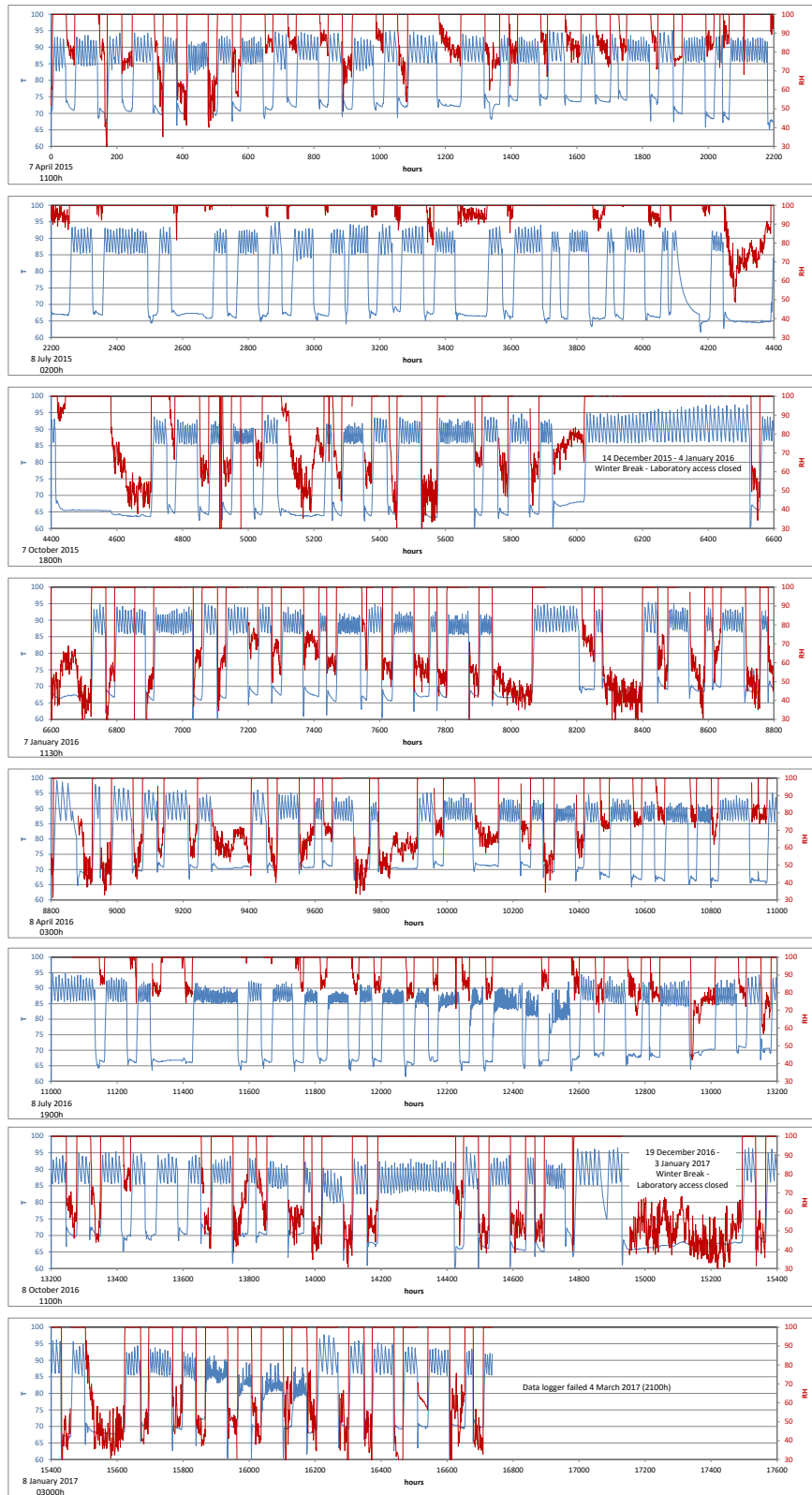


Figure 2.7 Temperature/RH log

2.2.4 Specimen Monitoring

Two series of tests were conducted on a regular basis. Tests were conducted on a twice-weekly basis early in the conditioning protocol and on a bi-weekly basis later. All tests were conducted following a period of 24h drying (i.e., typically Tuesday or Friday mornings prior to the tank being recovered and the heater reengaged as indicated in Table 2.3). Exact time increments are reported in the data summary tables provided as digital Appendices to this thesis.

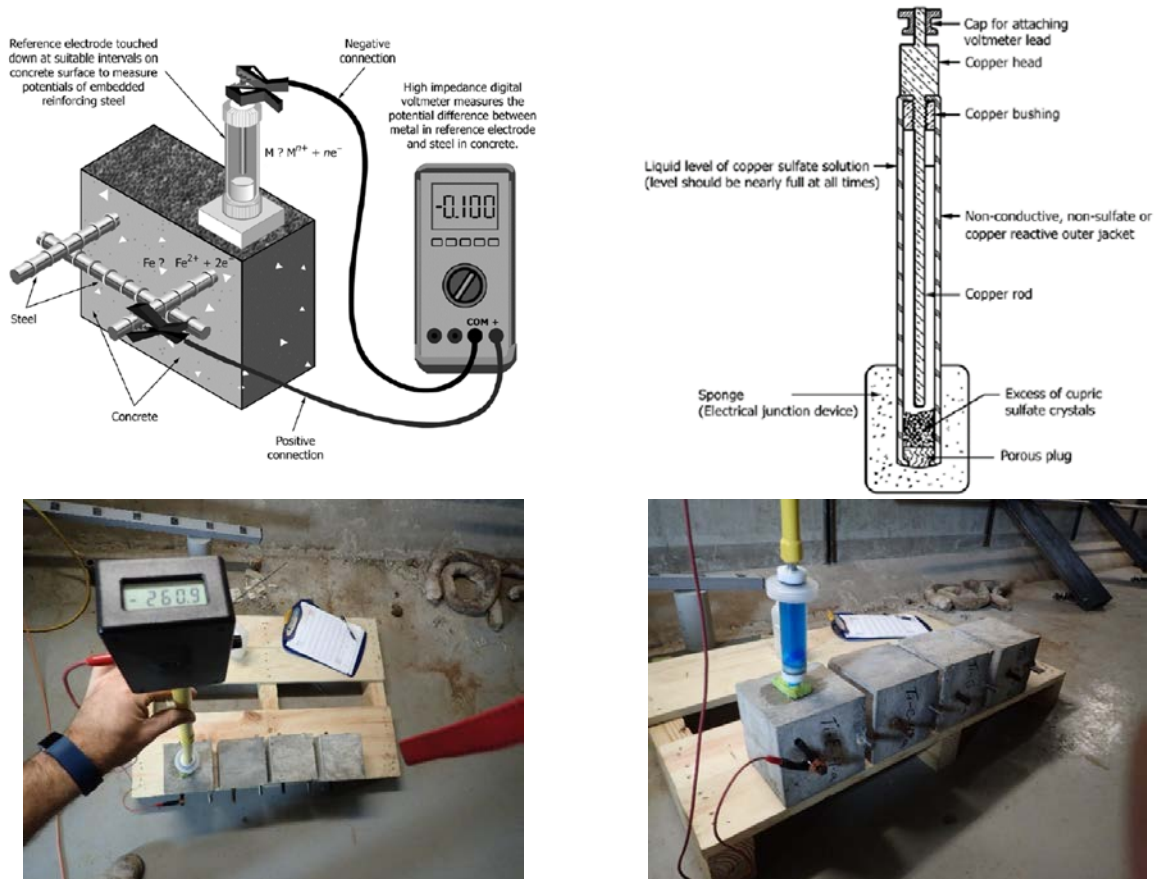
2.2.4.1 Half-cell potential (based on ASTM C876 10.3)

This test was conducted using a James Instruments Cor-Map System (Copper/Copper Sulphate half-cell potential system). The test provides a sense of the presence and magnitude of corrosion.

Corrosion is an electrochemical process which occurs in concrete when oxygen and moisture are present. The actual corrosion is an exchange of energy within different sections of the uncoated reinforcing steel. The relative energy levels can be determined in relation to a reference electrode having a stable electrochemical potential. The reference cell used was copper in a copper sulphate solution (Cu-CuSO₄).

By connecting a high impedance voltmeter between the reinforcing steel (the A615 bar in all cases) and a reference electrode (Copper/Copper Sulphate Electrode, CSE) placed on the concrete surface (Figure 2.8), a measurement can be made of the half-cell potential at the location of the reference cell. This is a measurement is correlated to the probability of corrosion activity in the steel in the vicinity of the reference cell. ASTM C876 provides the following *guidance* in interpreting results of this test.

- 1) For readings that are more negative than -350mV there is a 90% chance of active steel corrosion.
- 2) For readings between -200 and -350mV the results are inconclusive; some report that this corresponds to a 50% chance of active steel corrosion.
- 3) For readings that are more positive than -200mV there is only 5% chance of active steel corrosion.
- 4) Readings that have relatively high negative values with little variance in time may indicate that corrosion is possible, but that oxygen availability is very limited impeding the corrosion process.



a) Basic configuration of the electrical circuit [ASTM C876] b) Sectional view of a Copper-Copper Sulfate reference electrode [ASTM C876]

Figure 2.8 Half-cell potential equipment and testing

2.2.4.2 Macrocouple Current (based on ASTM G102-89)

Direct measurement of current between the embedded A615 steel bar and NSM bar was made using a Keithley 485 Autoranging Picoammeter. In this test, the current (in μA) measured between the embedded A615 steel bar and the NSM bar, I_{cor} , is an indirect measure of the rate of corrosion present (Equation 2.1). Values of I_{cor} , may be directly compared to assess relative rates of corrosion (see Eqs. 2.4 and 2.5). Faraday's law may be used to calculate the theoretical corrosion penetration rate (CR) or mass loss rate (MR) as follows [ASTM G102-89].

The corrosion current density (in $\mu\text{A}/\text{cm}^2$) for the embedded A615 steel bar (anode) is:

$$i_{cor} = I_{cor}/A \quad (2.1)$$

in which A = exposed anode surface area; for a #4 bar embedded in 152 mm of concrete,

$$A \approx \pi (12.7)(152) = 60.6 \text{ cm}^2.$$

The corrosion rate (in mm/yr) for carbon steel is given as:

$$CR = K_1 i_{cor}(EW)/\rho \quad (2.2)$$

in which: $K_1 = 3.27 \times 10^{-3} \text{ mm g}/\mu\text{A cm yr}$ (ASTM G102)

$$EW = 27.92 \text{ for carbon steel (ASTM G102, Table 1)}$$

$$\rho = 7.86 \text{ g}/\text{cm}^3 \text{ (ASTM G102, Table X1.1)}$$

The mass loss rate (in $\text{mg}/\text{dm}^2\text{d}$) for carbon steel is given as:

$$MR = K_2 i_{cor}(EW) \quad (2.3)$$

in which: $K_2 = 8.954 \times 10^{-2} \text{ mg cm}^2/\mu\text{A dm}^2 \text{ d}$ (ASTM G102)

$$\text{Thus: } CR = 1.91 \times 10^{-4} I_{cor} \text{ mm/yr} \quad (2.4)$$

$$MR = 2.50 I_{cor} \text{ mg}/\text{dm}^2\text{d} \quad (2.5)$$

2.2.4.3 Measurement of Reinforcing Bar Mass Loss

Following the conditioning period, all steel bars were recovered and mass loss due to corrosion determined. The following procedure was carried out to determine an average mass loss. All bars were sand-blasted (garnet abrasive with a Moh's hardness of 7.5) to remove adhering concrete and corrosion product. The bars were cut to their 152 mm (6 in.) embedment length and weighed. The masses were compared to uncorroded control specimens cut from the same reinforcing bar. The average mass of an uncorroded bar was 0.89 g/mm length

Where corrosion pits or highly localized corrosion was identified, the specimens were cut to isolate these regions and the masses of these smaller samples compared to that of the uncorroded control specimens. As the length of sample decreases, the mass loss calculation is increasingly a better estimation of cross section loss which is critical to bar performance.

2.3 GALVANIC CORROSION TEST RESULTS

2.3.1 Prior to Conditioning

Initial 'zero' readings were made 7 April 2015 prior to any conditioning cycles. As expected, the half-cell potential data indicated the *potential* for steel corrosion in the 'salted' concrete specimens. The average reading for all specimens was -400 mV (COV = 0.13) with maximum and minimum recorded values of -269 and -517 mV, respectively. There was no statistically significant variation based on material (Ti, Tis, CFRP or SS) or NSM embedment material

(concrete, epoxy or grout); nor should there expected to be at the beginning of the conditioning period.

Macrocouple current data in the previously unconditioned specimens is summarized in Figure 2.9. In the previously unconditioned and non-corroding specimens, the current varied seven orders of magnitude – from essentially zero (70 pA) to 41.7 μ A. Even the largest values do not indicate a significant level of active corrosion (Eqs. 2.4 and 2.5). The macrocouple data does indicate that the epoxy NSM material is an effective electrical insulator; the macrocouple current in specimens with epoxy NSM embedment did not exceed 0.1 μ A, representing a statistically significant variation from concrete ($p = 0.01$) or grout ($p = 0.03$) embedment. A less significant variation ($p = 0.07$) was observed between concrete and grout embedment although this is skewed by consistently high results for the stainless steel embedded in grout (see Figure 2.9). Curiously, despite their epoxy content, the CFRP bars did not appear to be electrically insulated and exhibited macrocouple currents similar to the other materials when embedded in the same NSM material.

It can be seen in Figure 2.9 that the Ti strip material exhibited uniformly greater macrocouple current than the Ti bars. This may partially result from the 53% greater surface area of the strips compared to the bars (Table 2.2) resulting a greater areal ratio as discussed in relation to Table 2.1.

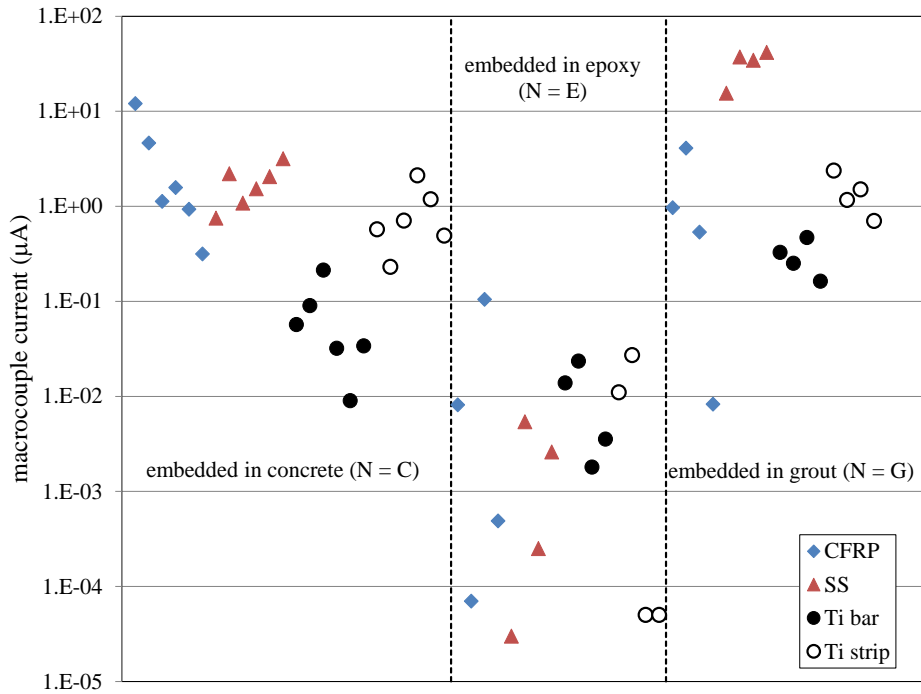


Figure 2.9 Grouping of specimens by macrocouple current prior to start of conditioning

2.3.2 During Conditioning

2.3.2.1 Half Cell measurements

Having established the high probability for active corrosion to develop, half-cell measurements are less useful in the time domain for small specimens. Significantly, the cyclic wetting and drying washes/leaches the surface chlorides out of the relatively small specimens resulting in the potential approaching a steady state [Poursaee 2011]. The average measured half-cell potential remained below -248 mV over the two-year conditioning program as seen in Figure 2.10.

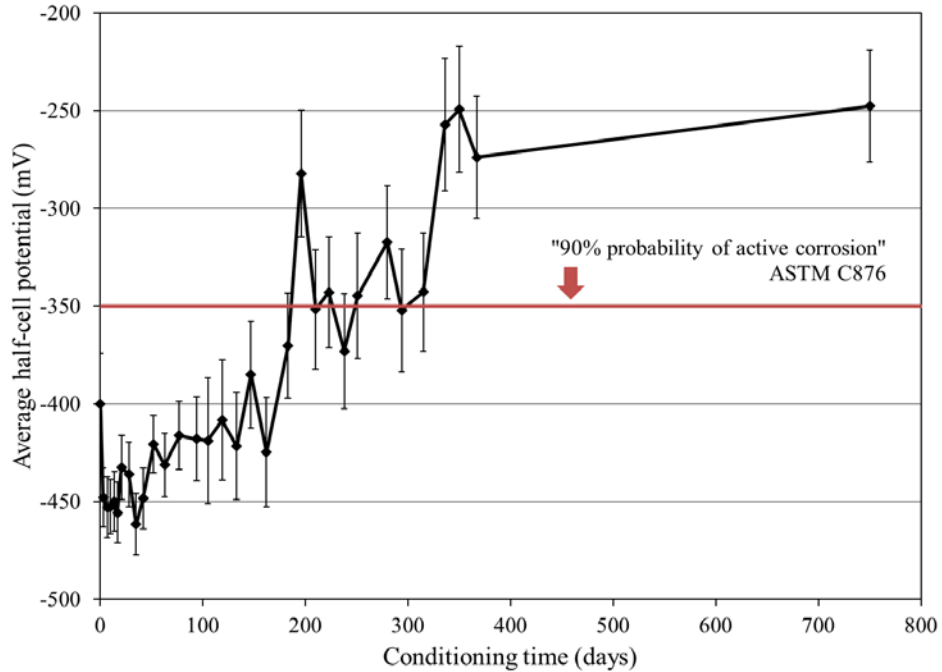


Figure 2.10 Half-cell potential history showing average and one standard deviation

Figure 2.10 shows the average half-cell potential values throughout the conditioning period for all specimens. It is clear that all specimens show a potential more negative than -350 mV for at least the first 175 days which corresponds to a greater than 90% probability of active corrosion according to ASTM C876. This correlates well with the high chloride contamination that was introduced during mixing of the concrete. The fluctuations thereafter and a decrease in potential (i.e. less negative) implies an increasingly steady state as the amount of chloride that is leached from the specimens increases with time. This can also be attributed to the fact that the readings produced by the Cor-Map system are a function of the measured polarization resistance, R_p , as seen in Equation 2.6, represents the current exchange of the oxidation-reduction reaction (redox) process ($\text{Fe}^{2+} \leftrightarrow \text{Fe}^{3+}$) in the passive layer.

$$i_{cor} = B/R_p A = I_{cor}/A \quad (2.6)$$

Where B is the Stern-Geary constant which is empirically determined and measured as 0.026 V and 0.052 V for active and passive corrosion, respectively, of carbon steel in concrete.

As the potential decreases, nearing -200 mV, where active corrosion is uncertain, the corrosion process ($\text{Fe} \leftrightarrow \text{Fe}^{2+} + 2\text{e}^-$) and the phase transformation in the oxide layer act together as shown in Equation 2.7 [Poursaei 2011].



As more Fe^{3+} accumulates in the oxide layer, the redox is extended resulting in corrosion potentials becoming more positive. The results from this experiment are largely similar to those reported by Poursaei [2011] where both chloride-free and chloride-contaminated samples were used in evaluating corrosion measurement techniques. Figure 2.11 shows the results reported by Poursaei. The patterns are similar at the beginning of both tests. As the specimens from the current study became “washed out” the concrete cubes gradually transitioned towards chloride free concrete resulting in potentials becoming more positive in a manner that closely resembles that shown in Figure 2.11.

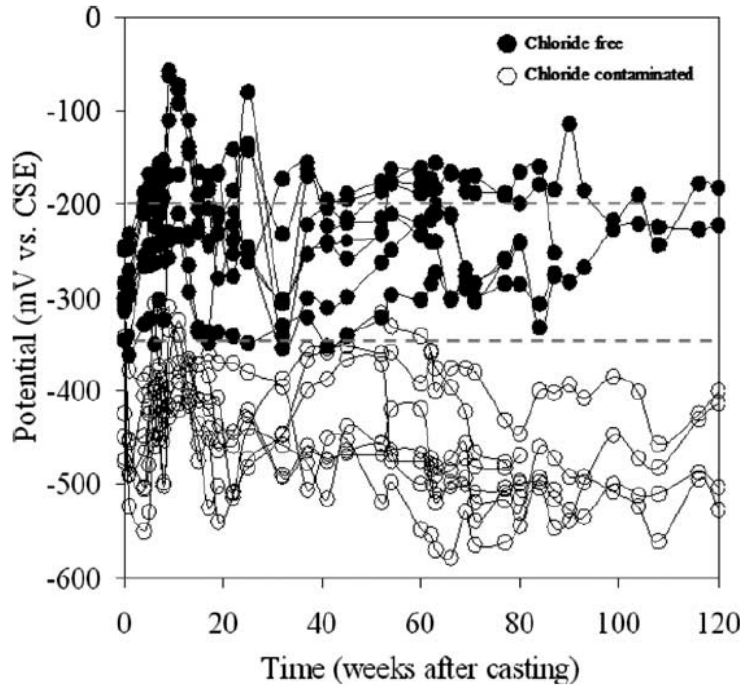


Figure 2.11 Half-cell potential values of segmented bars in concrete (Poursaei 2011)

2.3.2.2 Macrocouple measurements

The minimum 24-hour dry cycle was established to reduce moisture variability within the blocks. Macrocouple readings were taken following the dry cycle so as to reduce the influence of any remaining moisture within the blocks. Although the room used for storage was capable of remaining nearly environmentally constant, it was susceptible to season variations as seen in Figure 2.12 where the largest spikes with the greatest variability generally coincide with elevated humidity conditions with the last spike lower since most specimens were cracked at that time.

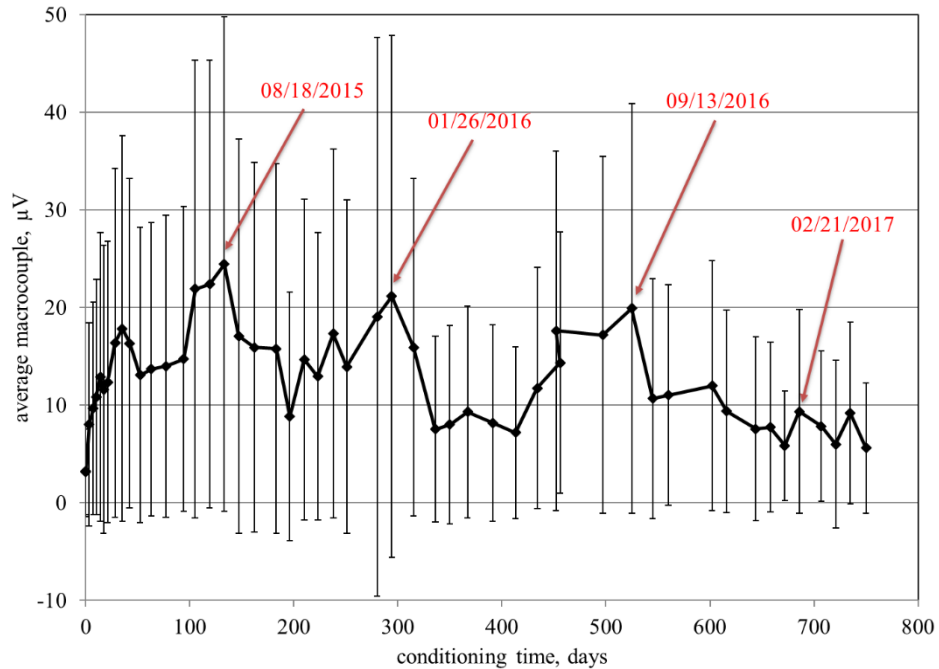


Figure 2.12 Average macrocouple history

Macrocouple current increased with time in most all specimens. This indicates that, in general, some degree of corrosion is occurring. Figure 2.13 repeats Figure 2.9 showing the macrocouple readings at the end of conditioning. Macrocouple current was similar for concrete and grout embedment and significantly lower for epoxy embedment. The epoxy initially serves as an insulator, mitigating the galvanic cell. However, the epoxy also degrades in an aggressive hygrothermal environment, becoming more permeable; this results in greater variance in the epoxy-embedded data.

A statistical analysis based the Bonferroni test (at 95% confidence interval) was carried out on the macrocouple data. Due the small sample size for each variation, only the apparent trends can be described:

- 1) Galvanic cells including stainless steel bars exhibited greater macrocouple current than the other materials. Titanium bars, strips and CFRP bars did not differ from one another.
- 2) As expected, epoxy embedment resulted in lower macrocouple current. The grout embedment resulted in higher macrocouple currents. This is believed to result because the grout used is likely to have a greater porosity than the surrounding concrete.
- 3) In the small specimens, the separation between bars (dimension d) had no significant effect on results.
- 4) An analysis dividing results into subsets of the 746-day conditioning period showed that change in macrocouple was more significant in the first six months of conditioning. This result would appear to reflect the observation of the increasing (less negative) half-cell potential described above.

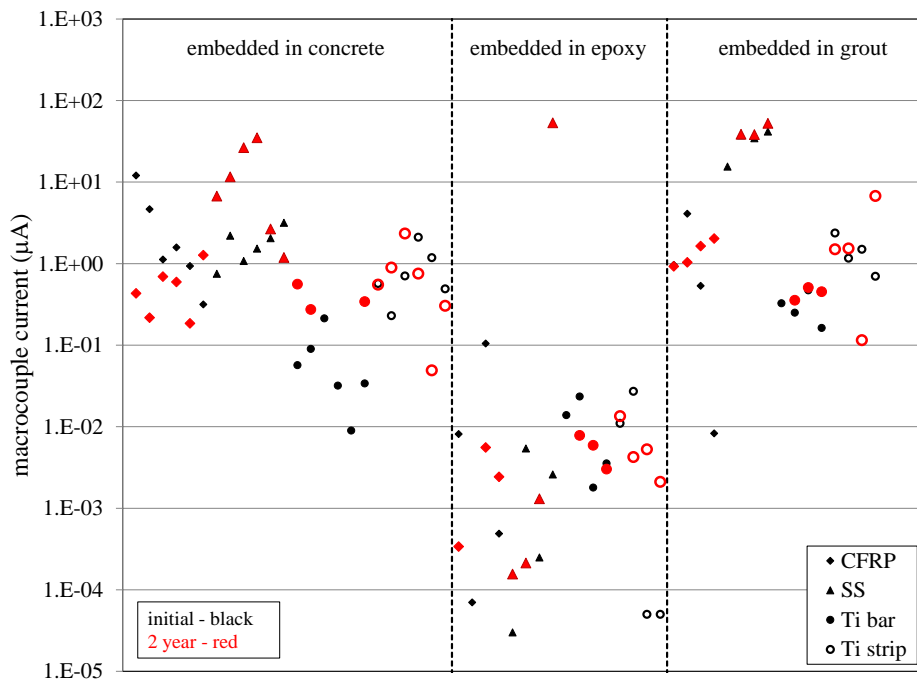


Figure 2.13 Macrocouple current following conditioning

2.3.3 Following Conditioning

Following 434 days of conditioning (June 14, 2016), small radial cracks emanating from the A615 bar were observed on some specimens. These are an indication of volumetric expansion of the bar resulting from corrosion. Three specimens were removed to determine the mass loss at the time radial cracking appeared; this was determined to range from 2% to 4.7% mass loss.

Mass loss was determined for the remainder of the specimens following 746 days of conditioning (Figure 2.14). As expected (and predicted by the half-cell potential), corrosion was observed in all specimens. Control specimens having no galvanic cell exhibited approximately 5.8% average mass loss after two years conditioning (Table 2.4). None of the galvanic cells (Fe-Ti bar, Fe-Ti Strip, Fe-SS, Fe-CFRP) exhibited statistically significant different behavior from each other or the control. 2205 duplex stainless steel exhibited statistically poorer behavior than Ti strips ($t = 0.01$) and CFRP ($t = 0.09$).

Based on visual analysis, the greatest corrosion pits for each bar were identified (Figure 2.15) and the mass loss determined for a shorter (12.6 mm) specimen determined (Table 2.4). The degree of corrosion, as measured in terms of mass loss percentage, was nearly uniform across all specimens with extreme cases where pitting was present skewing the results in some cases. Pitting in reinforcement is a localized attack and, in many cases, can be more detrimental to the service life of a reinforced concrete structure due to increased local section loss. The presence of pitting is difficult to interpret from either of the methods used in this study. The corrosion potential (E_{cor}) is related to the likelihood of the presence of active corrosion and therefore cannot be used in assessing the actual rate of corrosion. There has been some research attempting to associate values of corrosion current (I_{cor}) with active corrosion rates and

attempting to associate these values with the maximum pitting potential. Many of these studies have used the ratio of maximum pit depth to the average depth of penetration ($R = P_{avg} / P_{max}$). While the values of I_{cor} are representative of a much larger section of the overall reinforcement surface, if integrated over time may have merit in estimating the residual life of a structure taking into consideration a maximum pit depth potential. Values of R have been reported from 2 to 16 in various reports and values of 4 to 8 in chloride laden samples exposed to various accelerated testing methods [Gonzalez et al. 1995]. The values of R as seen in Table 2.4 range from 1.55 to 3.79 and are well in agreement with the previous studies.

Table 2.4 Steel bar mass loss

NSM material	average mass loss over 152 mm length					12.6 mm length	max pit
	n	average	COV	min	max	max pit mass loss	average
control	2	5.8%	-	5.3%	6.3%	16.5%	2.84
titanium bar	14	5.1%	0.46	1.9%	10.8%	18.6%	3.65
titanium strip	14	4.8%	0.27	2.5%	6.7%	16.0%	3.33
CFRP bar	14	5.3%	0.21	4.0%	7.2%	8.2%	1.55
stainless steel bar	14	6.2%	0.24	3.3%	8.1%	23.5%	3.79

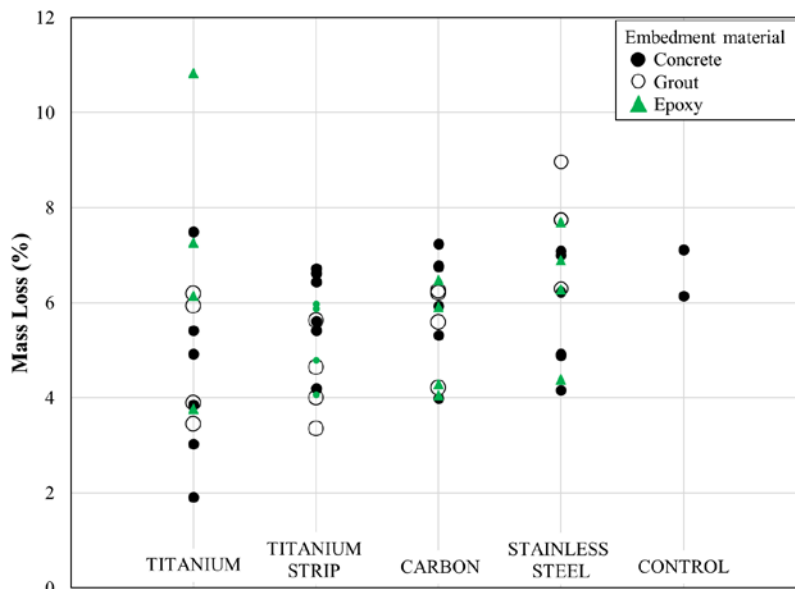


Figure 2.14 Average mass loss over 152 mm length due to corrosion of all specimens

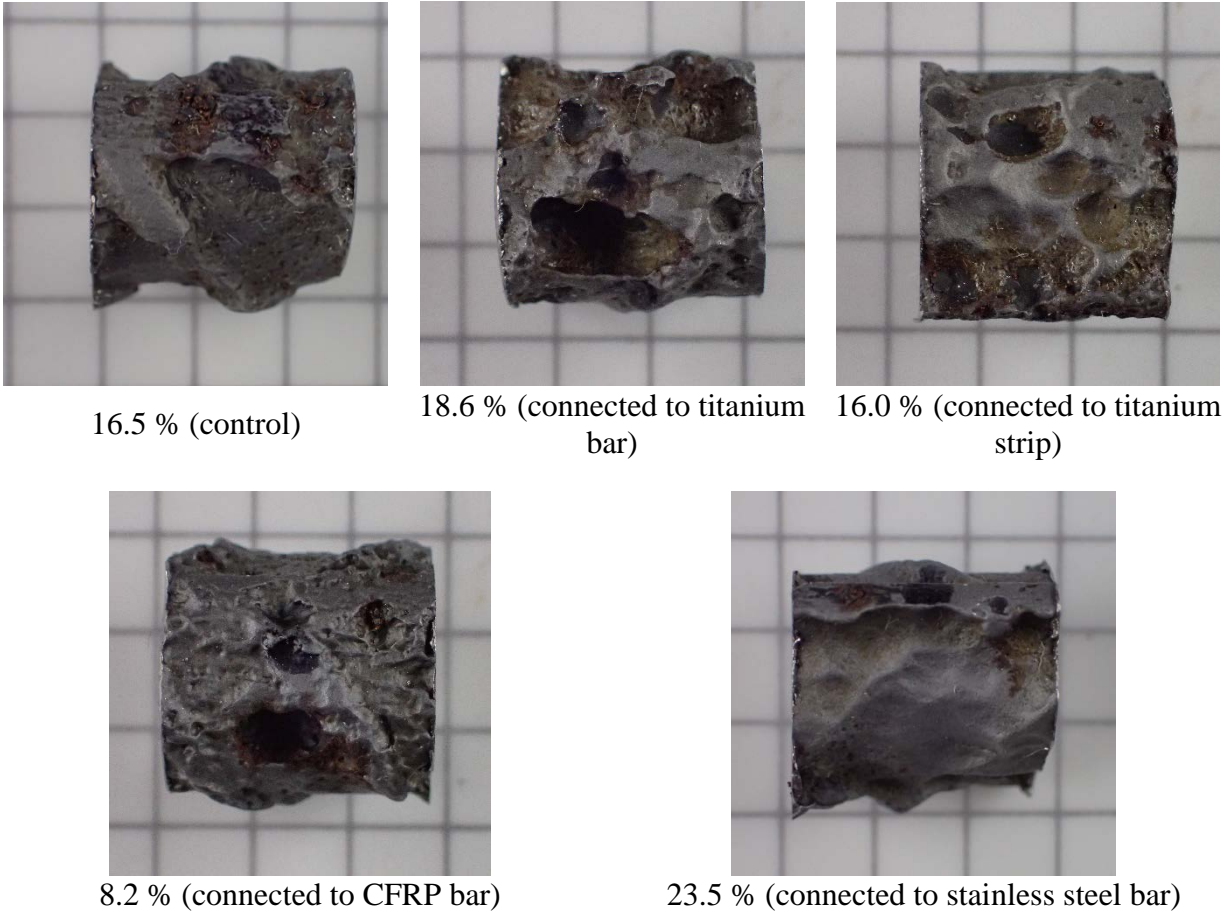


Figure 2.15 Mass loss for 12.6 mm representative sections of ASTM A615 bars

2.3.4 Mass Loss of Electrically Connected Bars

The electrically connected specimens (see Table 2.2 and Figure 2.5) should ensure a galvanic cell develops if one was likely. There was no statistical difference between the performance of these specimens and those in which the circuit is closed through embedment. This result reinforces the conclusion that no galvanic corrosion process was present in the test program.

2.4 SUMMARY OF GALVANIC CORROSION TEST PROGRAM

The analysis of the Macrocouple testing suggest that there is indeed a statistical difference in corresponding readings when considering all factors as listed in Figure 2.16 apart from separation (factor C) between the NSM material and the black steel. The data from the macrocouple tests suggest that there is a statistical difference in the response associated with each set of specimens. The graphs in the interaction plots shown in Figure 2.16 display the variation in means between different factors in terms of the average macrocouple readings. When considering separation as a factor that may influence the current at the time the data was collected, it can be seen that there are essentially no deviations seen in the plots. This is contrasted when considering that the material may influenced the readings as seen where in each case the greatest difference in average current is related to the material, with stainless steel having the greatest impact on current whereas both forms of the titanium alloy have negligible if any effect on the average current readings. Only the embedment and period had any significant impact. Interestingly the grout had the greatest impact when considering embedment. The factor of time or in this case period, the interaction plot shows a strong agreement with the Cor-Map results in that periods 2,3, and 4 had the greatest interaction in affecting the current readings. This aligns well with the previous statement of the chloride-rich cubes becoming washed out with time and the impact of the redox process.

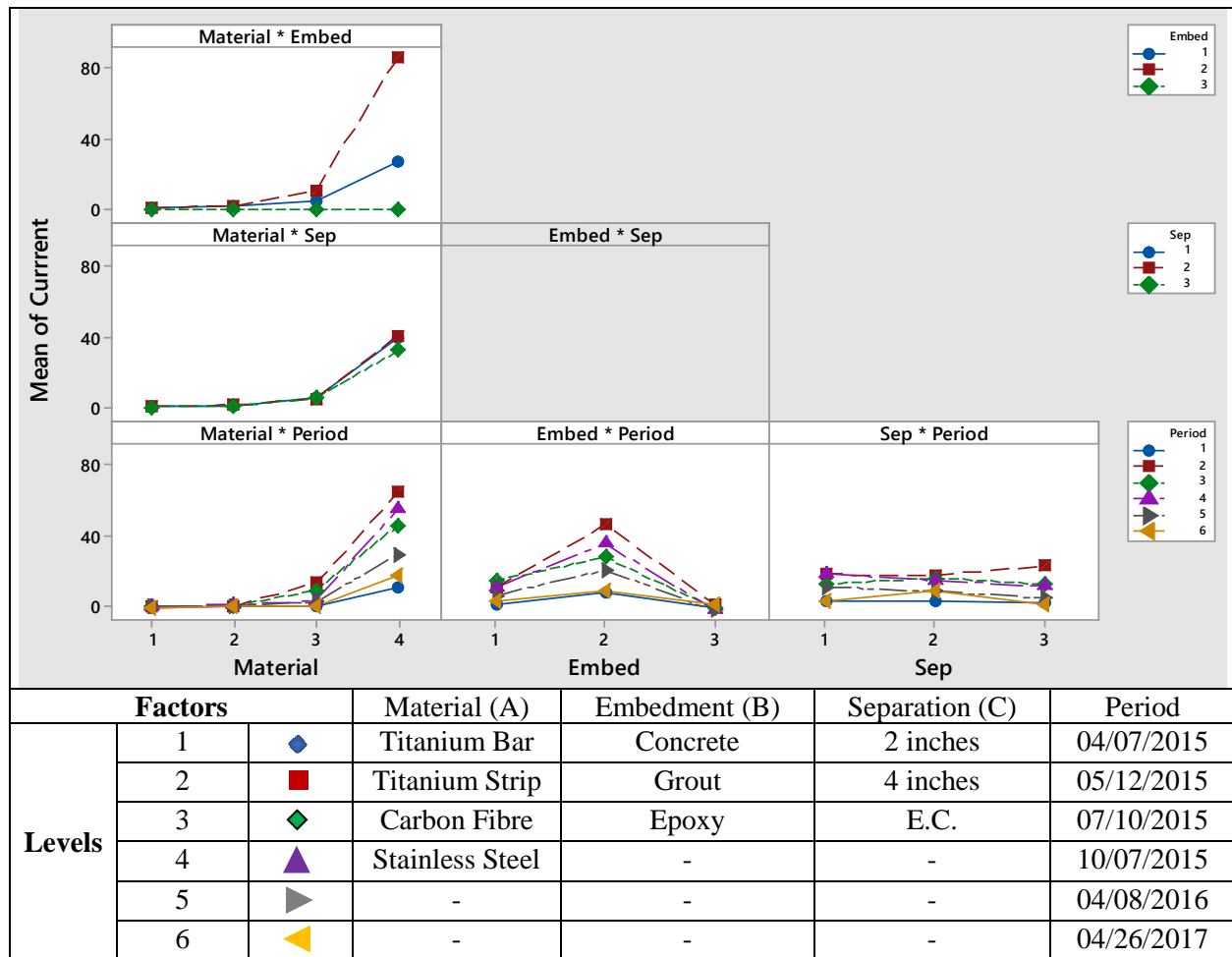


Figure 2.16 Interaction plot for current

The comparison of interest in this study is as follows: *does the presence of titanium accelerate or result in greater steel corrosion than other materials coupled with mild reinforcing steel; that is, does a galvanic cell develop?* For the conditions tested, as expected (and intended), corrosion was present in all specimens. There was no evidence that the presence of 6Al-4V titanium reinforcing bars in close proximity to (or in electrical contact with) A615 steel reinforcing bars results in any change in the rate or nature of corrosion. Interestingly, the use of 2205 duplex stainless-steel bars with A615 steel did exhibit evidence of an active galvanic corrosion effect.

3.0 TITANIUM REINFORCING BAR MECHANICAL AND GEOMETRIC CHARACTERIZATION

This chapter reports the material and geometric characterization of the titanium, steel and GFRP bars used in the remainder of the study (excluding Chapter 2). All bars are nominally US #5 bars (15.9 mm (5/8 in.) diameter); actual dimensions are described in Section 3.2.

3.1 MECHANICAL PROPERTIES OF REINFORCING BARS

Various codes and standards provide definitions of mechanical properties of concrete reinforcing bars. Properties which define strength and ductility include: minimum or lower bound yield strength, maximum or upper bound yield strength, length of the yield plateau, strain at the end of the yield plateau, tensile strength, uniform elongation, total elongation, and ratio of tensile strength-to-yield strength. Figure 3.1 provides a reference for some of the tensile properties in the form of an idealized stress-strain curve. The typical design consideration for steel reinforcing bars is yield strength.

The use of higher material strengths, must be evaluated in terms of their impact on design criteria [e.g. Shahrooz et al. 2014]. It was not until the 1960's that the 'typical' yield strength for steel reinforcement in concrete structures increased from $f_y = 276$ MPa to $f_y = 414$ MPa. Today

strengths of 690 MPa are permitted in design [ACI 318 and AASHTO LRFD] and those in excess of 827 MPa are common in the marketplace. With these higher strength bars, design codes limit the strength that can be used in design in order to maintain established behavior models and serviceability-related requirements. Although these limits are given in terms of yield strength (e.g., $f_y \leq 690$ or 414 MPa), they really reflect strain limits. Strains are proportional to steel stress, in which case achieving higher stresses results in greater strains and more cracking which may also affect bond and other performance parameters, limiting the stress that may be achieved. In steel reinforced concrete design, steel stress is often used in requirements for strain control; this is conventional since the Young's modulus of steel is constant ($E_s = 200$ GPa).

Glass fiber reinforced polymer (GFRP) reinforcement, on the other hand is linear to failure and considerably less stiff than steel (Figure 3.2). Its design (ACI 440.2) is based more on stiffness than on strength although is also limited in order to maintain behavior models and serviceability-related requirements.

Titanium, being stronger, but less stiff than steel (Figure 3.2) will also require design approaches that balance performance with maintaining mechanics and serviceability-related requirements including:

- 1) Respecting concrete compression stress limits while permitting greater curvature resulting from lower reinforcement modulus.
- 2) Ensuring bond between reinforcement and concrete is maintained through large strains and associated concrete cracking.
- 3) Maintaining acceptable deflections and practical crack widths and spacings.

These issues will be described at length in Chapter 6. This chapter reports the mechanical characterization of the titanium, steel and GFRP bars used in the remainder of the study (excluding Chapter 2).

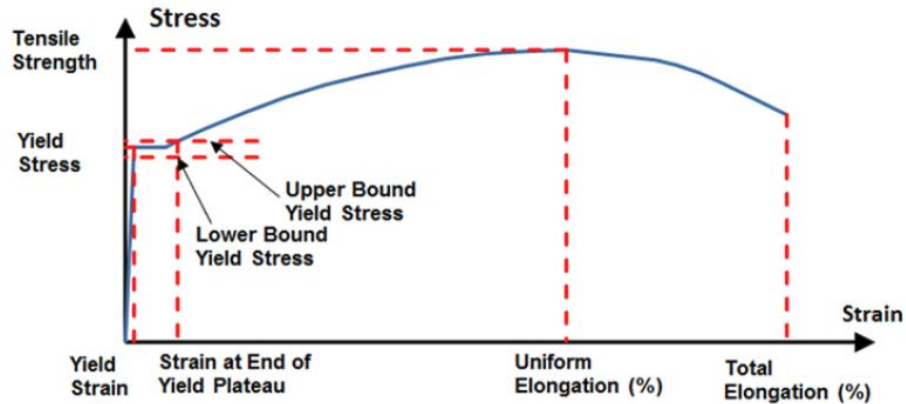


Figure 3.1 Idealized characteristics of typical stress-strain curve [Kelly et al. 2014]

3.1.1 Experimentally determined mechanical behavior of bars in this study

Tension tests of three heats of as-received titanium reinforcing bar were conducted. An additional batch of heat 1 bars that were annealed subsequent to rolling were also tested. Other than the material being titanium, the tensions tests are compliant with ASTM A370-14 (including Annex A9) as referenced by ASTM A615-16. Yield was determined using the 0.2% offset method. The results are summarized in Table 3.1 and representative stress-strain curves are shown in Figure 3.2. Also shown in Table 3.1 and Figure 3.2 are mechanical properties for the steel (single heat for all testing) and GFRP bars used in the bond test program. In all subsequent calculations, measured material properties are used. Nominal values of modulus are used: $E_s = 200$ GPa and $E_{Ti} = 114$ GPa.

The titanium bars are seen to have a similar behavior to steel bars and can be reasonable modeled for design as being elastic-perfectly plastic as is done for steel [ACI 318]. The titanium bars tested do not exhibit a great deal of strain hardening and exhibit considerably lower ultimate strains than steel. Nonetheless, the ultimate elongation of the titanium bars exceeds the requirements for steel bars [ASTM A615]; thus, are sufficiently ductile.

Table 3.1 Mechanical properties of reinforcing bars

	Titanium				Steel	sand-coated GFRP ²	ribbed GFRP ²
	heat 1	heat 1 annealed	heat 2	heat 3	heat 1		
number of tests	6	5	5	5	6 ³	8	n.r.
yield strength, F_y	1055 MPa 153.0 ksi	1044 MPa 151.4 ksi	1090 MPa 158.1 ksi	998.7 MPa 144.7 ksi	464 MPa 67.3 ksi	-	-
COV	0.009	0.009	0.009	0.005	0.046	-	-
modulus of elasticity, E	101.6 GPa ¹ 14740 ksi	107.3 GPa ¹ 15560 ksi	100.6 GPa ¹ 14587 ksi	94.27 GPa ¹ 13673 ksi	176.9 GPa ¹ 25660 ksi	48.4 GPa 7020 ksi	47.6 GPa 6911 ksi
COV	0.034	0.037	0.059	0.051	0.076	0.015	n.r.
tensile strength, F_u	1092 MPa 158.4 ksi	1082 MPa 156.9 ksi	1133 MPa 164.3 ksi	1054 MPa 152.9 ksi	740 MPa 107.3 ksi	738.6 MPa 107.1 ksi	780.1 MPa 113.1 ksi
COV	0.008	0.011	0.009	0.003	0.022	0.022	0.036
ultimate elongation ³	0.161	0.176	0.093	0.084	0.257	0.0153	0.0161
COV	0.158	0.067	0.121	0.042	0.206	0.019	n.r.

¹ determined from clip gage – lower than typically assumed values of 114 GPa for titanium and 200 GPa for steel

² QA tension tests reported by manufacturer; n.r. = not reported

³ n=5 for modulus of elasticity due to slippage in the grips

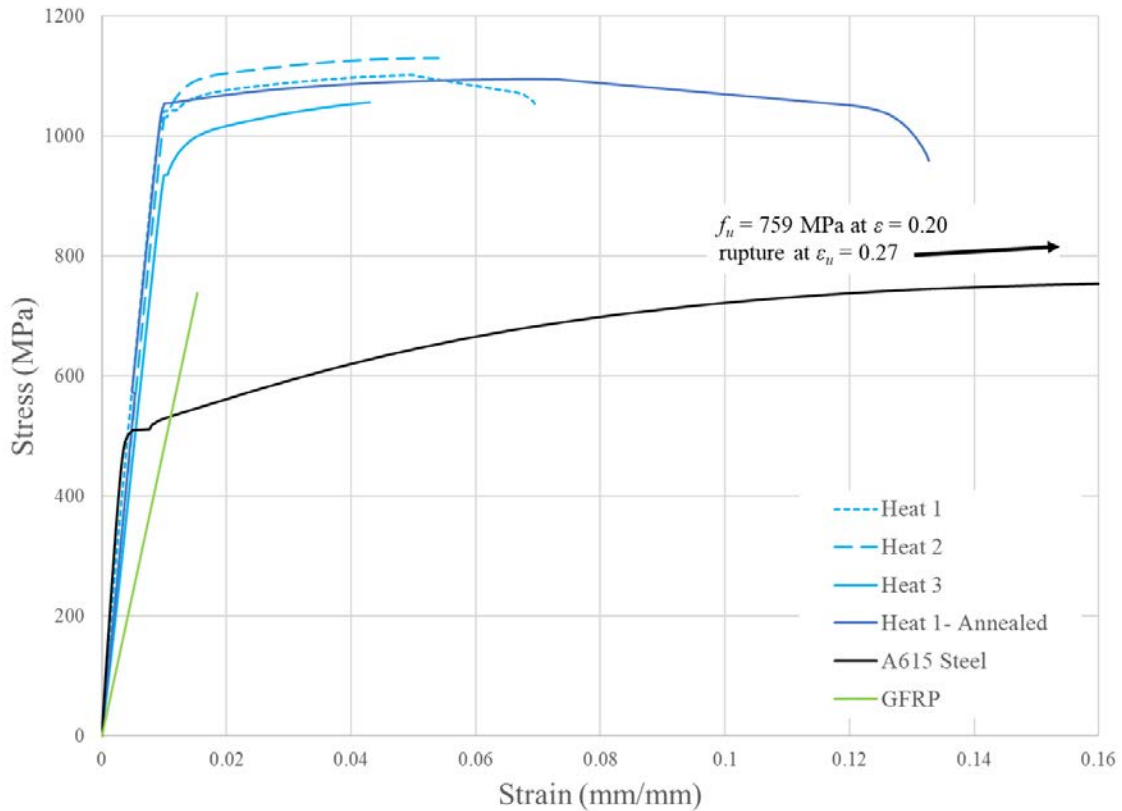


Figure 3.2 Representative experimentally determined stress-strain curves.

3.1.2 Fatigue Behavior

Fatigue is the progressive, localized weakening of a material by which cracks initiate and propagate under cyclic loading. Fatigue cracking generally results from stress that are well below the static yield strength of the material. These cracks initiate at points of concentrated strain and propagate under cyclic tension. The fatigue strength of a material is the greatest repeated transient stress range (S) that may be sustained for a given number of stress cycles (N). The inclusion of surface deformations intended to improve bond performance in reinforcing bars may adversely affect fatigue resistance. The combination of material defects typical in all engineering

materials and reinforcing bars deformations provides the perfect initiation site for fatigue cracking. Indeed, the conventional fatigue stress limit for deformed black steel reinforcing bars is less than about 150 MPa (AASHTO LRFD) whereas the same limit for a “polished” specimen will typically exceed 400 MPa. That is to say, there is a ‘notch effect’ attributed to the rolled deformations.

Titanium is known to have excellent fatigue resistance; however, no data is available for rolled titanium reinforcing bars. The fatigue stress limits for smooth Grade 5 titanium bar fall about 40-50% when the bar is notched [Boyer 1986]; thus, the effect of rolling deformations for titanium reinforcing bars warrants investigation.

A pilot study of 18 tension-tension fatigue tests [ASTM E466-15] were conducted as reported in Table 3.2 and summarized in Figure 3.3. All tests were conducted in an identical manner. As-received deformed bars were inserted into hydraulic wedge grips and clamped. A gage length of 51 mm (2 in.), corresponding to 3.2 bar diameters ($3.2d_b$), was maintained between grip faces. Specimens were loaded to the midpoint of their fatigue range (i.e. average of maximum and minimum loads) and cycling began at a rate of 20 Hz. Testing continued to failure or runout (defined as is typical in structural engineering applications as 2 million cycles).

All stresses are reported based on nominal cross-sectional area of a #5 bar, 200 mm² (0.31 in²). Two ‘target stress’ ranges were used: 165 MPa and 331 MPa (24 and 48 ksi). 165 MPa is the maximum fatigue stress range permitted in conventional Grade 40, 60 or 75 steel reinforcing bars by AASHTO [2017]. 331 MPa was selected as twice this value since titanium bars are nominally twice the strength of steel. In all cases (but one), the minimum stress was approximately 69 MPa (10 ksi).

Six specimens of #5 ASTM A615 steel were tested as a control for the test protocol which was typical of reinforcing bar fatigue testing reported in the literature. For deformed steel reinforcing bar tested in air, the following general equation is most often used to describe fatigue behavior [Helgason and Hanson 1974]: $\log N = 6.969 - 0.0055S$ (where S is expressed in MPa units; $\log N = 6.969 - 0.0383S$ in ksi units). It is seen in Figure 3.3, that the ASTM A615 specimens tested correlated well with this relationship thereby validating the test set-up and procedure.

Despite their higher strength, the titanium bars exhibited poor fatigue performance – poorer than expected and observed for steel bars.

Table 3.2 Fatigue test results

Material	R _r (Eq. 3.1)	S ^a (MPa)	N
ASTM A615 <i>F_y = 464 MPa</i> <i>F_u = 740 MPa</i>	0.079	163	565,597
		164	2,200,000 ^b
		162	2,007,129 ^b
		329	331,986
		331	108,044
		328	156,040
Ti (Heat 3) <i>F_y = 999 MPa</i> <i>F_u = 1054 MPa</i>	0.123	167	335,597
		171	353,104
		176	177,446
		351	21,922
		326	23,431
		327	22,330
annealed Ti (Heat 1) <i>F_y = 1044 MPa</i> <i>F_u = 1082 MPa</i>	0.050	169	629,768
		166	416,133
		165	2,021,387 ^b
		329	63,303
		328	48,022
		327	56,710

^a nominal stress range calculated with $A_{bar} = 200 \text{ mm}^2$

^b runout – tests stopped at $N > 2,000,000$ shown

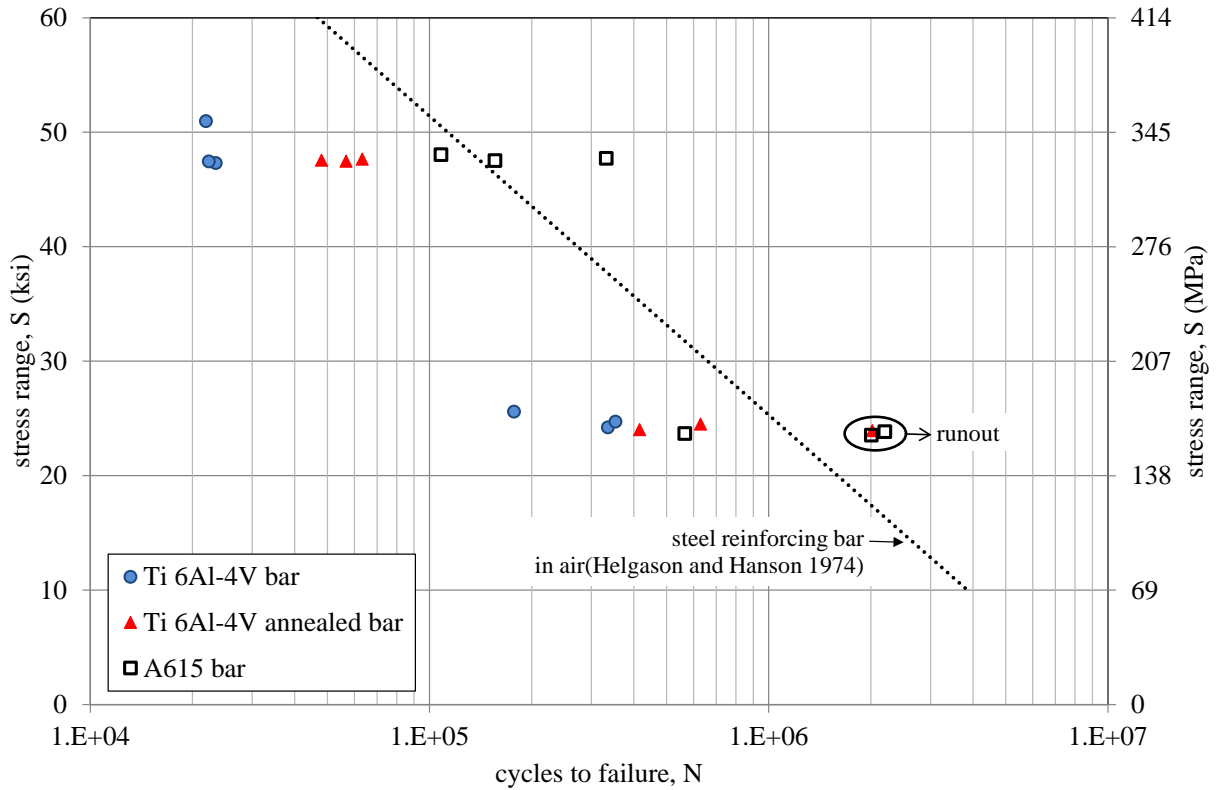


Figure 3.3 S-N results

3.1.3 Ductility Characterization

Reinforcing bars often are required to be bent. In order to have minimal impact on reinforcing bar placement, the bend diameters should be as small as possible without compromising the bar strength. Standard bend diameters are established for steel reinforcing bars [ASTM A615]. The basis of these is that a bar should have the ability to be bent 180° around a pin of specified diameter without cracking on the exterior of the radius of the bent portion of the bar. ASTM A370-14 Annex 9 provide a basis for assessing this requirement and, by extension, for determining reinforcing bar ductility. ASTM A615 prescribes minimum pin diameters around which a bar must be bent and not exhibit fracture or cracking [ASTM E290-14]. Minimum bend

diameters for a #5 bar are $3.5d_b = 56$ mm (2.2 in.) and $5d_b = 80$ mm (3.2 in.) for Grades 40-60 and Grades 75-100, respectively [ASTM A615-16]. It is noted that nominal bar diameters (d_b) are used and the pin diameter is the inside diameter of the resulting bent bar. While many factors affect ductility determination, steel reinforcing bars are conventionally cold bent in a shop environment on as-delivered material. So as not to impart a residual tension in the bar, the bending apparatus is designed to permit unrestricted movement of the bar at points of contact (usually accomplished through the use of pins that are allowed to rotate). In order to “pass” a bending test, there should be no evidence of cracking or surface irregularities at the extreme tensile face of the bend.

Because one envisioned application of NSM titanium are “staple-like” reinforcing bars [Amneus et al. 2014], a small bend diameter is desired so as to simplify installation and potential interference of the staple bend with existing reinforcement.

Titanium bars from Heat 3 were bent through 90° around diameters of $2d_b = 32$ mm (1.25 in.), $4d_b = 64$ mm (2.5 in.), and $6d_b = 95$ mm (3.75 in.) and the titanium was examined for bend-related damage [ASTM E290-14]. A testing platform consistent with ASTM A370-15 Annex 9 and in compliance with ASTM E290-14 for the ‘semi-guided bend test arrangement C’ (one end held – force applied near mandrel) was used. As expected, at room temperature, a brittle failure of the titanium bar resulted long before reaching a 90° bend; titanium bars cannot be cold-bent. As prescribed by the bar manufacturer, using an oxy-acetylene torch and ‘temperature crayons’ to monitor temperature, the bars were heated to 482°C (900°F) and bent. Using the temperature crayons, the temperature achieved is accurate to approximately $\pm 28^\circ\text{C}$ (50°F).

In all instances bending through 90° was possible however, once cooled, the bar exhibited a crack at the root of at least one deformation around the outside (tension side) of the bend

(Figure 3.4). The severity of the cracks (as expected) was inversely proportional to the bend diameter (Figures 3.4b-d). Additionally, the cracks are believed to have formed during the bar cooling (bars were cooled in ambient conditions). The very sharp transition from the bar surface to lug (almost a 90° re-entrant corner for the bars in Heat 3) affected this behavior. Although a ‘rounder’ transition, as is typical in steel reinforcing bars, may mitigate the observed cracking, bends will still require the application of significant heat making field bending titanium bars impractical.



a) profiles of samples cut from 90° bends with $6d_b$, $4d_b$, and $2d_b$ diameters (top to bottom)



b) pin diameter = $2d_b$



c) pin diameter = $4d_b$



d) pin diameter = $6d_b$

Figure 3.4 Cracked surfaces resulting from bend test

3.2 GEOMETRIC CHARACTERIZATION

Manufacturers of steel reinforcing bars have largely adopted very similar production characteristics in order to be compliant with the requirements of ASTM A615. This includes dimensional tolerances as well as lug or surface deformation geometry. These deformations provide most of the mechanical bond transferring force between the bar and the surrounding concrete (this will be described further in Chapter 4). Deformation requirements are to some extent empirical – deformations are demonstrated to be capable of fully developing steel reinforcement having a certain yield strength when embedded a prescribed “development length”; design codes are calibrated based on these values and are therefore reinforcing steel-specific in a sense.

The requirement for ‘standard’ deformations on bars dates to the research performed at the National Bureau of Standards (now the National Institute of Standards and Technology) by Clark [1946, 1949]. Clark, and other researchers since [Soretz and Holzenbein 1979, Vos 1983, Choi et al. 1990, Lorrain et al. 2010, Farshadfar et al. 2014], have demonstrated that the “relative rib area”, R_r , described by Equation 3.1, is a good indicator of bond strength between reinforcing steel and concrete [ACI 408.3R 2009].

$$R_r = (\delta/s_r) (1 - \Sigma \text{gaps}/p) \quad \text{or} \quad R_r = (\delta/s_r) (1 - \Sigma B_n/360^\circ) \quad (3.1)$$

Where: δ = average height of deformations

s_r = average longitudinal spacing of deformations

$\sum gaps$ = sum of the lengths of the gaps or chords between edges of deformations, plus the width of any continuous longitudinal protrusions used to represent the grade of the bar

p = nominal perimeter of the bar

$\sum B_n$ = sum of the chord angles between edges of deformations relative to the bar axis inclusive of any continuous longitudinal protrusions used to represent the grade of the bar; thus $\sum gaps/p = \sum B_n/360^\circ$

Although the ratio R_r is not implemented into ASTM A615, by combining the minimum ASTM A615 requirements for bar geometry (Table 3.4), one infers a minimum required value of $R_r \geq 0.05$. The same requirements are set forth in ASTM A706 (low alloy bars) and A1035 (low carbon, chromium steel bars). An important distinction is that suitable values for R_r , or the prescribed deformation geometry prescribed by ASTM, are intended for use with steel materials having a modulus of 200 GPa embedded in “conventional” concrete. The lower modulus of titanium may result in different rib ratio limits in order to achieve adequate performance or performance similar to steel. This study will attempt to address this to the extent possible using the limited variation of titanium bar deformations available. It is interesting to note that GFRP reinforcing bars do not have prescribed deformations but must be shown to provide adequate bond [ACI 440.1]. This approach has led to a number of different approaches to providing bond for GFRP bars including deformations, helical shapes and sand-coating bars.

The following sections report geometric properties for all titanium, steel and GFRP bars used in subsequent bond tests.

3.2.1 Cross Sectional Area

Cross sectional area was determined using the immersion method (Archimedes principle). The volume of accurately measured short lengths of bar were determined. Specimens were cut from the bars and faced in a lathe to permit accurate length measurements; lengths of 6.4 and 50.8 mm (0.25 and 2 in.) were used. Specimens were suspended by a thread in a beaker of water placed on a precision scale. The weight of the beaker before and after introduction of the titanium specimen is found and, using the density of water, the volume displaced by the specimen is determined. The volume is divided by the precisely measured specimen length to determine cross sectional area. Specimen density is found by dividing the mass of the specimen by the calculated volume. Nominal diameter was measured using calipers and multiple measuring points around the specimen. The geometric properties of the titanium bars are given in Table 3.3.

Table 3.3 Geometry of #5 titanium bars

	Nominal #5 bar	Heat 1		Heat 2		Heat 3	
		n = 10	COV	n = 6	COV	n = 5	COV
cross section area	200 mm ² 0.31 in ²	223 mm ² 0.347 in ²	0.041	215 mm ² 0.335 in ²	0.016	236 mm ² 0.366 in ²	0.010
diameter	15.9 mm 0.625 in	16.85 mm 0.67 in	0.021	16.55 mm 0.65 in	0.008	17.35 mm 0.68 in	0.005
density	-	4466 kg/m ³ 278 lb/ft ³	-	4433 kg/m ³ 276 lb/ft ³	-	4407 kg/m ³ 274 lb/ft ³	-
weight	-	0.995 kg/m 0.669 lb/ft	-	0.953 kg/m 0.641 lb/ft	-	1.040 kg/m 0.699 lb/ft	-

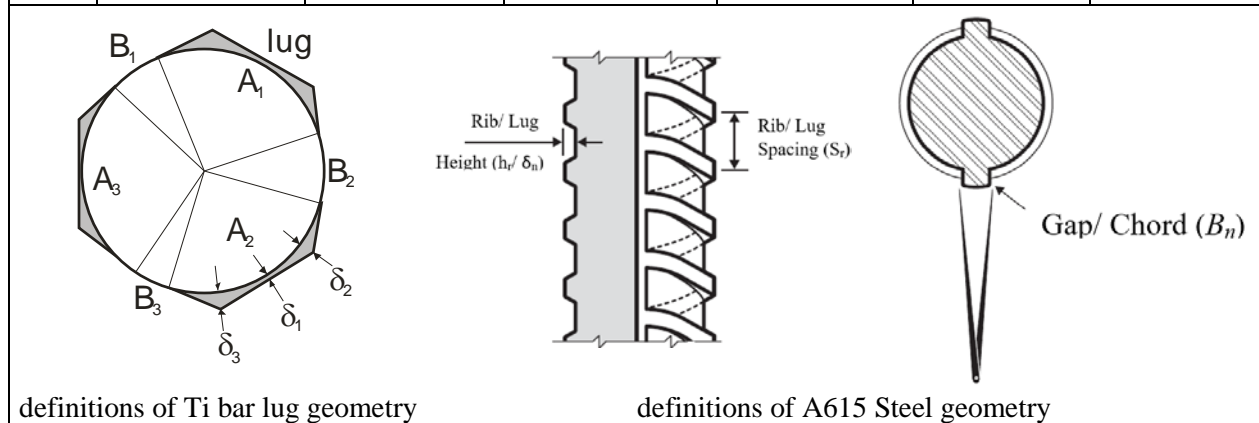
Based on ASTM A615-16, the titanium bar size is marginally larger than a #5 bar having a specified cross section area of 200 mm² (0.31 in²) and nominal diameter of 15.9 mm (0.625 in.). The next standard bar size is #6, having an area of 284 mm² (0.44 in²) and nominal diameter 19.1 mm (0.75 in.). The bars are therefore nominally #5 bars. In all further discussion, unless otherwise noted, the nominal cross-sectional area of 200 mm² will be used when calculating stress and the nominal value of bar diameter, $d_b = 15.9$ mm, will be used.

3.2.2 Deformation Geometry

Deformation geometry of all ribbed bars tested was assessed against the requirements of ASTM A615-16 summarized in Table 3.4. Samples for each heat were taken by numbering the individual bars received and then using a random number generator to select five bars from the lot. Those five bars were further divided along their length without measurement to select two areas per bar from which to collect detailed measurements. All data is based on measurements taken from 10 randomly selected samples per heat. Also shown in Table 3.4 is the rib ratio, R_r , defined in Eq. 3.1.

Table 3.4 Deformation (lug) geometry of #5 A615 steel and titanium bars

ASTM A615	Requirement	A615 Steel		Heat 1		Heat 2		Heat 3		Ribbed GFRP	
7.2	$A_n > 45^\circ$	$A_{n,min} = 156^\circ$	OK	$A_{n,min} = 95^\circ$	OK	$A_{n,min} = 76^\circ$	OK	$A_{n,min} = 103^\circ$	OK	$A_{n,min} = 165^\circ$	OK
7.2	if $A_n < 70^\circ$ opposite deformation is reversed	n/a	OK	n/a	OK	n/a	OK	n/a	OK	n/a	OK
7.3	lug spacing, $s_r < 0.7d_b$	$0.63d_b$ 10.00 mm 0.393 in.	OK	$0.60d_b$ 9.46 mm 0.372 in.	OK	$0.59d_b$ 9.37 mm 0.369 in.	OK	$0.60d_b$ 9.48 mm 0.373 in.	OK	$0.46d_b$ 7.37 mm 0.290 in.	OK
7.4	chord $< 12.5\%$ perimeter i.e., $B_n < 45^\circ$	$B_{n,max} = 23.6^\circ$	OK	$B_{n,max} = 33.8^\circ$	OK	$B_{n,max} = 50.8^\circ$	NG	$B_{n,max} = 17.7^\circ$	OK	$B_{n,max} = 14.6^\circ$	NG
7.4	Σ chord $< 25\%$ perimeter i.e., $\Sigma B_n < 90^\circ$	$\Sigma B_n = 46^\circ$	OK	$\Sigma B_n = 77^\circ$	OK	$\Sigma B_n = 132^\circ$	NG	$\Sigma B_n = 50^\circ$	OK	$\Sigma B_n = 28^\circ$	NG
7.5	lug height $\delta = \Sigma \delta_n / 3 > 0.71$ mm	0.92 mm 0.036 in.	OK	0.62 mm 0.024 in.	NG	0.49 mm 0.019 in.	NG	1.37 mm 0.054 in.	OK	0.66 mm 0.026 in.	NG
rib ratio	R_r (Eq. 3.1)	0.079		0.050		0.033		0.123		0.082	



From the perspective of geometry, the titanium bars from Heat 1 are compliant with #5 ASTM A615 deformed reinforcing bar with the exception of the lug heights (ASTM A615 Section 7.5). Whereas the bars from Heat 2 are non-compliant based on both lug height and circumferential coverage of the lugs (ASTM A615 Sections 7.4 and 7.5). Because these bars are rolled, these geometric properties are related; improving one will improve the other. Heat 3 has

quite large and well-defined lugs, easily meeting the requirements of ASTM A615. Both the steel and ribbed GFRP bars used in the study also satisfied ASTM A615 requirements.

3.2.3 Lug Height Variation

Lug height is defined by ASTM A615-16 as the average of three measurements (shown as δ_1 , δ_2 and δ_3 in Table 3.4). It was observed that the depth of the deformations (lugs) vary on the three sides of a bar (see Figure 3.5). This results from the bar not being perfectly centered within the three, 120°-oriented, mill rolls used to form the bar. Thus, there are ‘deep’ and ‘shallow’ lugs as shown in Figure 3.5. In some cases, particularly in heat 2, the value of δ_1 is very close to zero in the shallow lugs. Figure 3.6 displays sample deformations from typical A615 steel and each heat of titanium. Table 3.5 summarizes the lug height measurements taken from ten randomly selected lugs on each of three randomly selected bars for each of titanium heats 1, 2 and 3.



a) deep deformations on Ti bar from Heat 1

b) shallow deformations on Ti bar (rotated 120° from Figure a)

Figure 3.5 Samples of ASTM A615 #5 bar (left) and titanium bar (right).



#5 A615 steel



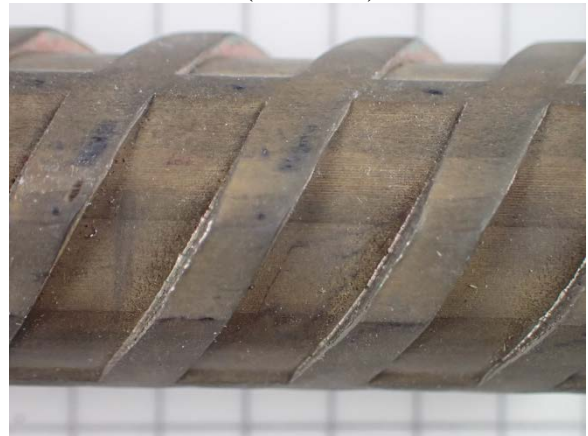
heat 1 #5 titanium



heat 1 (annealed) #5 titanium



heat 2 #5 titanium



heat 3 #5 titanium

Figure 3.6 Samples of A615 steel and each heat of titanium tested

Table 3.5 Measured lug heights for titanium bars

	δ_1	δ_2	δ_3	$\delta = \Sigma\delta_n/3$
Heat 1				
average	0.75 mm 0.030 in.	0.34 mm 0.013 in.	0.76 mm 0.030 in.	0.61 mm 0.024 in.
COV	0.057	0.366	0.077	0.106
minimum	0.67 mm 0.026 in.	0.13 mm 0.005 in.	0.65 mm 0.026 in.	0.51 mm 0.020 in.
maximum	0.82 mm 0.032 in.	0.51 mm 0.020 in.	0.82 mm 0.032 in.	0.69 mm 0.027 in.
Heat 2				
average	0.64 mm 0.025 in.	0.22 mm 0.009 in.	0.60 mm 0.024 in.	0.49 mm 0.019 in.
COV	0.003	0.112	0.654	0.220
minimum	0.53 mm 0.021 in.	0.04 mm 0.002 in.	0.05 mm 0.002 in.	0.28 mm 0.009 in.
maximum	0.75 mm 0.030 in.	0.51 mm 0.020 in.	0.80 mm 0.032 in.	0.69 mm 0.027 in.
Heat 3				
average	1.42 mm 0.056 in.	1.42 mm 0.056 in.	1.29 mm 0.051 in.	1.37 mm 0.054 in.
COV	0.084	0.096	0.061	0.042
minimum	1.22 mm 0.048 in.	1.17 mm 0.046 in.	1.08 mm 0.043 in.	1.27 mm 0.050 in.
maximum	1.66 mm 0.065 in.	1.65 mm 0.065 in.	1.45 mm 0.057 in.	1.47 mm 0.058 in.

3.2.4 Variation of Lug Geometry Along Single 3.66 m Length of Bar

A single bar, designated “bar X” from the very beginning of the rolling process of heat 2 illustrated the full degree of variation of deformation observed in heats 1 and 2. Table 3.6 summarizes the measured lug geometry obtained from five stations along bar X. These stations are immediately adjacent the bonded region of the bars in later cube tests.

Bar “Y”, also reported in Table 3.6, was an example of a particularly poor example of rolled deformations from heat 2. This bar will be used in subsequent bond tests to examine poor bond properties.

Table 3.6 Variation of lug geometry along length of bars X and Y (Heat 2)

	Bar X					Bar Y
						
station	2	4	6	8	10	
location	152 mm	812 mm	1470 mm	2130 mm	2790 mm	n/a
	6 in.	32 in.	58 in.	84 in.	110 in.	n/a
section area	232 mm ²	228 mm ²	208 mm ²	206 mm ²	213 mm ²	204 mm ²
	0.360 in ²	0.353 in ²	0.322 in ²	0.319 in ²	0.330 in ²	0.318 in ²
diameter	17.2 mm	17.0 mm	16.3 mm	16.2 mm	16.5 mm	16.1 mm
	0.677 in.	0.669 in.	0.642 in.	0.638 in.	0.650 in.	0.637 in.
$B_{n\ max}$	20.2°	21.7°	58.3°	57.2°	55.1°	58.4°
ΣB_n	57.2°	63.2°	169°	159°	158°	167°
lug height	1.28 mm	1.28 mm	0.36 mm	0.28 mm	0.33 mm	0.27 mm
	0.050 in.	0.050 in.	0.014 in.	0.011 in.	0.013 in.	0.011 in.
rib ratio	0.115	0.113	0.020	0.017	0.020	0.016

3.2.5 Discussion of Observed Deformations

In investigating the as-received bar geometry and the [proprietary] drawings of the mill rolls used to form these, a few issues were noted:

- 1) The as-received bars have a nominal diameter of 16.76 mm whereas the drawings would appear to provide a diameter of 17.26 mm.
- 2) The as-received bars have a flat-topped deformation (see Figures 3.5 and 3.6) whereas the drawings appear to provide a rounded deformation (at a radius of 10.74 mm).
- 3) As described above, it is also observed that the depth of the lugs varies on the three rolls. As shown in Figure 3.5a, a ‘deep’ lug has clear relief from the bar surface at its center whereas a shallow lug (Figure 3.5b) has essentially no relief at its closest point to the bar surface. The drawings show a ‘depth of slot’ of 2.108 mm. This was not apparently achieved.
- 4) The drawings show 3 mm “width”, which is understood to be the space between rolls that forms the ‘rib’ in the bar between deformations. The width of this rib was found to average 3.64 mm (COV 0.077).

Taken together, observations 1 and 2 suggest that the material diameter entering the roll was insufficient to engage the entire anticipated deformation depth. Observation 3 further suggests that the three rolls were not engaging equally. Observation 4 may imply that the diameter of the rolls themselves may be slightly small or vary from roll to roll. The speed at which the bar goes through the single roll also effects its final deformation pattern. By the time heat 3 was fabricated, the bar fabricator had more experience and thus produced a more uniform product.

3.3 SUMMARY OF MATERIAL AND GEOMETRIC CHARACTERIZATION OF TITANIUM REINFORCING BARS

Although the titanium material used in this study behaved as expected in terms of typical axial stress-strain behavior (Figure 3.2), some concerns – believed to result from the deformation rolling operation – were identified: relatively poor fatigue (Section 3.1.2) and ductility (3.1.3) performance. Rolled deformations must be sufficiently ‘large’ (as measured by the rib ratio, R_r , (Eq. 3.1)) to affect bond between the bar and concrete. The deformations, however, appeared to result in a significantly adverse fatigue performance. Although titanium is known for excellent fatigue resistance, the presence of the ‘sharp’ re-entrant corner deformations in Heat 3, led to fatigue performance notable worse than conventional steel reinforcing bars. The roots of the deformations also serve as crack initiators when the titanium bars are bent. Further work must be done to balance the need for marked deformations while minimizing the stress-raising effect of the deformation root.

An additional issue with titanium bars is that they must be bent using the application of heat. This represents an additional (and potentially expensive and cumbersome) process in the bar shop. It also limits the ability to field bend bars – a process required in many applications. Nonetheless, this is not insurmountable. GFRP bars, for instance, must be formed during manufacture in order to be bent and the bends result in significantly reduced capacity of the bar [ACI 440.1R-15].

4.0 BOND CHARACTERIZATION

In a reinforced concrete member, internal equilibrium is achieved as the tension force carried by the reinforcement balances the compression force carried by the concrete. The tension force is transferred to the reinforcement through bond between the reinforcement and concrete into which it is embedded. Bond stresses exist whenever the force in the tensile reinforcement changes. With the exception of unbonded post-tensioned concrete members, design assumptions [ACI 318 and AASHTO LRFD] assume conditions of “perfect bond” through the developed yield stress in the reinforcing. This assumption, implies that strain compatibility is enforced over the entire member and equilibrium is maintained locally at cracks.

To transfer force adequately, there must be a sufficient length of reinforcing bar, known as the development length, over which the bar force is transferred from the concrete to the reinforcing steel. Bond force is developed by chemical adhesion, friction, and mechanical interlock between bar deformations and the surrounding concrete (Figure 4.1a). Adhesion is small, rapidly overcome and therefore neglected. Friction requires the presence of a normal force which is present in prestressed reinforcement (the Hoyer effect) but is negligible in non-prestressed reinforcing. Thus, mechanical interlock is the dominate component of bond strength forming a resultant stress that can be further broken into longitudinal and radial components (Figure 4.1b). The ultimate failure of a reinforced concrete member is a function of the bond

stress, the tensile strength of the concrete, and the concrete cover or bar-to-bar spacing [Wight et al. 2012].

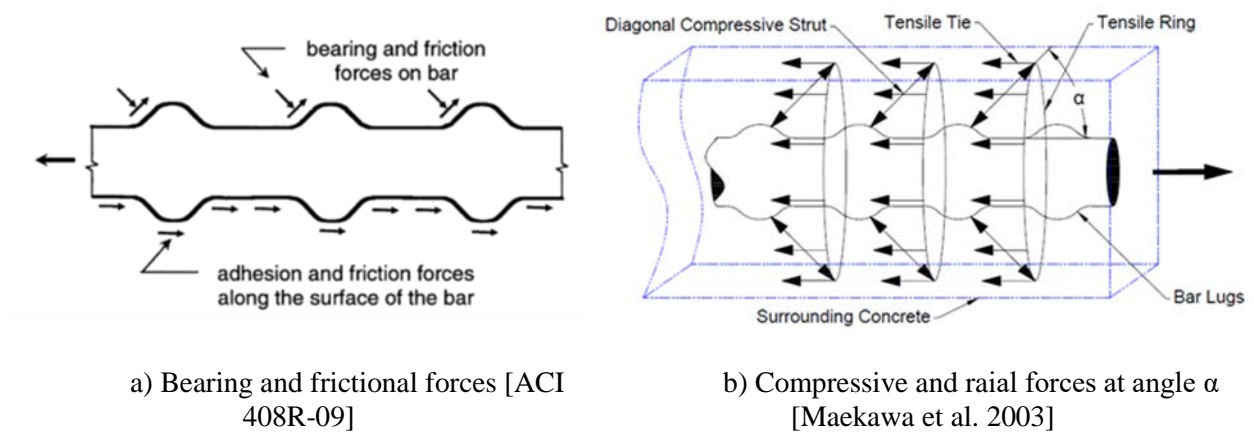


Figure 4.1 Transfer of forces from concrete to reinforcement

Bond of reinforcing steel is conventionally assessed using ‘pull-out’ tests having short embedment lengths (ASTM D7913-14 and similar). Such tests are not appropriate for determining characteristic development lengths and behavior, particularly for non-conventional reinforcing bar geometries; full development length tests such as ‘beam-end’ tests are required for this purpose (ASTM A944 and similar).

The bond mechanism depends on a number of factors including bar size, shape, deformation geometry and elastic modulus. Bond capacity is additionally dependent upon confining concrete strength and the effects of confining reinforcement, if present. When considering titanium reinforcing bars, two issues associated with bond arise:

- 1) The deformations provided may substantially differ in geometry from those used on conventional reinforcing steel resulting in a different stress transfer mechanism and therefore a different capacity. Quantification of the deformations present on the titanium bar used in this study is described in Section 3.2.

- 2) The lower modulus of titanium requires larger strains to develop the same reinforcing stress (by a factor of approximately two) and larger strains still (factor of approximately four) to effectively develop the capacity of the titanium bar; that is, to use the material efficiently. Our present understanding of bond to concrete does not typically consider these larger strains. This issue will be discussed in relationship to reinforced concrete design in Section 6.1.

Rather than address bond stress directly, reinforced concrete design uses the concept of development length. The development length, l_d , is the length of embedment required for the bar stress to increase from zero to the yield strength, f_y ; i.e., to fully ‘develop’ the bar capacity. If the development is inadequate, the bar will either pull out of the concrete (shear failure in concrete along plane of deformations) or the concrete will split as a result of the radial stresses developed. The development length can be expressed by the equation:

$$l_d = f_y A_b / \pi d_b \tau_{avg} = f_y d_b / 4 \tau_{avg} \quad (4.1)$$

Where τ_{avg} is the average bond stress that may be developed along the length l_d of the bar having diameter d_b . In practice, a number of factors contribute to development and the following empirical equation is adopted [ACI 318-14]:

$$l_d = \frac{3f_y d_b}{40} \frac{\Psi_t \Psi_e \Psi_s}{\sqrt{f'_c} \left(\frac{c_b + 40A_{tr}/s_n}{d_b} \right)} \quad (4.2)$$

The $\sqrt{f'_c}$ term accounts for concrete tensile strength, the term in brackets accounts for concrete cover and confinement, and the Ψ terms account for bar coating, size and placement, respectively. Finally, the 3/40 scalar is an empirical value intended to calibrate the equation with experimental results.

Since titanium has a lower modulus and is expected to exhibit greater slip for a given applied load, development equations need to be revised (or verified) for these new conditions.

Indeed, development equations for GFRP bars, while accounting for the same concrete conditions, take on a different empirical form [ACI 440.1R-15] requiring an iterative solution. Since GFRP is linear to failure, the problem is one of determining a development length, l_d , sufficient to develop the design stress, f_{fe} .

$$l_d = \frac{f_{fe} d_b}{\sqrt{f'_c}} \left(\frac{\alpha}{13.6 + \frac{c_b}{d_b} + \frac{340 d_b}{l_e}} \right) \quad (4.3)$$

Once again, familiar terms are present accounting for the same mechanical phenomena. The comparable Canadian code for GFRP-reinforced structures, CSA S806 [2012], also provides a development length equation of the same basic form having an experimentally determined “bar surface profile factor”, k_5 . For GFRP bars for which cover and bar spacing exceed $1.5d_b$ and $1.8d_b$, respectively:

$$l_d = \frac{0.5 k_1 k_2 k_3 k_5 f_f d_b}{\sqrt{f'_c}} \quad (4.4)$$

In which k_1 and k_3 are the same as Ψ_t and Ψ_s in Eq. 4.2.

Based on the experience with GFRP, despite the lower material modulus, bond and development length are considered in a manner similar to steel. Nonetheless, comprehensive testing must be conducted to quantify a particular material’s bond characteristics and strength for use in reinforced concrete structures.

4.1 EFFECTS OF RIB GEOMETRY ON BOND

The possible shapes, sizes and patterns for deformations on a reinforcing bar is nearly unlimited. The various configurations contribute differently to the components of the resulting bond strength of a given reinforcing bar. The properties ranging from shear to adhesion are all factors of the geometric arrangement of the deformations or ribs. In 1979, Soretz and Holzenbein summarized past research with the slogan “The stronger the short ribs, the better”. This requirement lent well to the available materials of the time as well as the effect of deformation size on the bendability of a reinforcing bar. Their research was based on the results of an earlier investigation of more than 1200 pull-out tests with embedment lengths greater than ten times the bar diameter and investigated the influence of the various parameters of the rib ratio as determined by the European definition shown in Figure 4.2 [Rehm 1961] and given by Equation 4.5. The research used specially manufactured bars with a constant inclination angle for the lugs of $\beta = 53^\circ$ to the bar axis while varying the lug heights, a , and spacing, c_s .

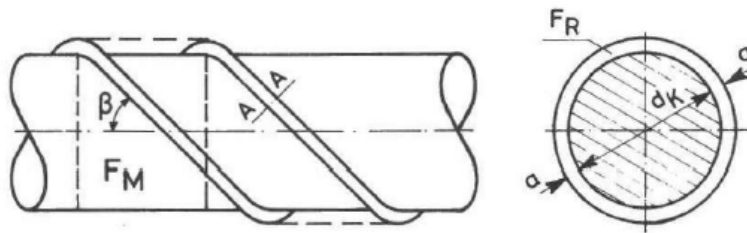


Figure 4.2 Descriptions of lug angles and spacing [Rehm 1961]

$$f_R = \frac{k \times F_R \times \sin \beta}{\pi \times d_b \times c_s} + \frac{i \times a}{j \times d_b} \quad (4.5)$$

Where: F_R = area of the longitudinal section of one lug

β = lug inclination towards the bar axis

k = number of lug series

d_k = nominal diameter

c_s = distance between lugs

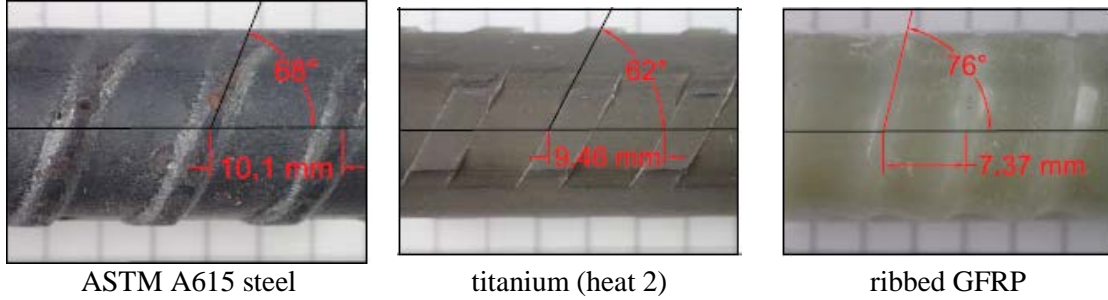
The second term in Equation 4.5 applies only to bars having a helical deformation pattern; for which:

a = height of longitudinal rib

$j*d_k$ = pitch of twist of twisted bars

i = number of longitudinal ribs

The European rib ratio (f_r) and that described by Equation 3.1 (R_r) are similar with the addition of lug inclination and pitch in the European versions. Equation 3.1 also considers the average lug area around the circumference of the bar whereas Equation 4.5 considers only one lug. A comparison of f_r and R_r for bars tested in the present study is shown in Figure 4.3. While these ratios have no physical meaning, the ratio between them is consistent for both formulations (Equations 4.5 and 3.1, respectively). R_r will be used to describe rib ratio in the present study as this is consistent with ACI practice [ACI 408.3R 2009].



Eq. 3.1

$$R_R = \left(\frac{0.92}{10.1}\right) \times \left(1 - \frac{46}{360}\right) \quad R_R = \left(\frac{0.49}{9.46}\right) \times \left(1 - \frac{132}{360}\right) \quad R_R = \left(\frac{0.66}{7.37}\right) \times \left(1 - \frac{28}{360}\right)$$

$$R_r = 0.079 \quad R_r = 0.033 \quad R_r = 0.083$$

Eq. 4.5

$$f_R \approx \frac{2 \times \left(\pi \times 15.6 \times 0.92 \times \frac{156}{360}\right) \times \sin 68^\circ}{\pi \times 15.6 \times 10.1} \quad f_R \approx \frac{3 \times \left(\pi \times 15.6 \times 0.49 \times \frac{76}{360}\right) \times \sin 62^\circ}{\pi \times 15.6 \times 9.46} \quad f_R \approx \frac{2 \times \left(\pi \times 15.6 \times 0.66 \times \frac{165}{360}\right) \times \sin 76^\circ}{\pi \times 15.6 \times 7.37}$$

$$f_R = 0.073 \quad f_R = 0.029 \quad f_R = 0.080$$

Figure 4.3 Rib ratios of bars used in present study

Extensive research up to that point had excluded or considered some parameters as being inconsequential. Some contemporary standards put different weight on different aspects of the rib ratio [Soretz and Holzenbein, 1979]. Research found that deformation height and spacing were related in that simultaneously decreasing the lug height and spacing (i.e., a constant f_R value), in bars having yield strengths ranging from 490 to 618 MPa, resulted in no significant change in bond behavior. This relation also changed the failure type from splitting to excessive slip with the same decrease and constant f_R . The change in lug inclination relative to the bar axis also affected bendability: as the angle β increased, the bendability decreased. It should also be noted that many of the specimens tested in earlier studies were cold worked to produce the twists in the reinforcing bar.

It can be concluded that as the rib ratio decreases and the failure mode changes from longitudinal splitting cracking to slipping, that there is a decrease in radial compressive force at the bar-to-concrete interface. The radial pressure has been extensively investigated by Martin

[1973], Tepfers [1973 and 1979], Eligehausen [1979], and Vos [1983]. This research has determined that the bond stress, f_{bc} , at cracking of the concrete cover along the length of the bar is related to this radial pressure. Tepfers described the cracking resistance using three theories to determine the bond stress as shown in Figure 4.4.

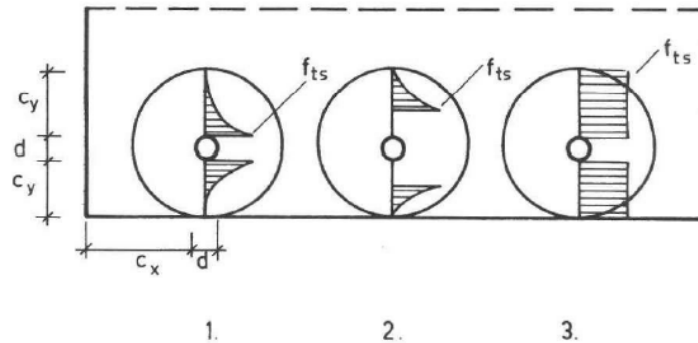


Figure 4.4 The distribution of tangential tensile stresses [Tepfers 1973]

1) Elastic stage
$$f_{bc} = \frac{f_{ts}}{\tau_{g\alpha}} \times \frac{(c_y+d/2)^2 - (d/2)^2}{(c_y+d/2)^2 + (d/2)^2}$$

2) Partly cracked elastic stage
$$f_{bc} = \frac{f_{ts}}{\tau_{g\alpha}} \times \frac{(c_y+d/2)^2}{1.664d}$$

3) Plastic stage
$$f_{bc} = \frac{f_{ts}}{\tau_{g\alpha}} \times \frac{2c_y}{d}$$

Where alpha, α , describes the slope of the lug as shown in Figure 4.5.

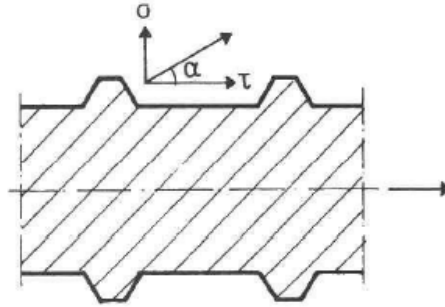


Figure 4.5 Description of the lug angles influence on radial pressure [Vos 1983]

Rehm [1961] found that the compacted concrete powder that forms in front of the rib upon initial slippage of the reinforcing bar produces a new rib face with an angle of 30-40°. This would explain why past research has shown that varying rib faces from 45-90° relative to the surface of the bar result has little influence on bond behavior. This also is relative to the rib spacing in the bar as Rehm determined that concrete crushing extends 5-7 times the length of the rib and to a height as much as twice the rib height [Vos 1983].

Confinement reinforcement transverse to the bar has been reported to increase the influence of the rib ratio. The addition of transverse reinforcement with increased rib ratios have resulted in increased bond strengths. Nonetheless, the ASTM standard tests prescribed for bond assessment do not include reinforcement transverse to the bar being tested. These are A-B comparison tests and thus are conducted under the simplest conditions. The absence of confinement should also yield a lower bound for calculated bond stress. ASTM A944 beam-end test conducted in this study display cracking patterns on the top surface of the specimens which is related to rib ratio and bond characteristics of the bars. The lack of transverse reinforcement (see Figure 4.16b) magnifies the cracking tendencies of the larger rib ratios and the low concrete cover, 38.1 mm (1.5 in.) in this case.

Interestingly, none of the known previous research investigates the contribution of the reinforcing bars modulus of elasticity and only a limited number consider the added contribution of higher strength concretes when related to deformation geometry. In the present study, multiple bar moduli are considered in addition to a significant variation of bar rib geometries.

4.2 BOND CHARACTERIZATION TEST PROGRAM

In this study, ASTM D7913-14 pull-out tests are used to compare the bond behaviors of titanium, steel and GFRP reinforcement. ASTM A944-10 beam-end tests are performed to assess actual development behavior.

All reinforcing bar properties are given in Chapter 3. Three batches of ready-mix concrete were used in a series of pull-out and beam-end tests as described in the following sections. The concrete mix designs and material properties are given in Table 4.1.

Table 4.1 Concrete batch mix designs and material properties

	batch 1	batch 2	batch 3
supplier	Frank Bryan		
mix designation	4000 shot		
date cast	3.21.16	6.27.16	12.6.16
batch size	1.53 m ³ (2 cy)	2.30 m ³ (3 cy)	2.30 m ³ (3 cy)
Mix Design			
Type I/II cement (ASTM C150)	294 kg/m ³ (496 lb/cy)		
fine aggregate (ASTM C33)	688 kg/m ³ (1159 lb/cy) SSD		
3/8 in. gravel (ASTM C33)	1015 kg/m ³ (1710 lb/cy) SSD		
class C fly ash (ASTM C618)	73.6 kg/m ³ (124 lb/cy) (20% cm replacement)		
AE: Axim AE 260 (ASTM C260)	5 oz/cy		
WR: Axim 1000N (ASTM C494)	≈5.56 kg/m ³ (4 oz/cwt)		
water	157 kg/m ³ (265 lb/cy)		
water added on site	≈ 9.5 kg/m ³ (16 lb/cy)	none	≈ 8.3 kg/m ³ (14 lb/cy)
final w/c	0.45	0.43	0.45
target slump	140 mm (5.5 in.)		
target air	6.7%		
unit weight	2227 kg/m ³ (139 pcf)		
7-day compressive strength ¹ (ASTM C39)	22.5 MPa 3260 psi (COV = 0.024)	30.2 MPa (8 day) 4377 psi (COV = 0.12)	19.2 MPa 2792 psi (COV = 0.16)
28-day compressive strength ² (ASTM C39)	$f_c' = 28.3\text{MPa}$ $f_c' = 4100\text{ psi}$ (COV = 0.02)	$f_c' = 43.6\text{ MPa}$ $f_c' = 6320\text{ psi}$ (COV = 0.004)	$f_c' = 43.3\text{ MPa}$ $f_c' = 6285\text{ psi}$ (COV = 0.05)
28-day split cylinder strength ³ 1(ASTM C496)	$2.42\text{ MPa} = 0.46\sqrt{f_c'}$ $350\text{ psi} = 5.47\sqrt{f_c'}$ (COV = 0.11)	$3.43\text{ MPa} = 0.52\sqrt{f_c'}$ $498\text{ psi} = 6.26\sqrt{f_c'}$ (COV = 0.07)	$2.57\text{ MPa} = 0.39\sqrt{f_c'}$ $373\text{ psi} = 4.71\sqrt{f_c'}$ (COV = 0.12)

¹n = 5 for all batches

²n = 5 for batches 1 and 2, n = 4 for batch 2

³n = 5 for batches 1 and 2, n = 3 for batch 3

4.3 PULL-OUT TESTING

Pull-out tests have been widely used in evaluating the bond characteristics of reinforcement. This is primarily due to the ease and repeatability of the testing arrangement. However, the method, using a bonded length of only $5d_b$ has been shown to overestimate the actual average bond stress

for a corresponding full development length [Feldman and Bartlett 2005; Osofero et al. 2014; Gudonis et al. 2014]. Thus, the test is more appropriate as an A-B comparison test rather than a test to establish a design parameter. The pull-out test, described in ASTM D7913-14, includes a length of reinforcing bar cast in a concrete cube or cylinder with both ends exposed. The specimen is placed in a testing arrangement where one end of the bar is loaded in tension while the other is monitored for slip relative to the concrete. While this method is, generally speaking, considered to be the easiest of all the test methods for assessing bond, it also the least realistic. This is because as the bar is loaded in tension, the surrounding concrete is placed entirely into compression. There is also a frictional force acting on the loaded concrete face resulting from the bearing plate and neoprene (when used) which contributes to resisting transverse splitting forces. Whereas in actual service conditions, such as in a flexural member, both the reinforcement and adjacent concrete are in tension.

4.3.1 Test Specimens

Table 4.2 summarizes the pull-out tests conducted for this test program. A minimum of 5 specimens of each material considered and a ‘control’ series of the same ASTM A615 bars were tested with each concrete batch in order to permit normalization of results.

Table 4.2 Pull-out test matrix indicating number of samples tested

#5 bars		R_r	Concrete		
	heat		Batch 1	Batch 2	Batch 3
ASTM A615		0.079	5	5	5
titanium	1	0.050	10	-	-
annealed titanium	1	0.050	-	5	-
titanium	2	0.033	-	5	-
titanium	3	0.123	-	-	10
sand-coated GFRP			5	-	-
ribbed GFRP		0.082	-	-	5
titanium bar X	2	0.017 – 0.115	-	5	-
titanium bar Y	2	0.016	-	5	-

As indicated in Table 4.2, #5 reinforcing bars of titanium, A615 steel, and GFRP (all material properties reported in Table 3.1) were cast into 203 mm concrete cubes (Figure 4.5). All bars have a bonded region 5 bar diameters ($5d_b$), equal to 80 mm (3.15 in.) long. The remaining embedded length is unbonded by placing it within a 19.2 mm I.D. (24.3 mm O.D.) GFRP tube (seen in Figure 4.6a).



a) single titanium reinforcing bar with GFRP tube bond breaker



b) series of cube forms prior to concrete casting



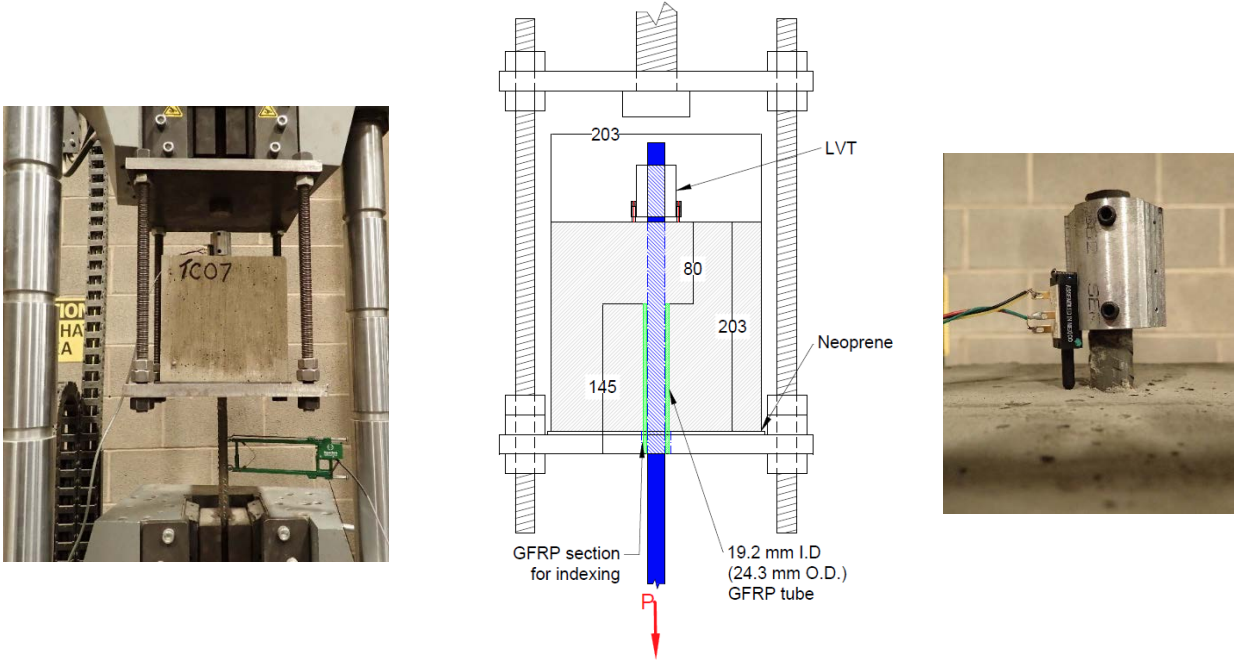
c) cured cubes

Figure 4.6 ASTM D7913-14 test specimens

4.3.2 Test Set-up and Protocol

All pull-out tests are compliant with ASTM D7913-14. A testing apparatus (Figure 4.7a) was fabricated to support the 203 mm concrete cubes while the embedded reinforcing bars were placed into concentric tension to ‘pull out’ the reinforcement. The apparatus was designed to be mounted in a 600 kN (135 kip) capacity universal test machine and to be self-centering with respect to the pull-out test. Slip of the protruding unloaded end of the embedded bar was measured using a custom-fabricated collar and linear position transducer (Figure 4.7b). The transducer has a range of 12 mm and a precision of 0.004 mm. A clip gage was installed on the

loaded portion of the bar (Figure 4.7a) to validate modulus data. Although continuous data was recorded during each test, ASTM D7913-14 defines “control” values of bond strength at specified slips of 0.05, 0.1, and 0.25 mm (0.002, 0.001 and 0.01 in.).



a) test apparatus

b) collar and transducer

Figure 4.7 ASTM D7913-14 test set-up

4.3.3 Test Results

Using the ASTM D7913-14 test arrangement, the average bond stress, τ , over the $5d_b$ embedment is calculated as:

$$\tau = F/\pi d_b l_b \quad (4.6)$$

Where F is the tensile force applied to the reinforcement, d_b is the bar diameter, and l_b is the bonded length, equal to 80 mm (3.15 in.) in each case. Tables 4.3 and 4.4 summarize the average results of all pull-out tests at ASTM D7913-prescribed values of slip. It is conventional to report bond results in terms of nominal bar sizes. Thus, for a #5 bar, the nominal diameter is $d_b = 15.9$ mm (0.625 in.) and the nominal area is 200 mm² (0.31 in²). As shown in Table 3.3, the measured diameter and area of the titanium bar is greater; therefore, in Table 4.3 the results for the titanium bars (only) are reported for both measured and nominal values.

Table 4.3 (part 1) Summary of pull-out test (titanium)

		Measured $d_b = 16.9 \text{ mm}$ $A_s = 223 \text{ mm}^2$		Measured $d_b = 16.5 \text{ mm}$ $A_s = 215 \text{ mm}^2$		Measured $d_b = 16.5 \text{ mm}$ $A_s = 215 \text{ mm}^2$		Nominal $d_b = 15.8 \text{ mm}$ $A_s = 200 \text{ mm}^2$							
		titanium (heat 1)		titanium (heat 2)		titanium (heat 3)		titanium (heat 1)		titanium (heat 1 – annealed)		titanium (heat 2)		titanium (heat 3)	
		AVG	COV	AVG	COV	AVG	COV	AVG	COV	AVG	COV	AVG	COV	AVG	COV
concrete		batch 1		batch 2		batch 3		batch 1		batch 2		batch 2		batch 3	
number of samples	n	10		5		10		10		5		5		10	
apparent E from clip gage	GPa	104	0.06	97.7	0.09	96.7	0.04	117	0.06	104	0.09	97.7	0.09	114	0.04
load at initiation of slip	kN	12.2	0.25	5.40	0.32	10.1	0.25	12.2	0.25	6.43	0.19	5.40	0.32	10.1	0.25
bar stress at initiation of slip	MPa	54.7	0.25	25.1	0.32	42.7	0.25	61.0	0.25	32.1	0.19	27.0	0.32	50.5	0.25
bar stress at initiation of slip	$1/f_y$	0.05	0.25	0.02	0.32	0.04	0.25	0.06	0.25	0.03	0.19	0.02	0.32	0.05	0.25
average bond stress at initiation of slip	MPa	2.90	0.25	1.31	0.32	2.33	0.25	3.07	0.25	1.62	0.19	1.36	0.32	2.54	0.25
load at 0.05 mm slip	kN	17.7	0.20	12.7	0.37	28.5	0.19	17.7	0.20	12.0	0.24	12.7	0.37	28.5	0.19
bar stress at 0.05 mm slip	MPa	79.1	0.20	58.9	0.37	121	0.19	88.2	0.20	60.1	0.24	63.3	0.37	143	0.19
bar stress at 0.05 mm slip	$1/f_y$	0.07	0.20	0.05	0.37	0.12	0.19	0.08	0.20	0.06	0.24	0.06	0.37	0.14	0.19
average bond stress at 0.05 mm slip	MPa	4.19	0.20	3.06	0.37	6.58	0.19	4.44	0.20	3.02	0.24	3.19	0.37	7.19	0.19
load at 0.10 mm slip	kN	20.4	0.22	16.1	0.37	36.9	0.17	20.4	0.22	15.8	0.24	16.1	0.37	36.9	0.17
bar stress at 0.10 mm slip	MPa	91.3	0.22	74.7	0.37	156	0.17	102	0.22	78.9	0.24	80.3	0.37	184	0.17
bar stress at 0.10 mm slip	$1/f_y$	0.09	0.22	0.07	0.37	0.16	0.17	0.10	0.22	0.08	0.24	0.07	0.37	0.18	0.17
average bond stress at 0.10 mm slip	MPa	4.83	0.22	3.89	0.37	8.50	0.17	5.13	0.22	3.97	0.24	4.04	0.37	9.28	0.17
load at 0.25 mm slip	kN	27.2	0.19	23.7	0.30	50.5	0.14	27.2	0.19	25.1	0.21	23.7	0.30	50.5	0.14
bar stress at 0.25 mm slip	MPa	122	0.19	110	0.30	213	0.14	136	0.19	126	0.21	118	0.30	252	0.14
bar stress at 0.25 mm slip	$1/f_y$	0.12	0.19	0.10	0.30	0.21	0.14	0.13	0.19	0.12	0.21	0.11	0.30	0.25	0.14
average bond stress at 0.25 mm slip	MPa	6.45	0.19	5.72	0.30	11.7	0.14	6.84	0.19	6.33	0.21	5.96	0.30	12.7	0.14
maximum load observed	kN	43.6	0.15	38.6	0.22	65.8	0.13	43.6	0.15	52.1	0.16	38.6	0.22	65.8	0.13
slip at maximum load	mm	1.49	0.12	1.48	0.21	1.17	0.20	1.49	0.12	1.70	0.14	1.48	0.21	1.17	0.20
bar stress at maximum load	MPa	196	0.15	180	0.22	278	0.13	218	0.15	260	0.16	193	0.22	329	0.13
bar stress at maximum load	$1/f_y$	0.19	0.15	0.16	0.22	0.28	0.13	0.21	0.15	0.25	0.16	0.18	0.22	0.33	0.13
average bond stress at maximum load	MPa	10.4	0.15	9.35	0.22	15.2	0.13	11.0	0.15	13.1	0.16	9.73	0.22	16.6	0.13

Table 4.3 (part 2) Summary of pull-out test (A615 Steel and GFRP)

		Nominal $d_b = 15.8 \text{ mm}$ $A_s = 200 \text{ mm}^2$									
		A615 steel		A615 steel		A615 steel		sand coated GFRP		ribbed GFRP	
		AVG	COV	AVG	COV	AVG	COV	AVG	COV	AVG	COV
concrete		batch 1		batch 2		batch 3		batch 1		batch 3	
number of samples	n	5		5		5		5		5	
apparent E from clip gage	GPa	168	0.16	181	0.04	180	0.04	44.4	0.10	40.1	0.02
load at initiation of slip	kN	8.74	0.13	7.17	0.39	11.9	0.73	16.8	0.20	6.41	0.12
bar stress at initiation of slip	MPa	43.7	0.13	35.9	0.39	59.7	0.73	83.8	0.20	32.1	0.12
bar stress at initiation of slip	$1/f_y$	0.09	0.13	0.08	0.39	0.13	0.73	0.11	0.20	0.05	0.12
average bond stress at initiation of slip	MPa	2.20	0.13	1.81	0.39	3.00	0.73	4.22	0.20	1.61	0.12
load at 0.05 mm slip	kN	16.2	0.11	22.1	0.29	19.4	0.43	38.8	0.14	13.2	0.53
bar stress at 0.05 mm slip	MPa	81.0	0.11	110	0.29	97.2	0.43	194	0.14	65.9	0.53
bar stress at 0.05 mm slip	$1/f_y$	0.17	0.11	0.24	0.29	0.21	0.43	0.26	0.14	0.09	0.53
average bond stress at 0.05 mm slip	MPa	4.08	0.11	5.56	0.29	4.89	0.43	9.76	0.14	3.32	0.53
load at 0.10 mm slip	kN	21.0	0.12	29.1	0.22	23.6	0.39	42.2	0.10	25.9	0.15
bar stress at 0.10 mm slip	MPa	105	0.12	146	0.22	118	0.39	211	0.10	130	0.15
bar stress at 0.10 mm slip	$1/f_y$	0.23	0.12	0.31	0.22	0.25	0.39	0.29	0.10	0.19	0.15
average bond stress at 0.10 mm slip	MPa	5.30	0.12	7.33	0.22	5.95	0.39	10.6	0.10	6.53	0.15
load at 0.25 mm slip	kN	29.6	0.07	45.9	0.13	33.0	0.34	45.9	0.07	43.4	0.08
bar stress at 0.25 mm slip	MPa	148	0.07	229	0.13	165	0.34	229	0.07	217	0.08
bar stress at 0.25 mm slip	$1/f_y$	0.32	0.07	0.49	0.13	0.36	0.34	0.31	0.07	0.31	0.08
average bond stress at 0.25 mm slip	MPa	7.46	0.07	11.6	0.13	8.31	0.34	11.6	0.07	10.9	0.08
maximum load observed	kN	45.3	0.10	73.7	0.08	66.4	0.10	47.2	0.06	81.4	0.09
slip at maximum load	mm	1.34	0.24	1.23	0.09	1.52	0.43	0.42	0.18	1.32	0.08
bar stress at maximum load	MPa	227	0.10	368	0.08	332	0.10	236	0.06	407	0.09
bar stress at maximum load	$1/f_y$	0.49	0.10	0.79	0.08	0.71	0.10	0.32	0.06	0.58	0.09
average bond stress at maximum load	MPa	11.4	0.10	18.6	0.08	16.7	0.10	11.9	0.06	20.5	0.09

Figure 4.8 summarizes the average observed bond stress-slip relationships for the ASTM D7913- prescribed values of slip reported in Table 4.3. Figures 4.9 to 4.11 show the entire bond stress-slip relationship for all specimens tested for concrete batches 1 to 3, respectively. Superimposed on part b of these figures are the ASTM D7913-prescribed values of slip.

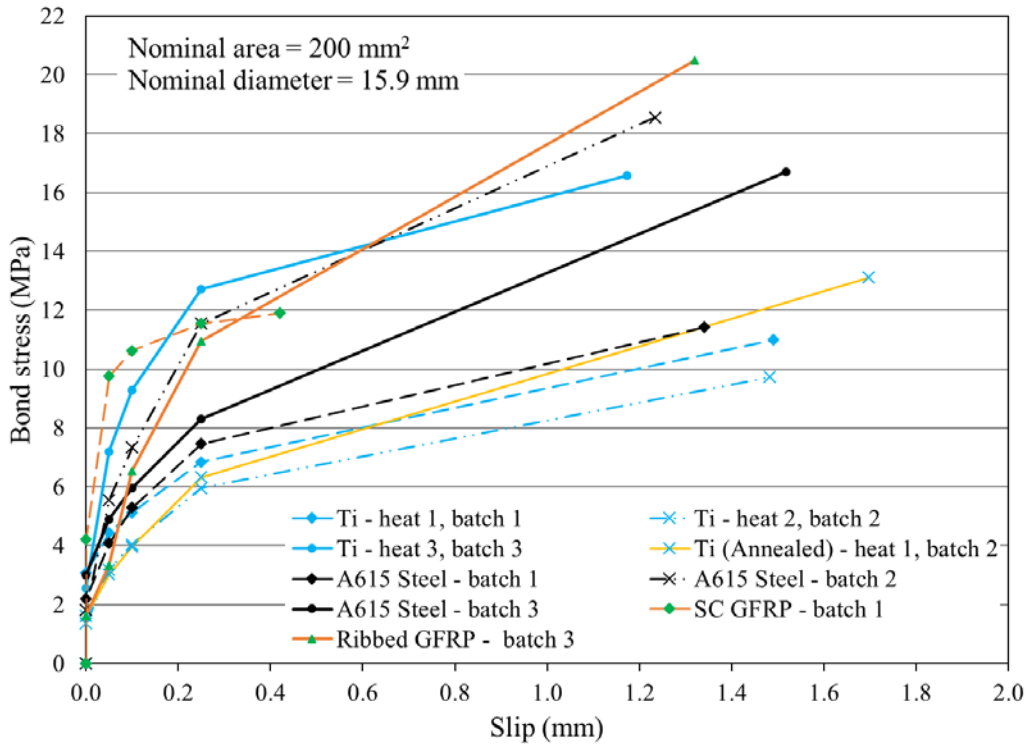
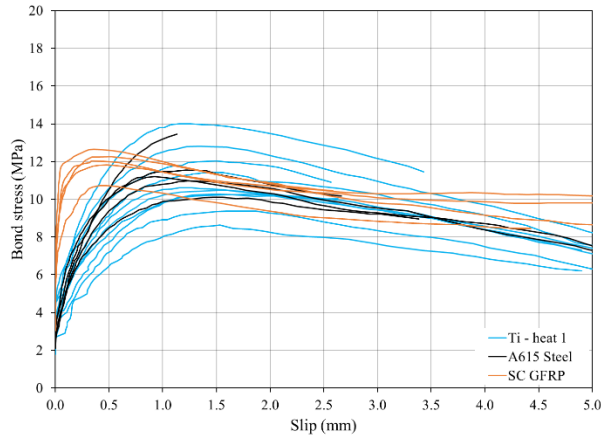
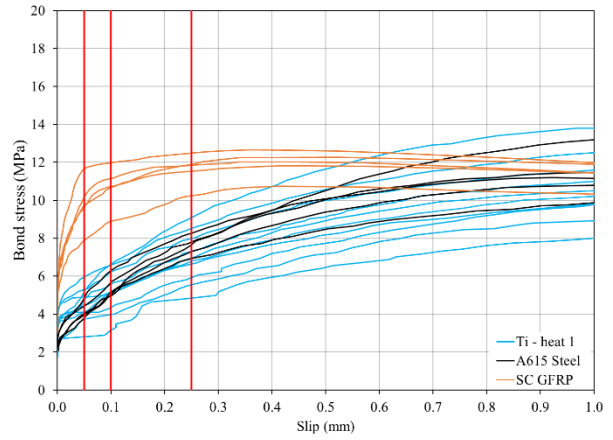


Figure 4.8 Average bond stress-slip relationships

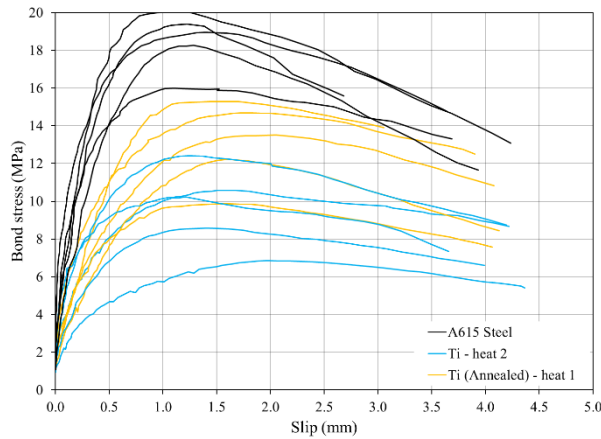


a) complete experimentally-determined bond stress-slip curves

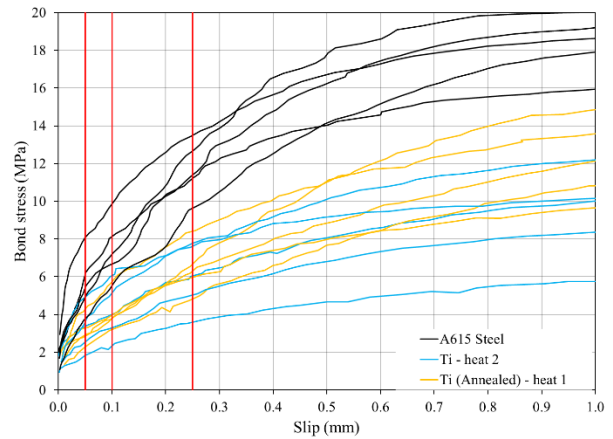


b) experimentally-determined bond stress-slip curves up to 1.0 mm slip

Figure 4.9 Bond stress-slip relationships for specimens tested with batch 1 concrete

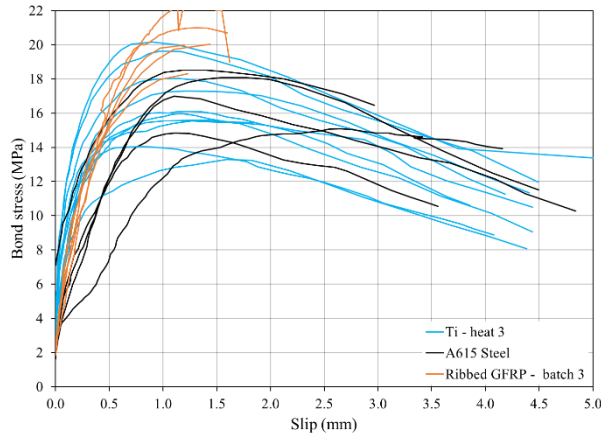


a) complete experimentally-determined bond stress-slip curves

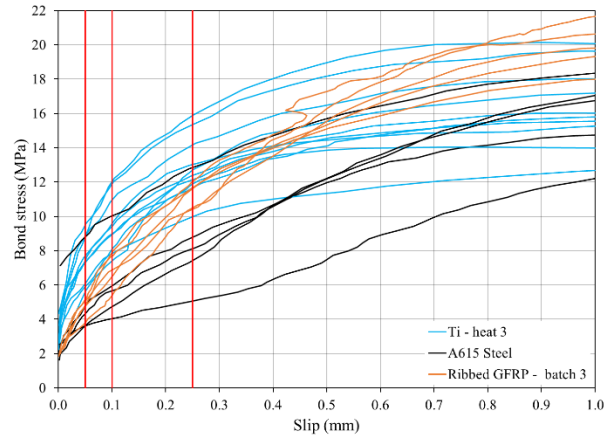


b) experimentally-determined bond stress-slip curves up to 1.0 mm slip

Figure 4.10 Bond stress-slip relationships for specimens tested with batch 2 concrete



a) complete experimentally-determined bond stress-slip curves



b) experimentally-determined bond stress-slip curves up to 1.0 mm slip

Figure 4.11 Bond stress-slip relationships for specimens tested with batch 3 concrete

Figure 4.12 compares the resulting bond stress calculated using nominal and measured bar dimensions. Since the titanium bars are larger than the nominal dimensions, the actual bond stress developed is lower in proportion to the bar diameter. The stress in the bar at the same applied force, however is lower in proportion to the diameter squared as seen in Table 4.3.

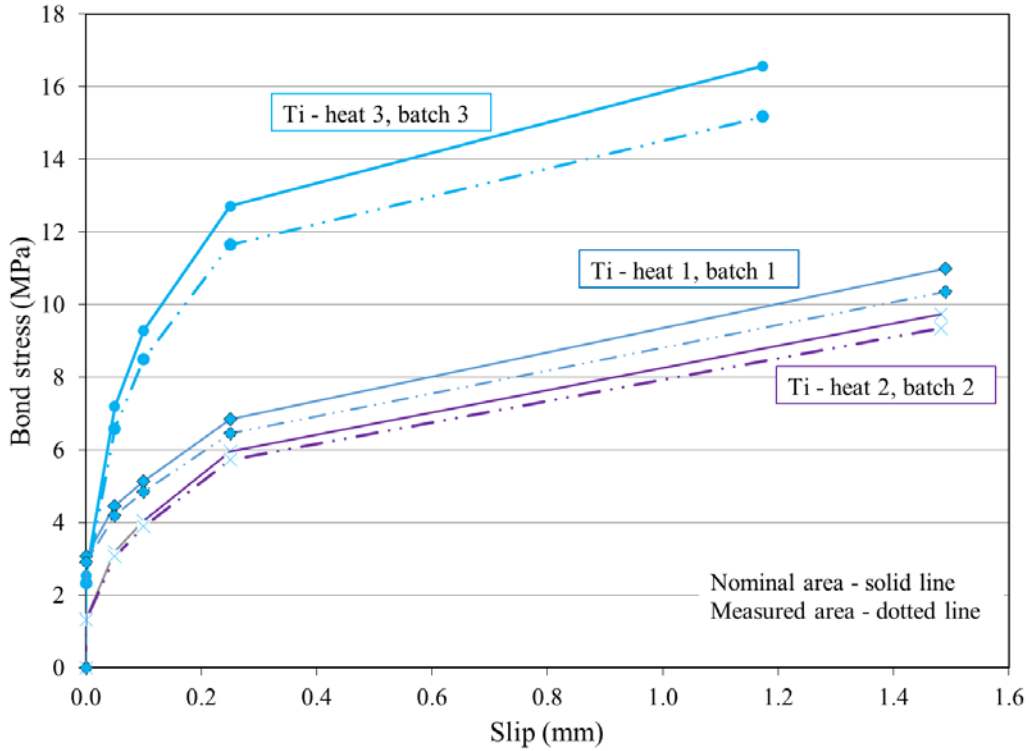


Figure 4.12 Bond stress-slip relationships for nominal and measured bar geometries

Bond stress is proportional to an exponential of concrete strength, $(f_c')^n$, where $n = 0.5$ in ACI 318 practice [ACI 318-14 §25.4.2] and $n = 0.66$ in EC2 practice [EC2 §8.4]. In order to normalize the obtained data for concrete strength, bond stress is divided by $(f_c')^{0.66}$ and plotted against slip in Figure 4.13. The basis for selecting $n = 0.66$ is that it results in a better correlation for the steel pull-out tests. Since no other parameter apart from concrete strength was varied in the steel tests, it is expected that the normalized bond stress-slip relationships found for steel should be the same.

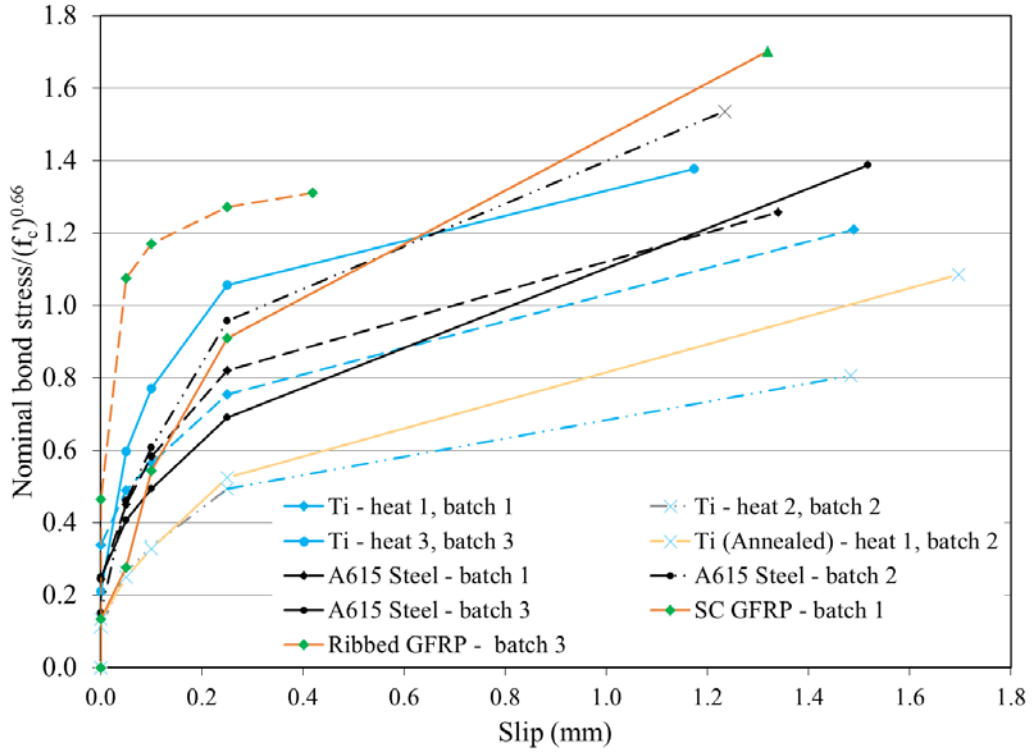


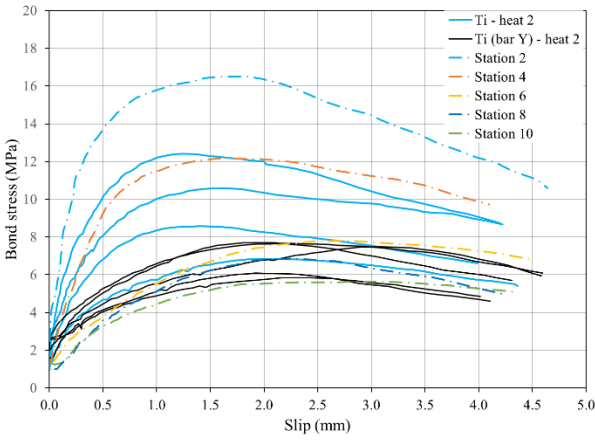
Figure 4.13 Normalized bond stress-slip relationships

4.3.4 Bar X and Bar Y Results

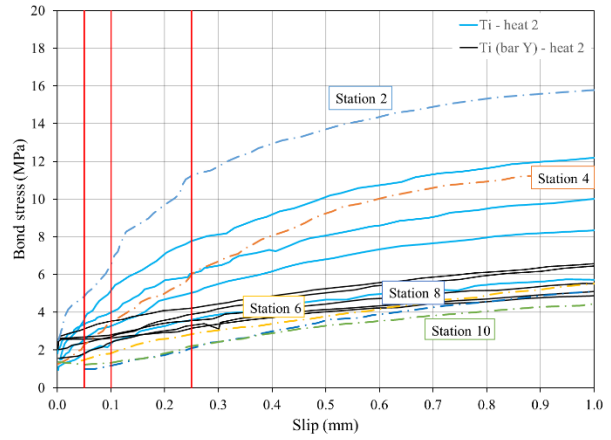
Table 4.4 presents the results obtained from ASTM D7913-14 tests of samples obtained from bar X (having varying deformations) and Bar Y (having very poor deformation). Figure 4.14 shows the resulting bond stress slip relationships obtained and Figure 4.15 shows a summary of these.

Table 4.4 Summary of pull-out test for Bars X and Y (Ti Heat 2; concrete Batch 2)

Station		Bar X					Bar Y	
		2	4	6	8	10	AVG	COV
rib ratio, R_r (Table 3.4)		0.115	0.113	0.020	0.017	0.020	0.016	
apparent E from clip gage	GPa	109	110	90.7	-	95.2	102	0.08
load at initiation of slip	kN	9.97	4.94	5.69	3.89	5.40	8.56	0.20
nominal bar stress at initiation of slip	MPa	50	25	28	19	27	42.8	0.20
nominal bar stress at initiation of slip	$1/f_y$	0.07	0.02	0.03	0.02	0.04	0.04	0.20
average bond stress at initiation of slip	MPa	2.51	1.24	1.43	0.98	1.36	2.16	0.20
load at 0.05 mm slip	kN	19.2	8.03	5.69	3.89	4.89	9.59	0.22
nominal bar stress at 0.05 mm slip	MPa	96	40	28	19	24	48.0	0.22
nominal bar stress at 0.05 mm slip	$1/f_y$	0.13	0.04	0.03	0.02	0.03	0.04	0.22
average bond stress at 0.05 mm slip	MPa	4.83	2.02	1.43	0.98	1.23	2.42	0.22
load at 0.10 mm slip	kN	25.9	13.1	7.18	4.64	5.21	11.0	0.16
nominal bar stress at 0.10 mm slip	MPa	129	65	36	23	26	55.2	0.16
nominal bar stress at 0.10 mm slip	$1/f_y$	0.17	0.06	0.03	0.02	0.04	0.05	0.16
average bond stress at 0.10 mm slip	MPa	6.51	3.29	1.81	1.17	1.31	2.78	0.16
load at 0.25 mm slip	kN	43.9	22.9	11.2	8.22	8.74	14.0	0.13
nominal bar stress at 0.25 mm slip	MPa	220	115	56	41	44	70.0	0.13
nominal bar stress at 0.25 mm slip	$1/f_y$	0.30	0.11	0.05	0.04	0.06	0.06	0.13
average bond stress at 0.25 mm slip	MPa	11.1	5.78	2.83	2.07	2.20	3.53	0.13
maximum load observed	kN	65.6	48.4	31.0	27.2	22.4	27.6	0.13
slip at maximum load	mm	1.77	1.65	2.66	2.26	2.94	2.33	0.19
nominal bar stress at maximum load	MPa	328	242	155	136	112	138	0.13
nominal bar stress at maximum load	$1/f_y$	0.44	0.23	0.15	0.13	0.15	0.13	0.13
average bond stress at maximum load	MPa	16.5	12.2	7.80	6.86	5.63	6.95	0.13

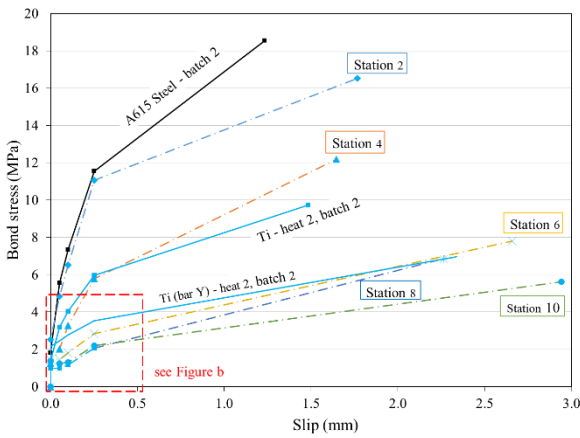


a) complete bond stress-slip relationships

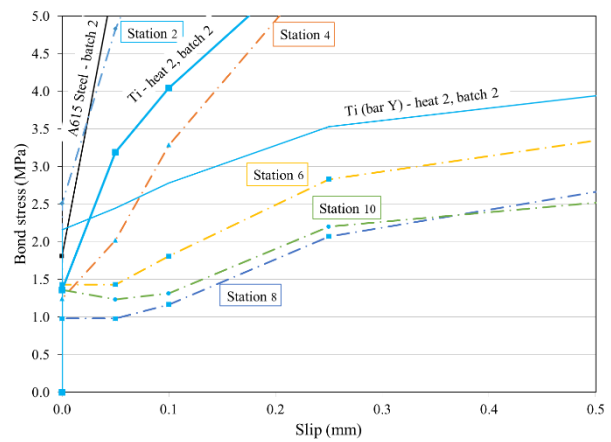


b) bond stress-slip curves up to 1.0 mm slip

Figure 4.14 Bond stress-slip relationships for five specimens from Bar X



a) complete bond stress-slip relationships



b) bond stress-slip curves up to 0.5 mm slip

Figure 4.15 Summary of bond stress-slip relationships for five specimens from Bar X

4.3.5 Discussion and Summary of Pull-out Test Results

The nature of reinforcing bar bond to concrete is such that deformed bars will exhibit very similar patterns of bond stress-slip behavior. This is evident in this study. Provided adequate deformations are provided, the bond-slip relationship is dominated by concrete behavior. The bond performance of the titanium bars was similar to that of the steel bars and, as expected,

clearly affected by the rib ratio. The results presented reinforce the ASTM A615-implied lower limit for the rib ratio, $R_r > 0.05$.

The implication of a similar bond-stress behavior is that existing bond relationships for steel-reinforced concrete likely apply to titanium bars provided the bars meet the deformation requirements of ASTM A615 – the standard for which steel reinforcing bars, and therefore their bond characterization – is calibrated.

The ribbed GFRP behaved similarly to the deformed metal bars although was considerably more brittle, reflecting post-peak shear failure of the deformations from the bar itself. Only the sand-coated GFRP exhibited a markedly stiffer bond-slip response however, these bars typically exhibit a lower bond capacity due to the reduced mechanical engagement of the concrete.

4.4 BEAM END TESTING

A more representative method for assessing bond is the beam-end test described in ASTM A944-10 which has been used in many studies including numerous modified versions of the test. Like the pull-out test, the beam-end test is primarily an A-B comparison test, although the mechanics of the test result in a stress state, similar to that which occurs at the end of a simply supported beam. The longer embedment length of the beam-end test also permits a better understanding of the development of the bar being tested. Indeed, the beam-end test can be designed to demonstrate full development, with the resulting failure mode being yield of the reinforcing bar.

The test matrix for the beam-end tests performed is summarized in Table 4.5. Three specimens of each material were considered and a ‘control’ series of the same ASTM A615 bars were tested with each concrete batch to permit normalization of results.

Table 4.5 Beam-end test matrix indicating number of samples tested

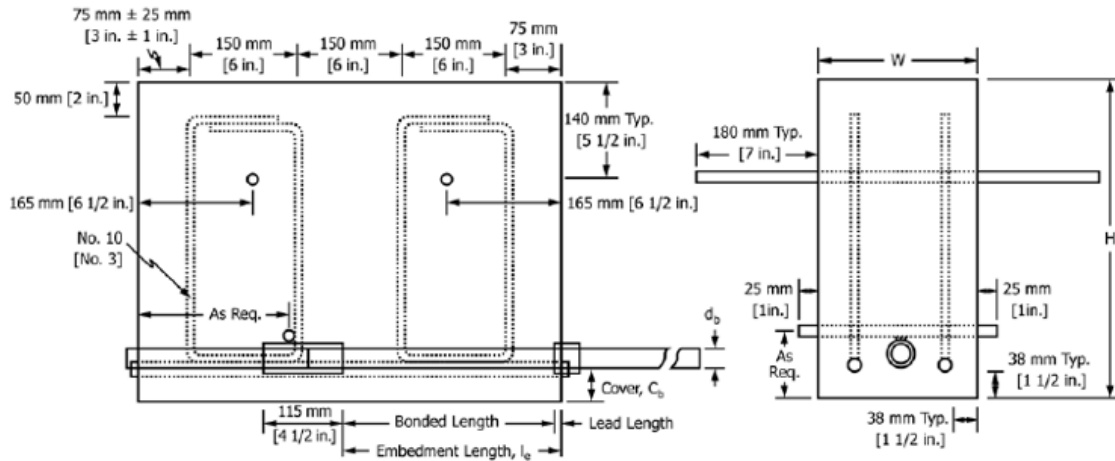
#5 bars	heat	R_r	concrete batch	bonded length		
				$l_b = 0.5l_d$	$l_b = 1.0l_d$	$l_b = 1.5l_d$
ASTM A615	-	0.079	2	1	3	3
			3	-	3	-
titanium	2	0.033	2	-	3	3
titanium	3	0.123	3	-	3	3
sand-coated GFRP	-	-	2	-	3	-
ribbed GFRP	-	0.082	3	-	3	-

4.4.1 Test Specimens

The same concrete mix designs and curing conditions, described in Section 4.1, are used for all concrete in this test program. The beam-end test specimens are compliant with those described in ASTM A944-10 and shown in Figure 4.16a. All specimens have the same dimensional details, only the bonded length (l_b), the length of reinforcement in direct contact with the concrete, of the embedded reinforcing bar is varied. The bonded lengths (l_b) were selected as multiples of the basic tensile development length (l_d) of a #5 ASTM A615 bar having $f_y = 414$ MPa and $f_c' = 28$ MPa, determined from Eq 4.2; $l_b = 21.3d_b = 340$ mm.

As indicated in Table 4.5, #5 reinforcing bars of titanium, A615 steel, and GFRP were cast into 216 x 603 x 622 mm concrete forms (Figure 4.16). Bars have bonded regions of $0.5l_d$, $1.0l_d$, or $1.5l_d$. The remaining embedded length is divided into two unbonded regions by placing

the bar at these locations within 19.2 mm I.D. (24.3 mm O.D.) GFRP tubes (seen in Figure 4.16b).



a) ASTM A944 test specimen [ASTM A944-10]



b) single form



c) series of forms



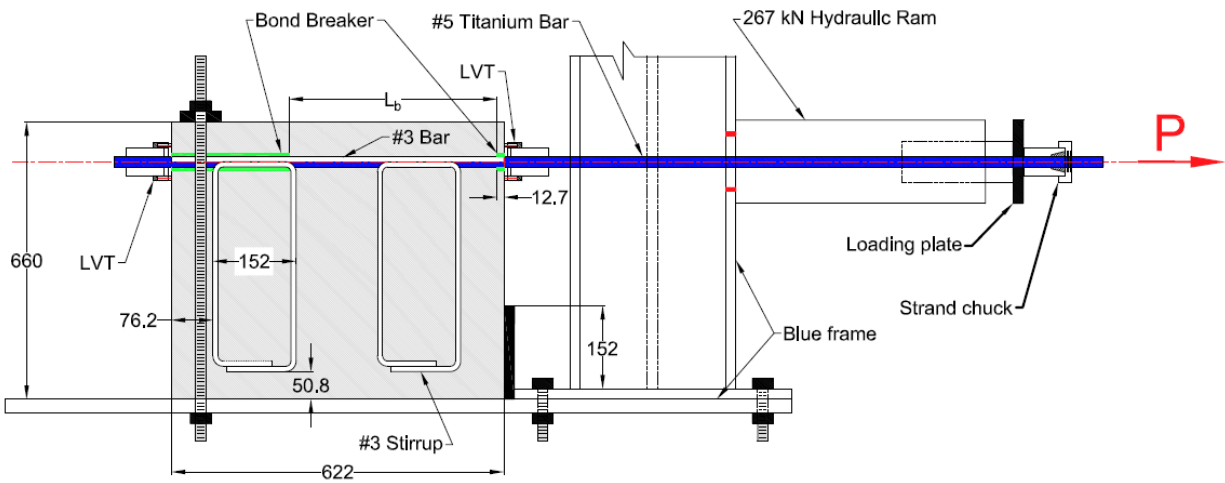
d) placing concrete

Figure 4.16 ASTM A944-10 test specimen details and fabrication

4.4.2 Test Set-up and Protocol

All beam-end tests are compliant with ASTM A944-10. The testing frame was designed around a large self-contained reaction frame. Load was applied concentrically to the bar using a 267 kN (60 kip) hollow core hydraulic ram (Figure 4.17). The hydraulic pressure is used to calculate the applied load with a precision of 320 N (72 lb). Slip is measured by implementing the same

LVDT collar used in the cube pull-out tests (Figure 4.7b) having a precision of 0.004 mm (0.0002 in.) which exceeds the 0.025 mm (0.001 in.) precision required by ASTM A944-10. Load was applied in 2.22 kN (500 lb) increments and instrument readings were taken from LVDTs at the loaded and free ends of the reinforcing bar at each load step.



a) schematic fixture for beam end test (after ASTM A944; units shown in mm)



b) photo of apparatus



c) free end elevation



d) loaded end (top view)

Figure 4.17 ASTM A944-10 test set-up

4.4.3 Test Results

Using the ASTM A944-10 test arrangement, the average bond stress, τ , was calculated using equation 4.6 as previously discussed for the pull-out tests. Table 4.6 summarizes the results. Typically, beam-end tests exhibit very little bar end slip before failure. In this study, the initial measurable slip (0.004 mm) and a second value (0.009 mm) are reported in addition to the measured slip at the ultimate capacity. In some cases, a brittle failure mode resulted in the ultimate slip not being recorded. Figures 4.18a and b show the calculated bond stress and bar stress versus free end bar slip relationships, respectively.

The single A615 specimen having $l_b = 0.5l_d$ was intended to demonstrate a bond pull-out failure in which the embedment is inadequate to develop the full capacity of the bar. In this case, with $l_b = 0.5l_d$, the bar was only able to develop $0.77f_y$ prior to pulling out from the beam end specimen. In contrast, the A615 specimens having $l_b = l_d$, all were able to develop more than $1.2f_y$. When embedment length was increased to $l_b = 1.5l_d$, the bar was able to approach its ultimate capacity, exceeding $1.4f_y$ prior to failing. The results with A615 steel validate the concept of development length and the efficacy of the ASTM A944-10 test method as a basis of comparison.

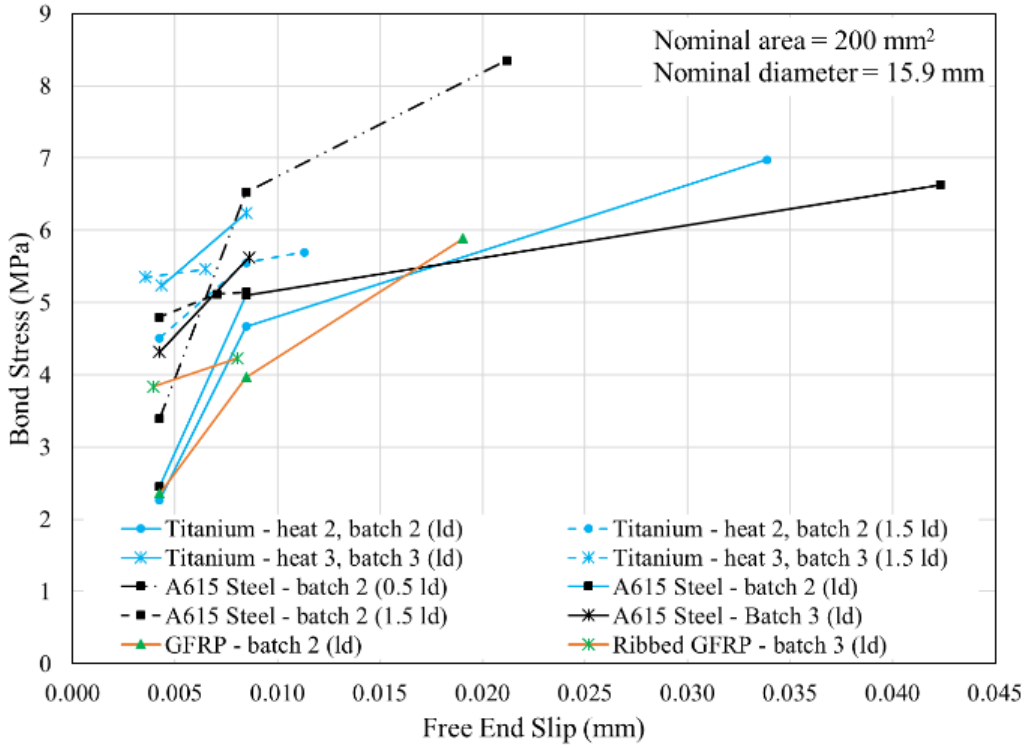
The capacity of the titanium bar beam-end tests appears to validate the use of Eq. 4.2 for the Heat 3 titanium bars tested. The bar stress (or bond stress) developed in the titanium is essentially the same as that for the steel at comparable load levels (Table 4.6). As expected, the GFRP bars tested exhibit lower bond stress values and the sand-coated bar exhibits better behavior than the ribbed bar.

Table 4.6 (part 1) Summary of beam-end test ($l_b = 0.5l_d$ and $l_b = 1.0l_d$)

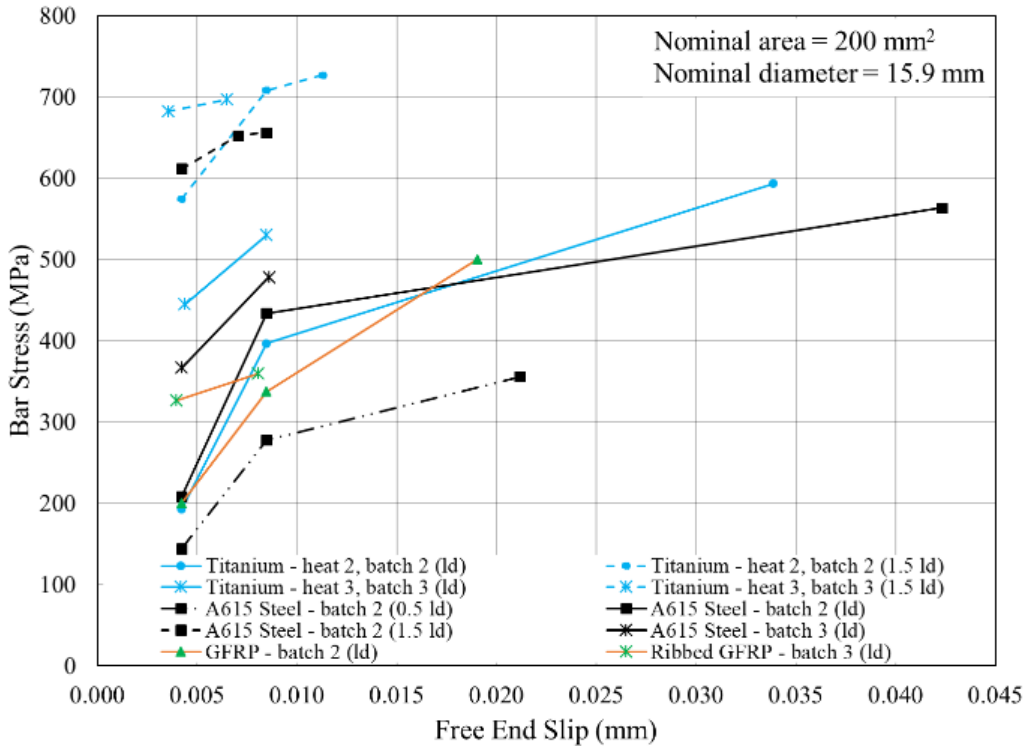
		$l_b = 0.5l_d$ = 171 mm		$l_b = 1.0l_d = 340$ mm										
		A615 steel		A615 steel		titanium (heat 2)		titanium (heat 3)		sand coated GFRP		ribbed GFRP		
		-	AVG	COV	AVG	COV	AVG	COV	AVG	COV	AVG	COV	AVG	COV
concrete		batch 2	batch 2		batch 3		batch 2		batch 3		batch 2		batch 3	
number of samples	n	1	3		3		3		3		3		3	
load at 0.05 mm slip	kN	28.9	41.7	0.30	73.4	0.18	38.5	0.43	89.0	0.13	40.0	0.73	65.2	0.07
nominal bar stress at 0.004 mm slip	MPa	145	209	0.30	367	0.18	193	0.43	445	0.13	200	0.73	326	0.07
nominal bar stress at 0.004 mm slip	$1/f_y$	0.31	0.45	0.30	0.79	0.18	0.18	0.43	0.45	0.13	0.27	0.73	0.47	0.07
average bond stress at 0.004 mm slip	MPa	3.39	2.46	0.30	4.32	0.18	2.27	0.43	5.23	0.13	2.35	0.73	3.84	0.07
load at 0.009 mm slip	kN	55.6	86.7	0.08	95.6	0.16	79.3	0.21	106	0.05	67.5	0.43	71.9	0.05
nominal bar stress at 0.009 mm slip	MPa	278	434	0.08	478	0.16	397	0.21	530	0.05	337	0.43	360	0.05
nominal bar stress at 0.009 mm slip	$1/f_y$	0.60	0.93	0.08	1.03	0.16	0.36	0.21	0.53	0.05	0.46	0.43	0.52	0.05
average bond stress at 0.009 mm slip	MPa	6.53	5.10	0.08	5.63	0.16	4.67	0.21	6.24	0.05	3.97	0.43	4.23	0.05
maximum load observed	kN	71.2	113	0.02	119	0.01	119	0.07	114	0.01	100	0.02	79.3	0.04
slip at maximum load	mm	0.02	0.04	1.04	-	-	0.03	0.71	-	-	0.02	0.16	-	-
nominal bar stress at maximum load	MPa	356	563	0.02	593	0.01	593	0.07	571	0.01	500	0.02	397	0.04
nominal bar stress at maximum load	$1/f_y$	0.77	1.21	0.02	1.28	0.01	0.54	0.07	0.57	0.01	0.68	0.02	0.57	0.04
average bond stress at maximum load	MPa	8.35	6.63	0.02	6.98	0.01	6.98	0.07	6.72	0.01	5.89	0.02	4.66	0.04

Table 4.6 (part 2) Summary of beam-end test ($l_b = 1.5l_d$)

		$l_b = 1.5l_d = 511 \text{ mm}$					
		A615 steel		titanium (heat 2)		titanium (heat 3)	
		AVG	COV	AVG	COV	AVG	COV
concrete		batch 2		batch 2		batch 3	
number of samples	n	3		3		3	
load at 0.05 mm slip	kN	122	0.03	115	0.35	136	0.06
nominal bar stress at 0.004 mm slip	MPa	612	0.03	575	0.35	682	0.06
nominal bar stress at 0.004 mm slip	$1/f_y$	1.32	0.03	0.53	0.35	0.68	0.06
average bond stress at 0.004 mm slip	MPa	4.80	0.03	4.51	0.35	5.35	0.06
load at 0.009 mm slip	kN	133	-	142	0.02	139	0.05
nominal bar stress at 0.009 mm slip	MPa	667	-	708	0.02	697	0.05
nominal bar stress at 0.009 mm slip	$1/f_y$	1.44	-	0.65	0.02	0.70	0.05
average bond stress at 0.009 mm slip	MPa	5.23	-	5.55	0.02	5.47	0.05
maximum load observed	kN	131	0.04	145	0.02	145	0.04
slip at maximum load	mm	0.01	0.50	0.01	0.43	-	-
nominal bar stress at maximum load	MPa	656	0.02	727	0.02	727	0.04
nominal bar stress at maximum load	$1/f_y$	1.41	0.02	0.67	0.02	0.73	0.04
average bond stress at maximum load	MPa	5.15	0.02	5.70	0.02	5.70	0.04



a) average bond stress –free end slip



b) bar stress –free end slip
Figure 4.18 Beam-end test results

Figure 4.19 provides an example of the effect of the radial stresses (see Section 4.1 and Figure 4.4) at the vertical face of the loaded end of select beam-end specimens from batch 2 with development lengths of 340 mm. The more significant radial cracking associated with the greater rib ratio of the A615 steel is evident. Figure 4.20 shows the crack patterns and reports their development for all beam end tests.

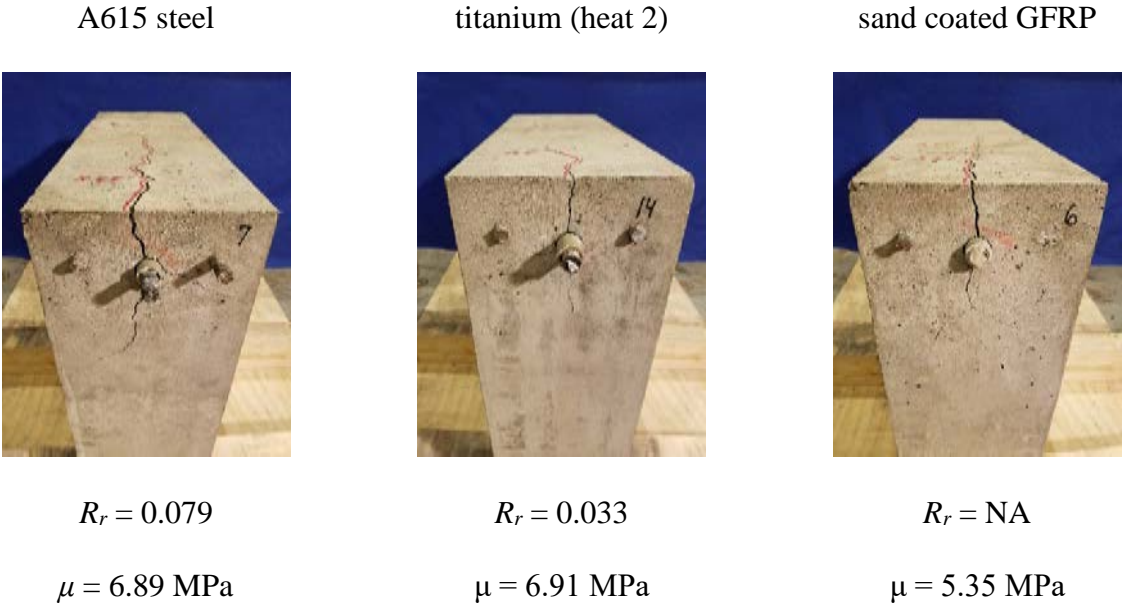


Figure 4.19 Radial cracking at loaded face

Stresses are calculated using as measured area of the reinforcing bars. The reported stresses in this table are given at the point of first observable crack. That is the first sign of [splitting] cracking that was detectable visually on the top plane of the beam end. Due to the testing set up, cracks on the loaded end vertical surface (Figure 4.17) could not be observed until after removal from the testing frame. In this instance, slip is taken as the first measurable movement of the bar at the free end (0.004 mm) whereas the bond strength has been taken as the

second measurable movement (0.009 mm). For the bond calculation, this makes sense as the second slip measurement in most cases was substantially higher than the first and in some cases was the maximum slip observed. As the cracking progression is of interest here, the first slip relative to the first crack is of importance. The following observations based on Figure 4.20 are made:

- 1) patterns are essentially similar – crack extension to the end of the development provided and a ‘fish bone’ crack at this location
- 2) first cracking (and to some extent the first perpendicular crack location) are functions of stiffness of bond. Steel and Ti are indistinguishable and sand coated GFRP is stiffer resulting in earlier crack.
- 3) cracking and slippage was observed to relate to both the stiffness of the reinforcing bar as well as the relative rib ratios as seen by comparing batches 2 and 3 which incorporated two rib ratios for titanium and two surface treatments for GFRP as reported previously in Table 3.4.

0.5l _d = 171 mm	ASTM A615 steel (batch 2)		no cracking observed bar slip: 144 MPa (0.31f _y)
	ASTM A615 steel (batch 2)		
l _d = 340 mm			
	first crack: 316 MPa (0.68f _y)	510 MPa (1.10f _y)	374 MPa (0.81f _y)
	first bar slip: 277 MPa (0.60f _y)	188 MPa (0.41f _y)	158 MPa (0.34f _y)
	ASTM A615 steel (batch 3)		
	first crack: 378 MPa (0.81f _y)	422 MPa (0.91f _y)	378 MPa (0.81f _y)
	first bar slip: 288 MPa (0.62f _y)	398 MPa (0.86f _y)	409 MPa (0.88f _y)
	titanium heat 2 (batch 2)		
	first crack: 403 MPa (0.37f _y)	no cracking observed	345 MPa (0.32f _y)
	first bar slip: 269 MPa (0.25f _y)	134 MPa (0.29f _y)	134 MPa (0.12f _y)
	titanium heat 3 (batch 3)		
	first crack: 376 MPa (0.38f _y)	394 MPa (0.39f _y)	357 MPa (0.36f _y)
	first bar slip: 395 MPa (0.40f _y)	320 MPa (0.32f _y)	414 MPa (0.41f _y)
	sand coated GFRP (batch 2)		
	first crack: 194 MPa (0.26f _{tu})	258 MPa (0.35f _{tu})	194 MPa (0.26f _{tu})
first bar slip: 77.1 MPa (0.11f _{tu})	318 MPa (0.44f _{tu})	125 MPa (0.17f _{tu})	
ribbed GFRP (batch 3)			
first crack: 207 MPa (0.30f _{tu})	no cracking observed	207 MPa (0.30f _{tu})	
first bar slip: 279 MPa (0.40f _{tu})	310 MPa (0.45f _{tu})	321 MPa (0.46f _{tu})	

Figure 4.20 (part 1) Beam-end crack patterns and progression (pull out to right in all images)

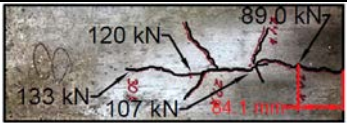
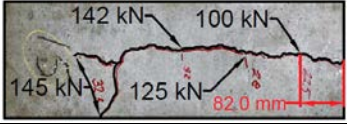
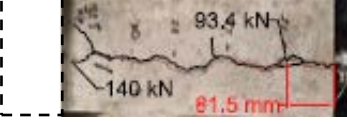
$1.5l_d = 511 \text{ mm}$	ASTM A615 steel (batch 2)		
			
	first crack: 294 MPa ($0.63f_y$)	287 MPa ($0.62f_y$)	308 MPa ($0.66f_y$)
	first bar slip: 620 MPa ($1.34f_y$)	586 MPa ($1.26f_y$)	620 MPa ($1.34f_y$)
	titanium heat 2 (batch 2)		
			
	first crack: 439 MPa ($0.40f_y$)	423 MPa ($0.39f_y$)	323 MPa ($0.30f_y$)
	first bar slip: 651 MPa ($0.60f_y$)	321 MPa ($0.29f_y$)	631 MPa ($0.58f_y$)
	titanium heat 3 (batch 3)		
			
	first crack: 376 MPa ($0.38f_y$)	413 MPa ($0.41f_y$)	394 MPa ($0.39f_y$)
	first bar slip: 592 MPa ($0.59f_y$)	602 MPa ($0.60f_y$)	536 MPa ($0.54f_y$)

Figure 4.20 (part 2) Beam-end crack patterns and progression (pull out to right in all images)

4.4.4 Discussion and Summary of Beam-End Test

Both, the pull-out and beam-end tests are A-B tests that are best used to evaluate relative performance of reinforcing bars. Table 4.7 summarizes the observed average bond stresses corresponding to a bar slip of 0.009 mm (0.0004 in.) for all cases studied: embedment of $0.23l_d$ (pull-out test), $0.5l_d$, l_d , and $1.5l_d$ (l_d is calculated by Eq. 4.2 for the #5 ASTM A615 bars). Similarly, Table 4.8 summarizes the maximum bond stress and corresponding development length calculated using Eq. 2 in each test. The data in both Tables 4.7 and 4.8 reinforce the conclusion that bond behavior of titanium bars is essentially the same as that steel bars. The bond stresses, normalized to account for variation in concrete strength, are similar (Table 4.7). The calculated development lengths are essentially in the ratio of yield strengths of the materials (Table 4.8)

Table 4.7 Summary of avg. bond stress¹ determined at slip of 0.009 mm

# 5 bars	heat	batch	ASTM D7913		ASTM A944					
			80 mm = 0.23l _d		170 mm = 0.5l _d		340 mm = l _d		511 mm = 1.5l _d	
			τ (MPa)	τ/(f _c ') ^{0.66}	τ (MPa)	τ/(f _c ') ^{0.66}	τ (MPa)	τ/(f _c ') ^{0.66}	τ (MPa)	τ/(f _c ') ^{0.66}
A615 steel	-	1	3.00 (0.11)	0.34	-	-	-	-	-	-
	-	2	2.77 (0.34)	0.23	6.53	0.54	5.10 (0.08)	0.42	5.23 (0.02)	0.43
	-	3	2.71 (0.10)	0.23	-	-	5.63 (0.16)	0.47	-	-
Ti	1	1	3.85 (0.19)	0.44	-	-	-	-	-	-
	2	2	1.94 (0.28)	0.16	-	-	4.67 (0.21)	0.39	5.55 (0.02)	0.46
	3	3	4.40 (0.16)	0.37	-	-	6.24 (0.05)	0.52	5.47 (0.05)	0.45
sand coated GFRP	-	1	7.02 (0.11)	0.81	-	-	-	-	-	-
	-	2	-	-	-	-	3.97 (0.42)	0.33	-	-
ribbed GFRP	-	3	2.54 (0.10)	0.21	-	-	4.23 (0.05)	0.35	-	-

¹COV in brackets

Table 4.8 Summary of maximum avg. bond stress¹ and corresponding development length from Equation 2

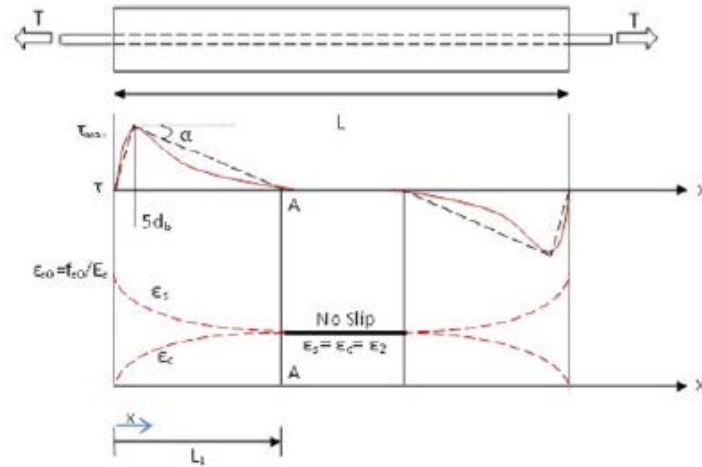
# 5 bars	heat	batch	ASTM D7913		ASTM A944					
			80 mm = 0.23l _d		170 mm = 0.5l _d		340 mm = l _d		511 mm = 1.5l _d	
			τ (MPa)	l _d (mm)	τ (MPa)	l _d (mm)	τ (MPa)	l _d (mm)	τ (MPa)	l _d (mm)
A615 steel	-	1	11.4 (0.10)	163	-	-	-	-	-	-
	-	2	18.6 (0.08)	100	8.35	222	6.63 (0.02)	280	5.15 (0.04)	361
	-	3	16.3 (0.10)	114	-	-	6.98 (0.01)	266	-	-
Ti	1	1	11.0 (0.15)	384	-	-	-	-	-	-
	2	2	9.73 (0.22)	422	-	-	6.98 (0.07)	589	5.70 (0.02)	721
	3	3	16.6 (0.13)	241	-	-	6.72 (0.01)	595	5.70 (0.04)	701
sand coated GFRP	-	1	11.9 (0.06)	249	-	-	-	-	-	-
	-	2	-	-	-	-	5.89 (0.02)	503	-	-
ribbed GFRP	-	3	20.5 (0.09)	136	-	-	4.66 (0.04)	597	-	-

¹COV in brackets

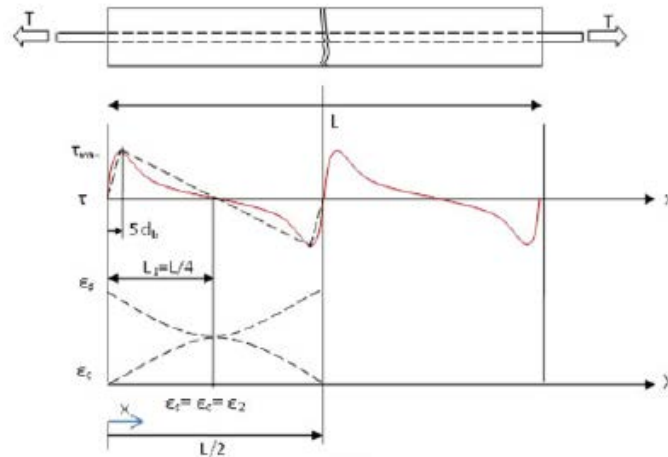
4.5 PRISM TENSION TESTING

When a reinforcement bar is loaded in tension, the adhesive component of the bond is the initial transfer mechanism followed by frictional slip; both quickly dissipate, replaced by the mechanical component of bond (Figure 4.1a). Within the development length, the deformations will begin to bear onto the concrete with resulting forces inclined with respect to the bar axis (Figure 4.1b). The perpendicular component of this normal force produces a radially-oriented tension force in the surrounding concrete causing longitudinal splitting. The angled resultant force, however, engages the concrete surrounding the bar and will affect the rate at which force is transferred. This, in turn, affects the transverse crack spacing and therefore crack widths.

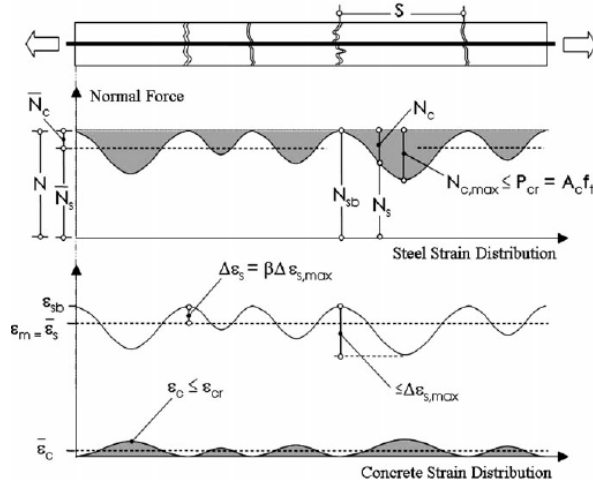
Bond stress can be idealized by axially loading a single bar-reinforced concrete prism in tension as shown in Figure 4.21. Theoretically, once beyond the transfer length, L_t , the stresses and strains along the length of the prism are uniform (Figure 4.21a). As the bar is loaded, tensile stress will increase in the concrete. Once the tension capacity of the concrete is exceeded, a primary crack forms (Figure 4.21b). At the crack locations, the bar resists 100% of the applied load; that is: $f_s = T/A_b$ and the distribution of stress and strains are longer uniform. Between cracks, a portion of the load is transferred to the concrete through bond (Figure 4.21b). If the distance between cracks is sufficient to permit tensile strains to develop, the concrete will crack again between existing cracks (so-called secondary cracks). This process continues until the crack spacing, s , is too short to permit development of the concrete tensile strength between cracks (Figure 4.21c). At this stage, no further cracking develops and increased applied load results in only increased crack widths.



a) bond stress and resulting steel and concrete strain distribution before cracking [Soltani et al. 2013]



b) first crack appears when concrete reaches critical tensile capacity [Soltani et al. 2013]



c) load distribution of concrete and steel bar in cracked RC under tension [Sahamitmongkol and Kishi 2011]

Figure 4.21 Crack development and internal strains in direct tension test

Between cracks, the concrete stress is less than the tensile capacity of the concrete and the concrete and reinforcing are composite, resulting in lower reinforcing bar strains than at the cracks. This is known as “tension stiffening” [Collins & Mitchell 1997]. The bond stress is therefore proportional to the slope of the longitudinal reinforcing bar stress distribution. Since the stress in the reinforcing bar is equal at each crack, the average bond stress between cracks, τ_{avg} , is also equal. This results in a theoretical final crack spacing that is a function of bond capacity. The greater the bond capacity, the more rapidly stress may be transferred to the concrete resulting in closer cracks (reduced spacing). Since the total strain remains the same, these closely spaced cracks have smaller crack widths. This is the goal of durable concrete *having a large number of (closely spaced) small cracks*, rather than few larger cracks.

4.5.1 Test Specimens and Test Method

Six 127 mm square x 1575 mm long (5 in. square by 62 in. long) specimens, each with a single #5 reinforcing bar cast through its center with sufficient exposed length on either end to permit gripping in the testing frame were cast. The basic geometry is shown schematically in Figure 4.21. As the prism is loaded in tension, the formation of cracks are recorded including their locations, initiation loads, and a crack scope is used to accurately measure the width of the crack at predetermined load levels. Two of each bar type, ASTM A615, titanium (batch 1) and sand-coated GFRP, were tested. Material properties of the bars are given in Table 3.1. The prisms were cast from concrete from batch 1 (Table 4.1). Direct tension tests were conducted in a 600 kN (135 kip) capacity servo-hydraulic load frame. Load was applied monotonically to develop a

cracking history. Following this, the cracked specimens were loaded to 76, 125 and 173 kN and crack widths recorded. For such a test to provide meaningful data, the bars must remain elastic.

4.5.2 Prism Test Results

A summary of the crack development with monotonically increasing axial load, the crack widths and crack spacing are provided in Table 4.9. Bar stresses are given based on nominal area; thus, these are the stresses at the prism ends and at each crack. A photo of all six specimens following testing is shown in Figure 4.22. The following observations are made which reinforce previous discussions and observations:

- 1) Cracking itself (initiation and development of subsequent cracks) is a function of the concrete. The embedded bar, provided it is bonded to the concrete serves to *control* cracking not affects its initiation.
- 2) Since the bars alone carry stress across the cracks, crack width is inversely proportional to bar stiffness, AE .

Crack spacing is a function of bond behavior – that is, how efficiently does the bar transfer stress to the concrete at either end and to either side of a crack. The crack spacing for the steel bars is considered the control. In this study, the spacing was observed to be between 200 and 220 mm. The Heat 1 titanium bars exhibited a ‘softer’ bond-slip relationship (see Figures 4.4 and 4.8) than the steel; thus, the crack spacing is greater (about 320 mm). Similarly, the sand-coated GFRP exhibited a ‘stiffer’ bond response and the resulting spacing is smaller (about 145 mm).

4.5.3 Discussion and Summary of Prism Test

For a given strain in concrete, the resulting deformation is the sum of the crack widths. To ensure good serviceability, ductility and continued adequate bond, it is desirable to have a *large number of smaller cracks*. However, crack widths are a function of both bar modulus and bond characteristics. Crack width is proportional to modular ratio ($E_{steel}/E_{titanium}$ or E_{steel}/E_{GFRP}), while spacing is inversely proportional to the stiffness of the initial bond-slip response. Therefore, a lower modulus bar will exhibit larger crack widths unless bond characteristics are improved proportionally. This is why sand-coated GFRP is often preferred to ribbed GFRP. The sand-coated bars have an improved bond characteristic which results in smaller crack spacing and thus smaller crack widths at a given strain than when ribbed bars are used (it was shown in Figures 4.4 and 4.9 that ribbed GFRP has similar bond characteristics to steel bars).

It is *hypothesized* that were Heat 3 titanium bars available for this test, since the bond characteristics were improved, the crack spacing would decrease (likely to approximately 200 mm) and only the crack width would remain greater than that for steel.

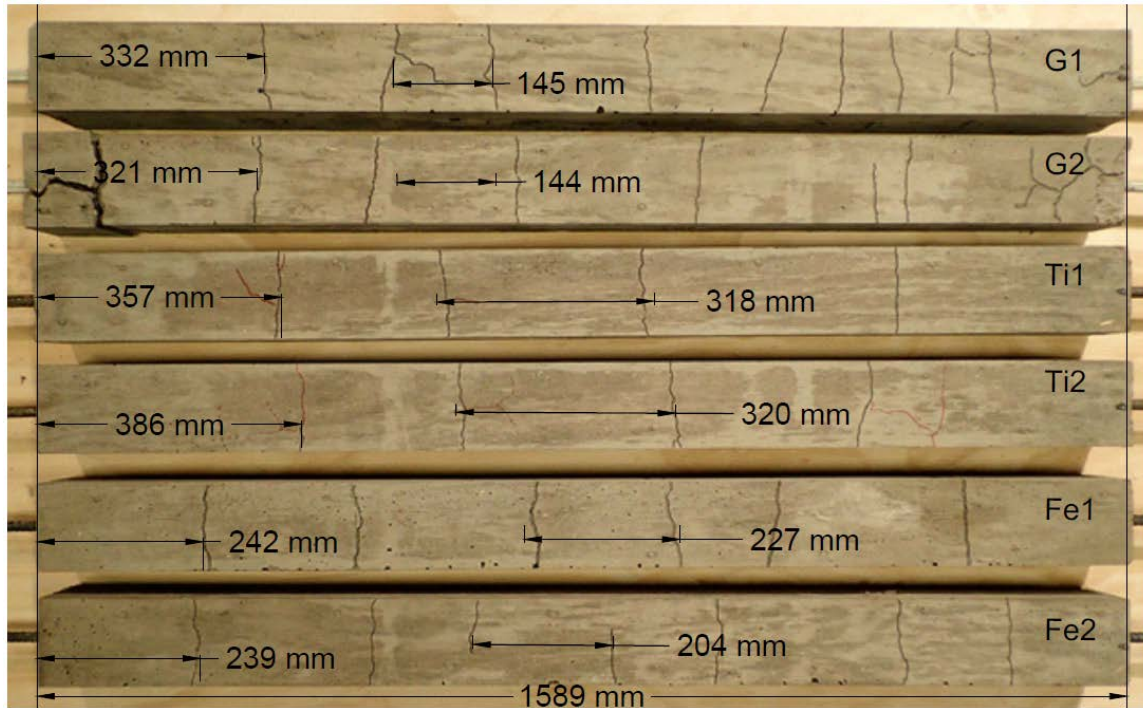


Figure 4.22 Prism specimens following testing showing crack patterns (from top to bottom: sand-coated GFRP (2 specimens), titanium heat 1 (2 specimens) and steel (2 specimens))

Table 4.9 (part 1) Crack history, widths and spacing for prism tension tests (A615 steel)

Specimen I.D.	Fe1			Fe2				
	ASTM A615 steel							
yield stress of bar	464 MPa							
	stress in...	load (kN)	stress		load (kN)	stress		
	concrete ²		1.91 MPa	$0.36\sqrt{f'_c}$		1.38 MPa	$0.26\sqrt{f'_c}$	
first crack	bar ¹	30.7	MPa	$1/f_y$	22.3	MPa	$1/f_y$	
			154	0.33		111	0.24	
subsequent cracks at	bar ¹	35.6	178	0.38	25.9	130	0.28	
		35.6	178	0.38	25.9	130	0.28	
		36.1	181	0.39	25.9	130	0.28	
		43.1	215	0.46	38.0	190	0.41	
		49.2	246	0.53	39.3	197	0.42	
						44.5	223	0.48
		crack width	strain ³	bar stress ¹	crack width	approx. strain	bar stress ¹	
load step	mm	mm/mm	$1/f_y$	mm	mm/mm	$1/f_y$		
sum of cracks widths	≈76 kN	1.52	0.001	0.82	1.27	0.0008	0.82	
	≈125 kN	-	-	-	-	-	-	
	≈173 kN	-	-	-	-	-	-	
crack spacing	avg. (COV)	227 mm (0.18)			204 mm (0.22)			

¹ Stress calculated using nominal bar area: $A_b = 200 \text{ mm}^2$ and experimentally determined f_y shown

² Stress calculated using gross concrete area: $A_g = 16000 \text{ mm}^2$ and $f'_c = 28.3 \text{ MPa}$

Table 4.9 (part 2) Crack history, widths and spacing for prism tension tests (titanium)

Specimen I.D.		Ti1			Ti2		
yield stress of bar		heat 1 titanium bars					
yield stress of bar		1055 MPa					
	stress in...	load (kN)	stress		load (kN)	stress	
	concrete ²		1.85 MPa	$0.35\sqrt{f'_c}$		2.21 MPa	$0.42\sqrt{f'_c}$
first crack	bar ¹	29.8	MPa	$1/f_y$	35.6	MPa	$1/f_y$
			149	0.14		199	0.17
subsequent cracks at	bar ¹	31.6	158	0.15	36.7	183	0.17
		35.3	177	0.17	39.7	199	0.19
		39.4	197	0.19	41.1	205	0.19
		crack width	strain ³	bar stress ¹	crack width	approx. strain	bar stress ¹
	load step	mm	mm/mm	$1/f_y$	mm	mm/mm	$1/f_y$
sum of cracks widths	≈76 kN	2.54	0.0016	0.36	2.32	0.0012	0.36
	≈125 kN	4.83	0.003	0.57	3.89	0.0024	0.59
	≈173 kN	8.13	0.0051	0.82	5.59	0.0036	0.82
crack spacing	avg (COV)	318 mm (0.16)			320 mm (0.21)		

¹ Stress calculated using nominal bar area: $A_b = 200 \text{ mm}^2$ and experimentally determined f_y shown

² Stress calculated using gross concrete area: $A_g = 16000 \text{ mm}^2$ and $f'_c = 28.3 \text{ MPa}$

Table 4.9 (part 3) Crack history, widths and spacing for prism tension tests (Sand-coated GFRP)

Specimen I.D.		G1			G2			
yield stress of bar		sand-coated GFRP bars						
yield stress of bar		738 MPa						
	stress in...	load (kN)	stress		load (kN)	stress		
	concrete ²		0.84 MPa	$0.16\sqrt{f'_c}$		2.09 MPa	$0.39\sqrt{f'_c}$	
first crack	bar ¹	13.5	MPa	$1/f_{tu}$	33.5	MPa	$1/f_{tu}$	
			67.6	0.09		168	0.23	
subsequent cracks at	bar ¹	27.0	135	0.18fy	38.3	192	0.26	
		27.2	136	0.18fy	40.0	200	0.27	
		36.3	181	0.25fy	40.0	200	0.27	
		36.3	181	0.25fy	41.1	205	0.28	
		36.3	181	0.25fy	43.6	218	0.29	
		36.3	181	0.25fy	46.5	232	0.31	
		40.3	201	0.27fy	X			
		52.0	260	0.35fy				
	load step	mm	mm/mm	$1/f_{tu}$	mm	mm/mm	$1/f_{tu}$	
sum of cracks widths	≈76 kN	6.86	0.0044	0.52	8.13	0.0051	0.51	
	≈125 kN	-	-	-	-	-	-	
	≈173 kN	-	-	-	-	-	-	
crack spacing	avg (COV)	145 mm (0.60)			144 mm (0.56)			

¹ Stress calculated using nominal bar area: $A_b = 200 \text{ mm}^2$ and experimentally determined f_y shown

² Stress calculated using gross concrete area: $A_g = 16000 \text{ mm}^2$ and $f'_c = 28.3 \text{ MPa}$

4.6 SUMMARY OF BOND CHARACTERIZATION OF TITANIUM REINFORCING BARS

In this Chapter, bond characteristics of the titanium bars were assessed through ASTM D7913 pull-out tests, ASTM A944 beam-end tests, and concrete prism tension tests. Both, the pull-out and beam-end tests are A-B tests that are best used to evaluate relative performance of reinforcing bars. The nature of reinforcing bar bond to concrete is such that deformed bars exhibited very similar patterns of bond stress-slip behavior. Provided adequate deformations are provided, the bond-slip relationship is dominated by concrete behavior. The bond performance of the titanium bars was similar to that of ASTM A615 steel bars and, as expected, affected by the rib ratio. The results presented reinforce the need to roll deformations such that the ASTM A615- implied lower limit for the rib ratio, $R_r > 0.05$ is satisfied. The implication of a similar bond-stress behavior is that existing bond relationships for steel-reinforced concrete apply to titanium bars provided they meet the deformation requirements of ASTM A615 – the standard for which steel reinforcing bars, and therefore their bond characterization – is calibrated. Both the pull-out and beam-end test results reinforce the conclusion that bond behavior of titanium bars is essentially the same as that steel bars. The bond stresses, normalized to account for variation in concrete strength, are similar and the calculated development lengths are essentially in the ratio of yield strengths of the materials.

For a given strain in concrete, the resulting deformation is the sum of the crack widths. To ensure good serviceability, ductility and continued adequate bond, it is desirable to have a large number of small cracks. However, crack widths are a function of both bar modulus and bond characteristics. Crack width is proportional to modular ratio ($E_{steel}/E_{titanium}$), while spacing is

inversely proportional to the stiffness of the initial bond-slip response. Therefore, a lower modulus bar will exhibit larger crack widths unless bond characteristics are improved proportionally.

A limitation of this study is that the beam-end tests of titanium did not have sufficient embedment to develop yield of the bar. As illustrated in Figure 4.15, bond failure is characterized by longitudinal cracking and eventual slip. It has not been demonstrated that the bond capacity sufficient to fully develop a titanium bar can be achieved at the strains necessary to do so. Therefore, the following recommendation is made.

4.6.1 Bond and Development Length Recommendation for Titanium Bars

Provided the deformations of a titanium reinforcing bar meet the requirements of ASTM A615, the bond behavior is similar to that of steel reinforcement and therefore the development length may be calculated in a similar manner (Eq. 4.2). However, due to lack of data it remains unclear whether the full yield capacity of the titanium can be obtained through conventional straight-bar development. Therefore, in the absence of further data, the stress developed by the titanium bar should be limited to the maximum yield stress for which the current development length equations are calibrated. In the case of Eq. 4.2 [ACI 318], the bar stress should be limited to 550 MPa (80 ksi); this is approximately $0.55f_y$ for the titanium bars considered. This limitation may impact design of titanium reinforced members as discussed in Chapter 6. The ability of hooked or mechanical anchorages to develop titanium bars has not been studied in this work.

5.0 NSM TITANIUM REINFORCED SLAB TESTS

A primary anticipated application for titanium reinforcement is a near surface mounted (NSM) reinforcement for strengthening in cases where the advantages of titanium may be realized such as in a highly corrosive environment. A pilot study of this is described in this chapter. Four steel-reinforced bridge deck slabs, cast in 2013, were available to this study for testing. These slabs were designed based on the AASHTO (2017) prescriptive design method and had four #5 primary reinforcing bars spaced at 140 mm, top and bottom, across the 559 mm slab width. The ‘control’ specimen used for this study is Slab A, tested in 2013 [McCabe 2013; McCabe et al. 2014]. Details of the slabs geometry are shown in Figure 5.1.

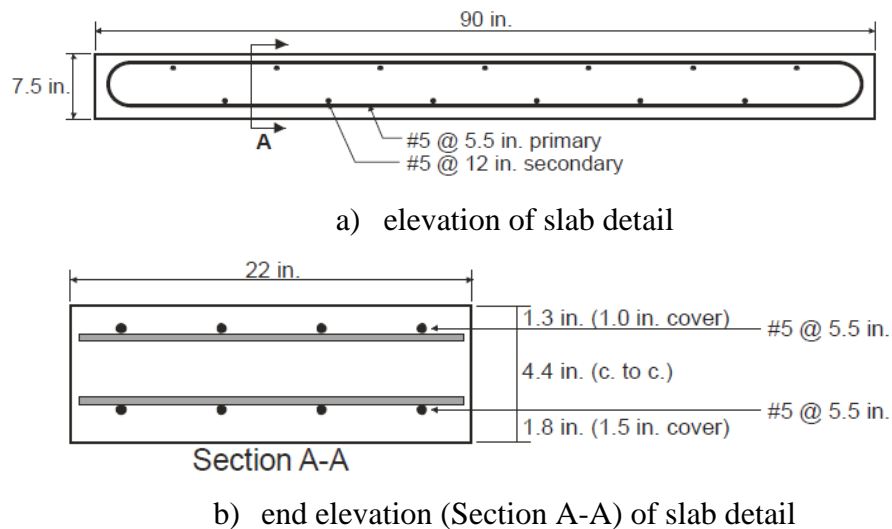


Figure 5.1 Details of laboratory control specimen and test arrangement [McCabe 2013] (1 in. = 25 mm)

The slabs were tested in mid-point flexure over a 2135 mm simple span. Primary instrumentation consisted of 8 in. (203.2 mm) gauge length DEMEC strain gauges centered on the span in order to provide a strain profile at midspan (Figure 5.5a). Tests of the four NSM titanium retrofit slabs were carried out in a manner (to the extent possible) identical to the control specimen: Slab A tested by McCabe [McCabe 2013; McCabe et al. 2014]. An extensive analytical study was also carried out by McCabe [2013]. The present study leverages both the experimental test results for the control specimen and the analytic model of the control specimen from this earlier study.

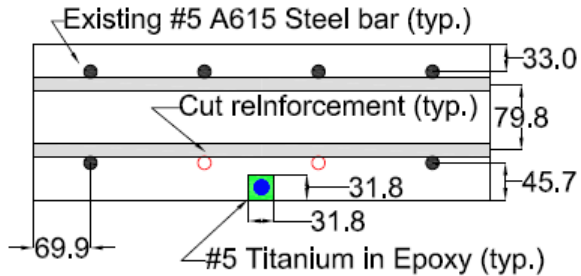
Four untested slabs ‘left over’ from the earlier study were used to demonstrate the proposed NSM titanium reinforcement. #5 titanium bars were embedded in an epoxy-bonded NSM application which was, other than the use of titanium, compliant with the design approach of ACI 440.2R-17. Two variations of the NSM repair were examined: using straight bars and ‘staples’. Details of the NSM installations and existing slabs are shown in Figure 5.2. The 1830 mm (72 in.) long straight bars are intended to represent a typical NSM repair in which retrofit is required over the length of a span such as in the case of severe [uniform] corrosion of existing reinforcement. The 406 mm (16 in.) long staples are a local repair intended to bridge local damage to existing reinforcement such as that which may be associated with impact damage [e.g., Kasan and Harries 2009].

In order to maintain an under reinforced section (so that tensile reinforcement continues to control the slab behavior), two of the four existing #5 steel bars were cut at increments along their length sufficient to ensure that the bars no longer contributed to the flexural capacity of the slabs. The internal bars were cut only at midspan for the slabs receiving NSM staples (local damage) while those receiving full-length straight NSM bars had their internal reinforcement cut

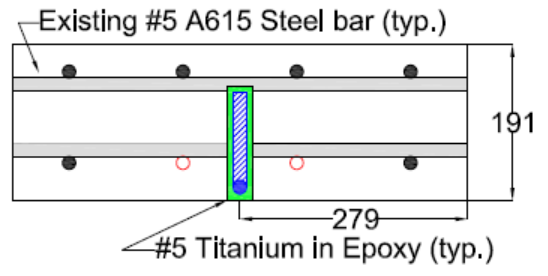
at five locations along the slab span. Locations of the cuts are shown in Figure 5.2 and can be seen in Figures 5.3b and c. The cut bars were then ‘replaced’ with NSM #5 titanium bars or staples as shown in Table 5.1 and Figure 5.2. The internal steel reinforcement in the slabs was the same ASTM A615 bars used in this study and the NSM titanium bars were from Heat 3; the geometric and material properties of all bars are given in Tables 3.3 and 3.1, respectively. Two NSM ‘designs’, representing the cases of essentially equal reinforcement capacity (replacement of cut bar capacity, $A_s f_y$) and equal reinforcement stiffness (replacement of cut bar axial stiffness ($A_s E_s$)) were tested.

Table 5.1 Demonstration tests

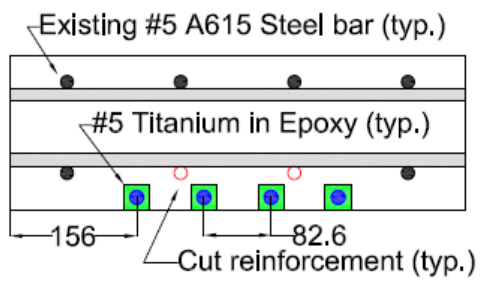
Slab ID	existing internal A615 steel	NSM titanium	Design
Control	4 - #5	-	tested and reported by McCabe (2013)
TiNSM-1	2 - #5	1 - #5 straight bar	equal strength: $A_s f_{ys} + A_{Ti} f_{yTi} \approx \text{control}$
TiNSM-3	2 - #5	1 - #5 staple	
TiNSM-2	2 - #5	4 - #5 straight bars	equal strength: $E_s A_s + A_{Ti} E_{Ti} \approx \text{control}$
TiNSM-4	2 - #5	4 - #5 staples	



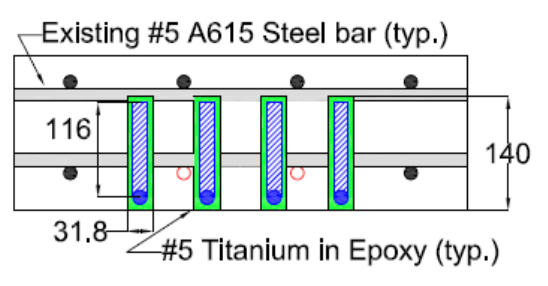
TiNSM-1 section – 1 bar centered in slab soffit



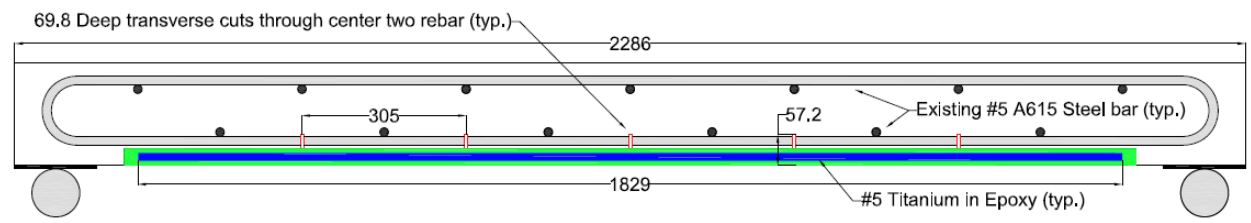
TiNSM-3 section – 1 staple centered in slab soffit



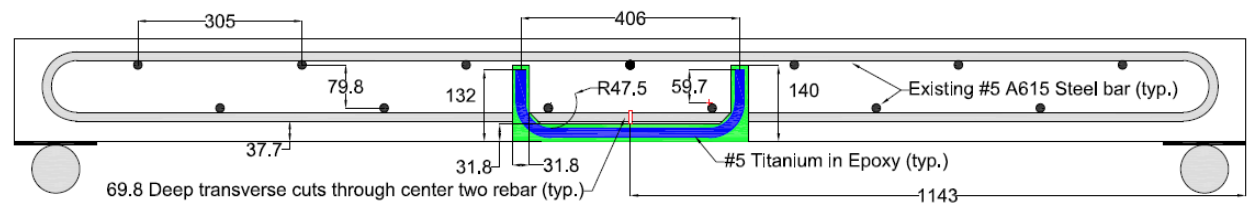
TiNSM-2 section – 4 bars at 83 mm across soffit



TiNSM-4 section – 4 staples at 83 mm across soffit



TiNSM-1 and TiNSM-2 elevation with NSM titanium straight bars (units = mm)



TiNSM-3 and TiNSM-4 elevation with NSM titanium staples (units = mm)

Figure 5.2 Cross sections and elevations of repaired slabs

5.1.1 Preparation of test slabs

Using the as-built slab drawings (Figure 5.1), the existing reinforcement was located and the location for the proposed NSM reinforcing schemes determined. Depth and width of the NSM slots must be as uniform as possible. This was accomplished by manufacturing a carriage system which ensured accurate and repeatable cuts in the tension face of the slabs. In overhead field applications, a rail system carrying a concrete saw would be bolted to the slab soffit [e.g., Figure 3.7 in Aidoo 2004]. The initial longitudinal and cross cuts were made using a 356 mm (14 in.) Makita DPC7301 Power Cut cutoff saw which was attached to the mobile chassis enabling precise depth control while being guided along a fence that was repositioned for each cut (Figure 5.3a). As seen in Figure 5.3b, the resulting cuts were very uniform.

After completing all longitudinal cuts at a depth of 31.8 ± 1.6 mm ($1.25 \pm 1/16$ in.), cross cuts of equal depth were made at the ends of the intended slot. The final cross-cuts were made to cut the existing reinforcing steel as shown in Figure 5.3b. These cuts were made to a depth 57.2 ± 3.2 mm ($2.25 \pm 1/8$ in.) so as to penetrate fully through the depth of the existing reinforcement. The slabs to receive NSM staples, received only a single cross cut through existing reinforcing steel at midspan (seen in Figure 5.4a) while those receiving straight NSM bars were cut at five locations along the length of the slabs (seen in Figure 5.3c). The straight NSM was 1829 mm (72 in.) long. This length was based on the hypothetical soffit length available on a bridge deck supported on girders having 305 mm (12 in.) flanges spaced at 2134 mm (84 in.).

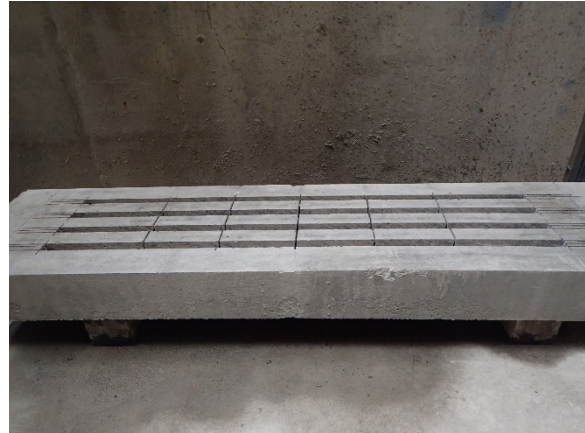
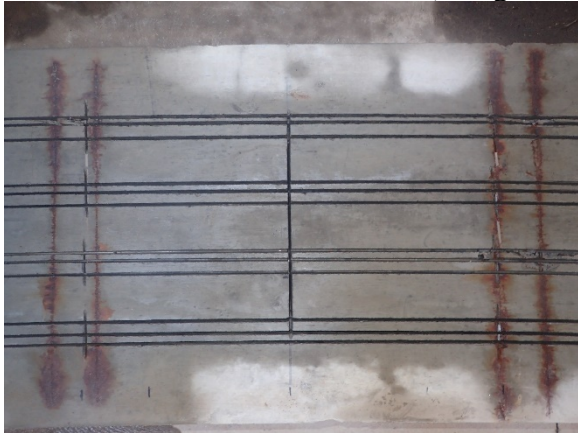
After all cuts had been made, the material bounded by the cuts was removed using a Dewalt SDS chipping hammer with a 19 mm (0.75 in.) bit. This produced a clean slot with

parallel sides to receive the NSM bars (seen in Figures 5.3c and 5.4d). Prior to NSM application, each slot was thoroughly cleaned and dried. Each slot was filled about halfway with Sikadur 31 epoxy and the titanium reinforcing bars were placed firmly into the epoxy, squeezing out air pockets and filling the sides of the slots (Figure 5.3d). After ensuring that each bar was properly seated, the remainder of the slot was filled with epoxy and troweled smooth (Figure 5.3e). Sikadur 31 is a commercially available two-part structural adhesive, based on a combination of epoxy resins and proprietary filler. The adhesive is commonly used to bond structural reinforcement in NSM applications. Sikadur 31 has manufacturer-reported 1-day tensile strength of 16 MPa (2.3 ksi) and bond strength to concrete exceeding 4 MPa (580 psi).

Slabs repaired using staples were prepared in a manner similar to that of the full-length repair specimens with the exception of the shorter length of slot and the addition of 25.4 mm (1.0 in.) holes to accommodate the legs of the staples as shown in Figure 5.4a. Care was taken to ensure that the length of the legs and depth of the holes did not interfere with the existing top bar reinforcement (see Figure 5.2). The interior edge of each hole was chamfered to accommodate the 47.5 mm (1.87 in.) bend radius of the staple. The staples were hot-bent as described in Section 3.1.3. Since the planned tests were monotonic in nature, the small cracks that occur at the tension face of the bend were not likely to affect the results of the present tests. Based on post-test evaluation, no issues associated with the bends were apparent. The remainder of the installation continued as previously described. Epoxy filled the entire depth of the hole accommodating the legs of the staples.



a) longitudinal cuts for channels



b) cross cuts through the existing A615 steel

c) clearing of channels for NSM titanium

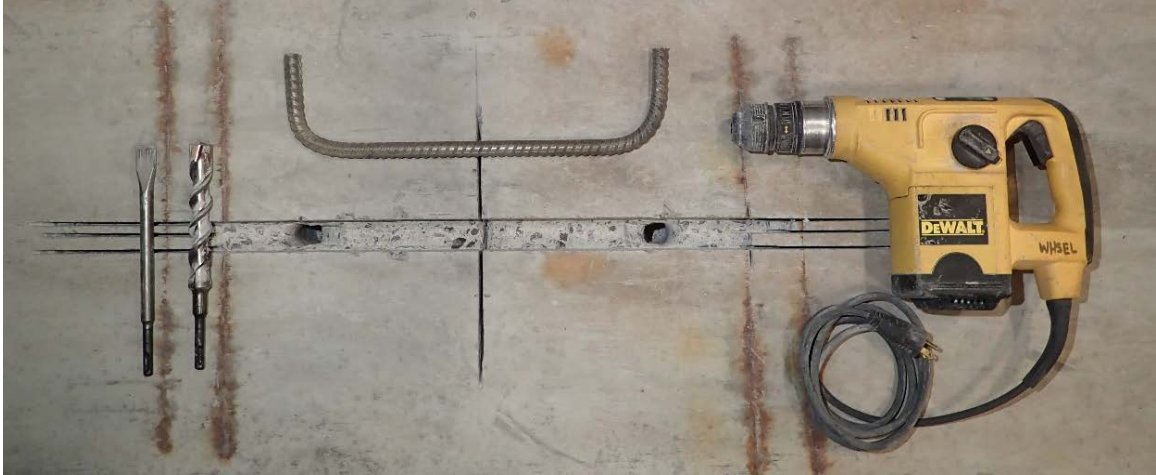


d) channels partially filled and NSM titanium placed

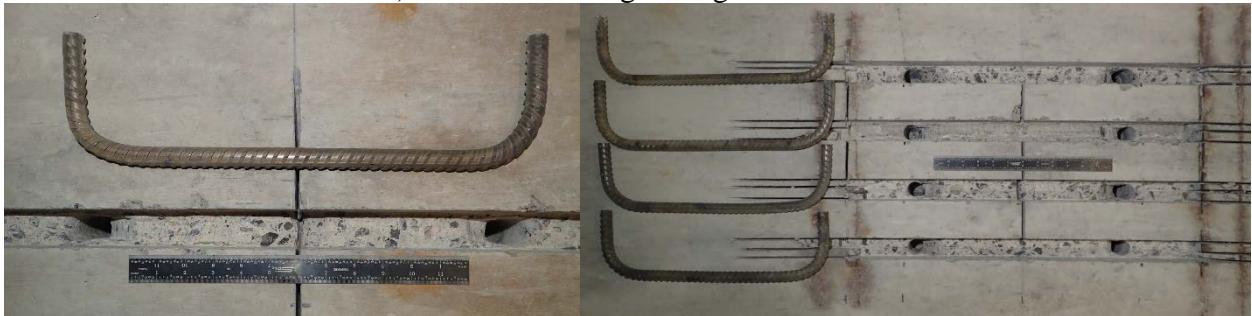


e) all channels filled and troweled smooth

Figure 5.3 Preparation of straight bar NSM repair specimens



a) slab after drilling for legs of stiches

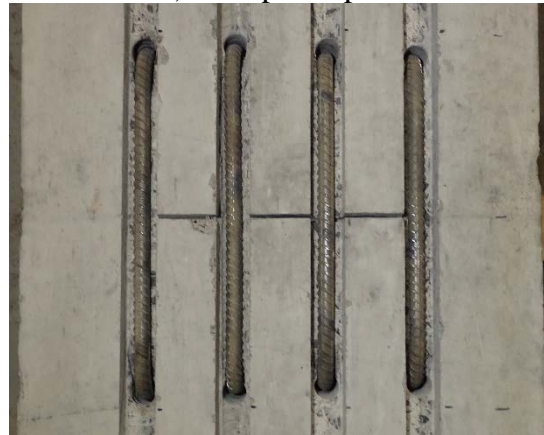


b) single staple

c) multiple staples



d) dry fit checking for clearance



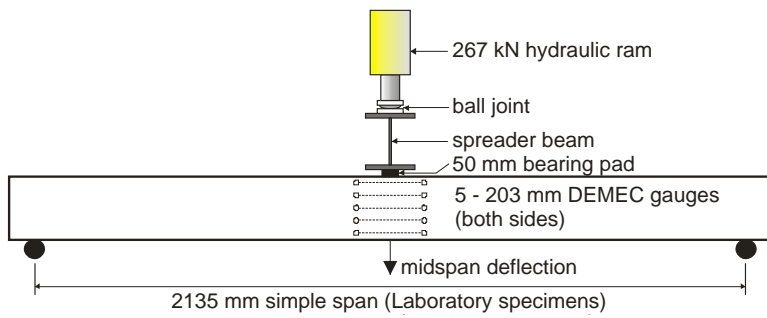
e) dry fit of multiple staples prior epoxy

Figure 5.4 Preparation of staple NSM repair specimens

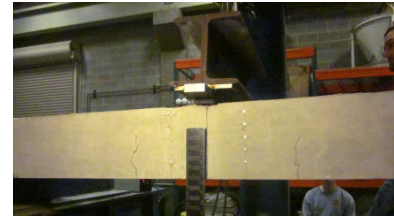
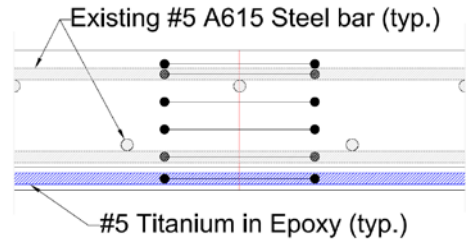
5.1.2 Testing of slabs

The NSM installations were permitted to cure a minimum of 72 hours before, the slabs were rotated and placed in the reaction frame. The same loading arrangement and support conditions as used by McCabe [2013] to test control Slab A were used (Figure 5.5a). The specimens were tested over a simple span length (L) of 2134 mm (84.0 in.). Prior to testing, each slab was checked for level and squareness across the entire slab width at each support. The slab ends were bedded in high strength plaster onto 559 x 152 x 9.5 mm (22 x 6 x 0.375 in.) steel reaction plates over rocker supports. When necessary, high points were removed from the top center of the slabs using an angle grinder and the midspan area of the beam was leveled with plaster to ensure a uniform loading surface across the entire slab width. A 50.8 mm wide x 12.7 mm deep (2 x 0.5 in.) 60 durometer rubber bearing pad was placed on the slab and the loading beam on top of this (Figure 5.5a).

Demountable mechanical (DEMEC) gauges having a 203 mm (8 in.) gauge length were installed at midspan on each side of each slab. The DEMEC gauges were located vertically at distances from the tension face representative of the depths of each reinforcement layer as shown in Figure 5.5b. Gauges were located as near as possible to the locations of the #5 titanium NSM, the existing un-cut #5 A615 steel tension and compression reinforcements, as near as possible to the compression face, at the slab midheight, and a sixth set of targets located to provide good resolution of the strain distribution as seen in Figure 5.5b.



a) test Set-up (Slab A shown)



b) DEMEC and vertical deflection instrumentation (Slab A shown)



c) DEMEC reader
(wexham-developments.co.uk)

Figure 5.5 Test Set-Up and Instrumentation [adapted from McCabe et al. 2014]

Prior to loading, existing cracks and visually noticeable surface imperfections were noted and pre-load (zero) DEMEC gauge readings recorded. It is noted that the ‘zero’ readings for the DEMEC gauges include the effects of self-weight of the slab and load apparatus – thus measured strains are those resulting from active loading only. Load was applied using a 267 kN (60 kip) capacity hydraulic cylinder – the loading arrangement has a precision of 320 N (72 lbs). Load was applied at intervals of approximately 4.45 kN (1.0 kip). Midspan displacement was recorded manually at each load interval with a precision of 0.8 mm (1/32 in.). A DEMEC instrument (Figure 5.5c), having a resolution of 8 microstrain, was used to record the change in length for

each DEMEC gauge at each load interval. As loading continued, the initiation of cracking and location of cracks were recorded. Subsequent crack elongation and crack widths were recorded at each load interval until slab failure.

5.1.3 Slab Concrete Properties

The slabs tested had been stored outdoors in Pittsburgh for the four years since they were cast. The compression and tensile strengths and modulus of rupture reported by McCabe (Slab A) are given in Table 5.9. No cylinders remained from the cast; therefore, core samples were taken from the slabs to confirm present *in situ* compressive and tensile strengths. Cores having a diameter of 57 mm (2.25 in.) were removed from the [essentially undamaged] support region of the slabs following testing. Core concrete strength is affected by the location of the concrete within the structural element, with concrete at the bottom of a placement tending to be stronger (denser) than the top, although this variation is not expected to be significant for 203 mm (8 in.) thick slabs. Cores were cut into the slab soffits in a downhand orientation. Full depth 203 mm (8 in.) cores were taken. These were long enough to permit subsequent cutting of specimens having an aspect ratio, L/D , near 2 and to provide representative samples from the compressive (top) and tension (bottom) areas of the slab.

The compressive strength of small diameter cores is known to be somewhat lower and more variable than those of ‘standard’ 100 mm (4 in.) or 152 mm (6 in.) diameter cores. In addition, smaller diameter cores appear to be more sensitive to effects of the length-diameter (L/D) ratio. ASTM C39-16-specified correction factors applicable for normal-density concrete having nominal concrete strengths from 14 to 42 MPa (2000 to 6000 psi) were applied to all

reported data; correction factors for concrete strengths exceeding this range may be marginally different [ASTM C39-16]. In addition, the wet-drilled cores were allowed to dry in ambient conditions for 24 hours in order to remove moisture gradients that may have been present *in situ*.

The compression and tension strengths obtained from the 57 mm cores (including all corrections) are shown in Table 5.2. An expected increase in compressive strength is observed. Although values of splitting tensile strength apparently fall marginally, the variation of these tests suggests no significant change. The 1666 day tested strengths reported in Table 5.2 were used for all subsequent analyses of the slabs. The 132-day strength was used for Slab A.

Table 5.2 Concrete slab properties

Age		ASTM C39				ASTM C496				ASTM C78			
		Compression test				Split Cylinder test				Modulus of rupture			
Date	days	n	f_c'		COV	n	f_{sp}		COV	n	f_r		COV
			MPa	ksi			MPa	psi			MPa	psi	
02/13/13	28 ^a	3	44.8	6.50	0.034	3	3.12 = 0.47 $\sqrt{f_c'}$	453 = 5.6 $\sqrt{f_c'}$	0.131	3	5.45 = 0.81 $\sqrt{f_c'}$	790 = 9.8 $\sqrt{f_c'}$	0.056
06/25/13	132 ^a	3	45.8	6.65	0.084	-	-	-	-	-	-	-	-
08/09/17	1666	8 ^b	50.7	7.35	0.081	5 ^c	2.98 = 0.42 $\sqrt{f_c'}$	432 = 5.0 $\sqrt{f_c'}$	0.186	-	-	-	-

^a McCabe [2013], slab cast date: January 16, 2013

^b 8 cores total (5 from top and 3 from bottom of slab)

^c Splitting tensile data for bottom of slab only (5 cores)

5.1.4 Test Results

Table 5.3 summarizes the key results from the control Slab A [McCabe 2013] and the NSM-repaired slabs. The reported moment is calculated as: $M = PL/4$, where P is inclusive of the cross-head contribution but neglects the weight of the slab. The curvature is calculated by dividing the difference in strain between the uppermost DEMEC gauge and the gauge located at the existing A615 steel tension reinforcement by the vertical distance separating these gauges. This is consistent with the procedure used for the control Slab A. The calculated moment-curvature for each slab tested along with the control slab is shown in Figure 5.6.

Table 5.3 Summary of tested slabs

Slab		A	TiNSM-1	TiNSM-2	TiNSM-3	TiNSM-4
depth of slab	mm	191	216	191	191	191
	in.	7.5	8.5	7.5	7.5	7.5
NSM bars		none	1 - #5 straight bar	4 - #5 straight bars	1 - #5 staple	4 - #5 staples
load at first crack	kN	22.6	23.1	28.2	28.2	32.6
	kips	5.08	5.20	6.33	6.33	7.33
moment at first crack	kN-m	12.1	22.1	15.0	15.0	17.4
	k-ft.	8.89	16.3	11.1	11.1	12.8
load at internal reinforcing bar yield	kN	81.0	81.8	104	72.5	113
	kips	18.2	18.4	23.3	16.3	25.3
moment at internal reinforcing bar yield	kN-m	43.1	43.6	55.3	38.7	60.1
	k-ft.	31.8	32.1	40.8	28.6	44.3
ratio yield capacity to Slab A	-	-	1.01 0.89 ¹	1.28	0.90	1.39
deflection at reinforcing bar yield	mm	9.65	5.59	6.35	5.59	11.2
	in.	0.38	0.22	0.25	0.22	0.44
curvature at reinforcing bar yield	rad/km	25.6	16.6	21.2	18.4	14.4
	rad/in (x 10 ⁻⁶)	650	422	538	467	366
ultimate load	kN	125	179	192	117	130
	kips	28.0	40.3	43.3	26.3	29.3
ultimate moment	kN-m	66.6	95.7	103	62.5	69.6
	k-ft.	49.1	70.6	75.8	46.1	51.3
ratio ultimate capacity to Slab A	-	-	1.44 1.12 ¹	1.55	0.94	1.05
deflection at ultimate load	mm	-	32.5	15.0	25.4	31.0
	in.	-	1.28	0.59	1.00	1.22
failure mode		flexural	flexural	shear	flexural	flexural at end of staples

¹ value normalized to 191 mm slab depth; i.e.: Slab TiNSM-1 ratio multiplied by (191/216)²

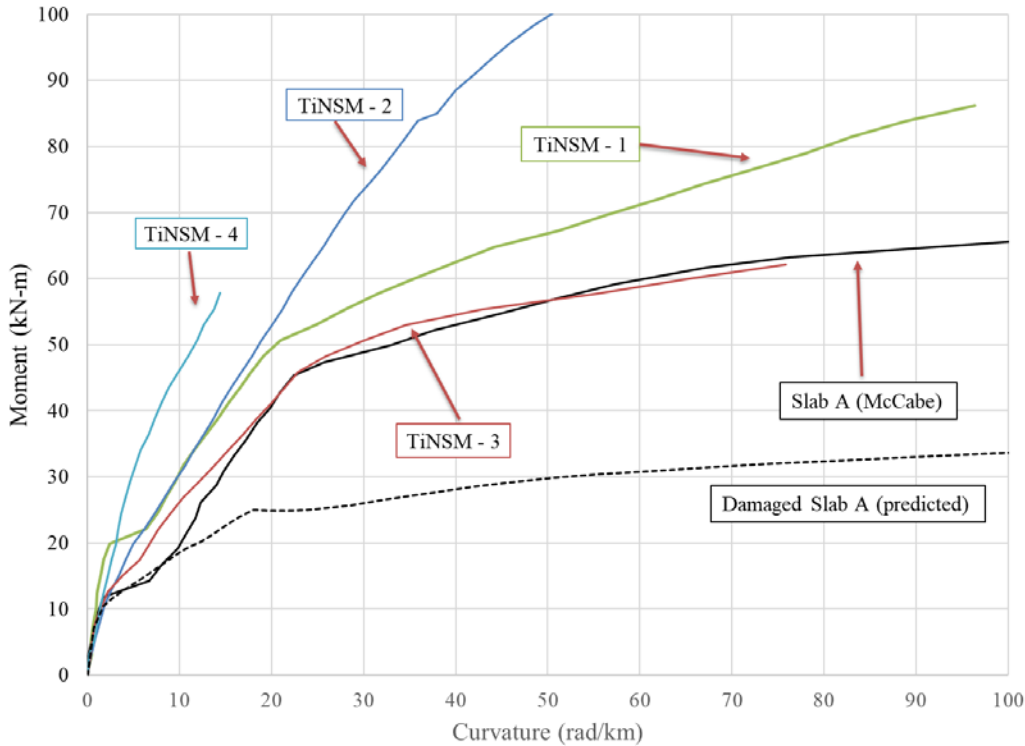


Figure 5.6 Summary of Moment-Curvature results from slab flexure tests

The behavior of the control slab was analyzed by McCabe [2013] using the program RESPONSE (Bentz 2000), a fiber-element plane-sections analysis tool. The predictive capacity of RESPONSE for these specimens was shown by McCabe to quite good. The analyses were repeated for the four tests conducted in this program as well as the slabs having only two continuous #5 bars (i.e., slabs with cut bars prior to NSM installation). All material properties used in the RESPONSE models are those given in Tables 3.1 and 5.2. Figure 5.7 shows the moment-curvature responses predicted for each slab tested and that for control Slab A superimposed with the as tested results. These predicted moment-curvature responses are for the critical section for flexure (midspan). The effects of shear-moment interaction in the relatively short shear spans having no shear reinforcement must also be considered and will marginally

reduce the predicted “pure” moment capacity. In the more heavily reinforced Slabs 2 and 4, the flexural capacity exceeds the slab shear capacity and the latter controls the predicted capacity. RESPONSE-predicted capacities are shown in Table 5.4. Complete moment-curvature, strain diagrams, and cracking patterns are shown in Figures 5.8 through 5.12.

Table 5.4 Summary of predicted capacities of NSM-reinforced slabs

	Slab A	Slab A with two bars cut	TiNSM-1	TiNSM-3	TiNSM-2	TiNSM-4
Predicted moment capacity (kNm)	57.3	34.3	84.1	65.6	134	
Predicted peak applied load (kN)	94.8	52.4	137	100	154	
moment capacity accounting for shear (kNm)	50.5	27.9	72.8	53.5	82.3	
Observed moment capacity (kNm)	66.6	-	84.6 ¹	62.5	103	69.6
Capacity normalized to Slab A	1.0	-	1.27	0.94	1.55	1.05

¹ value normalized to 191 mm slab depth; i.e.: Slab TiNSM-1 ratio multiplied by $(191/216)^2$

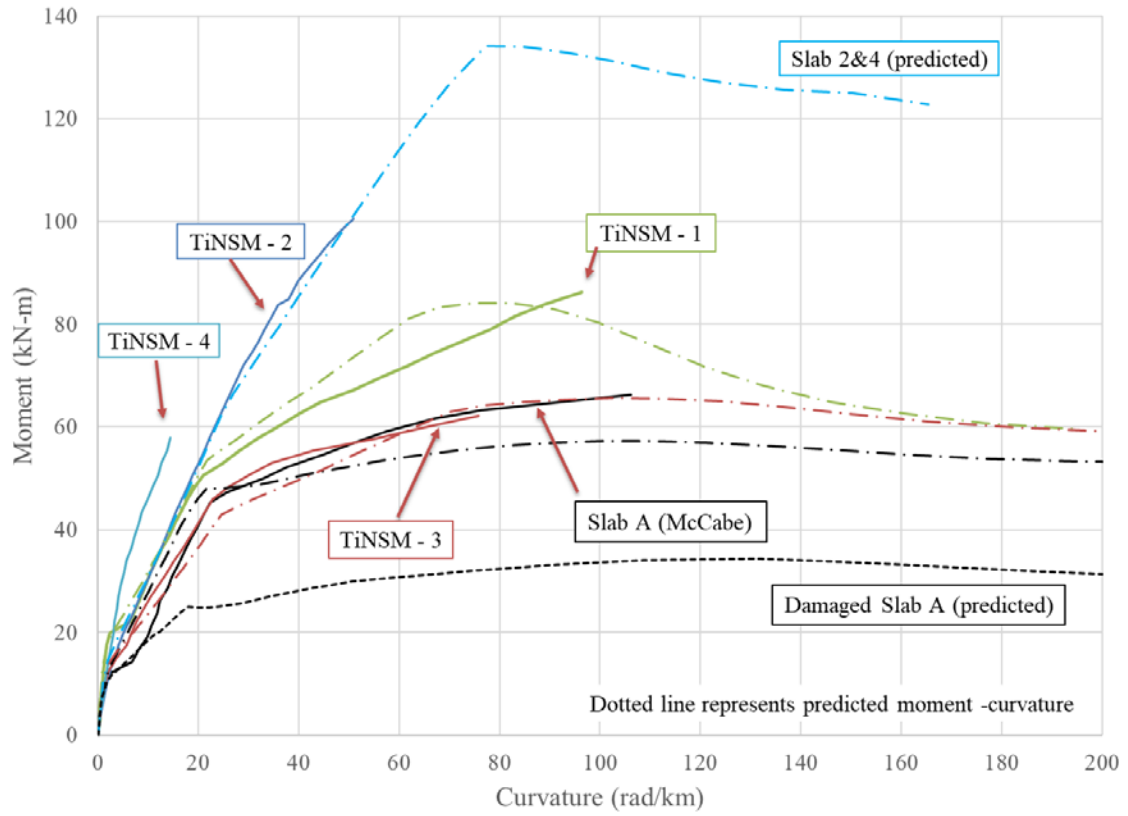
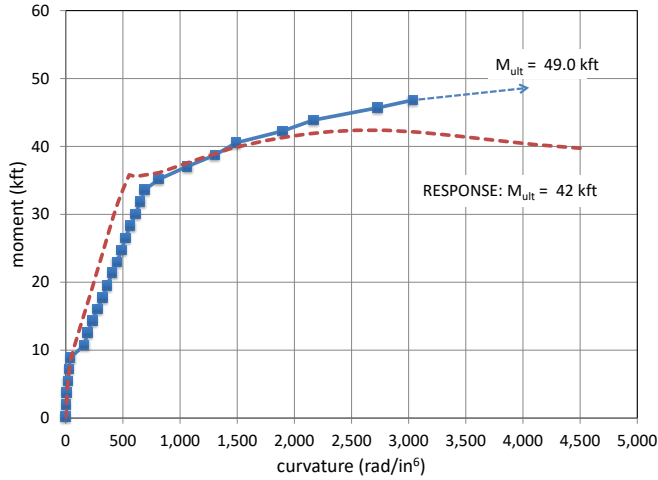
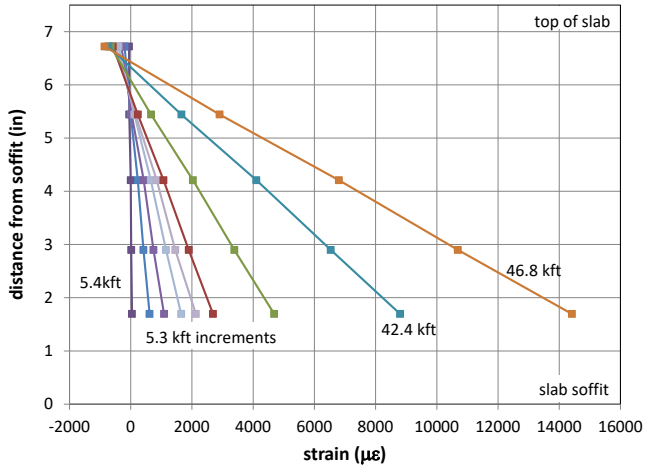


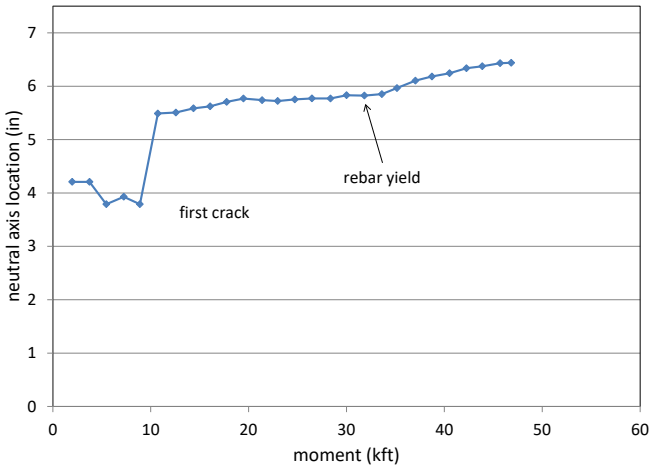
Figure 5.7 Summary of Moment-Curvature results with RESPONSE predicted results



a) Moment-Curvature Plot



b) Strain Profiles



c) Location of Neutral Axis

(1 in. = 25.4 mm; 1 kip = 4.448 kN; 1 rad/in = 0.0394 rad/mm)

Figure 5.8 Summary of Slab A test results reproduced from McCabe [2013]



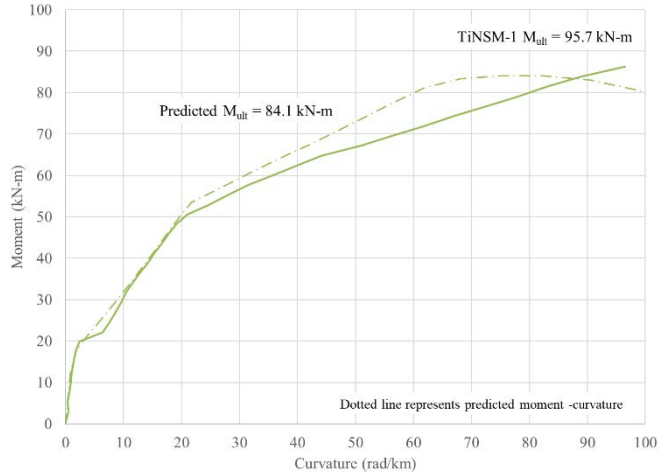
d) Reinforcement Yield (31.8 kipft)



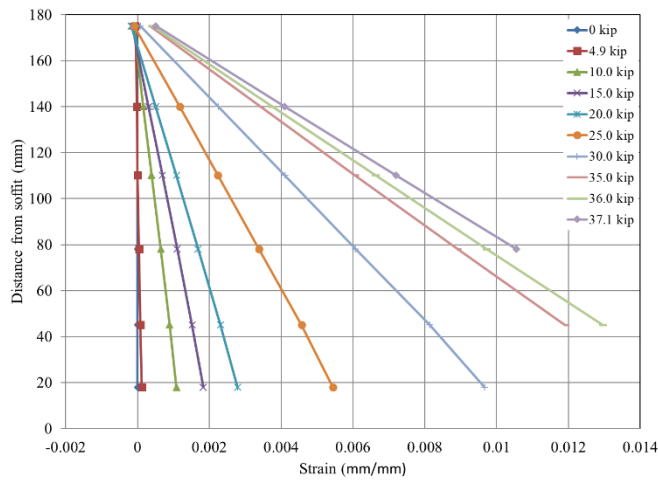
e) Final DEMEC Reading (46.8 kipft)



f) Ultimate Load (49.0 kipft)



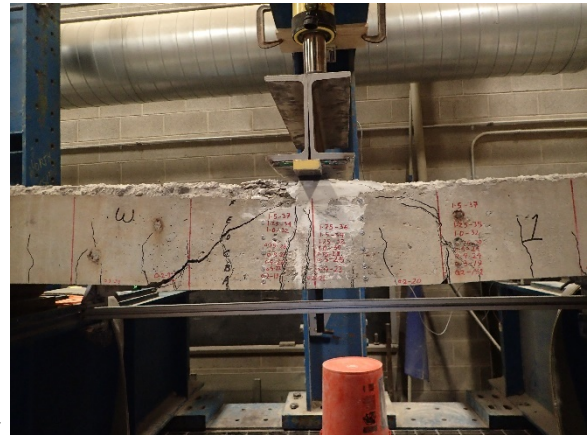
a) moment-curvature



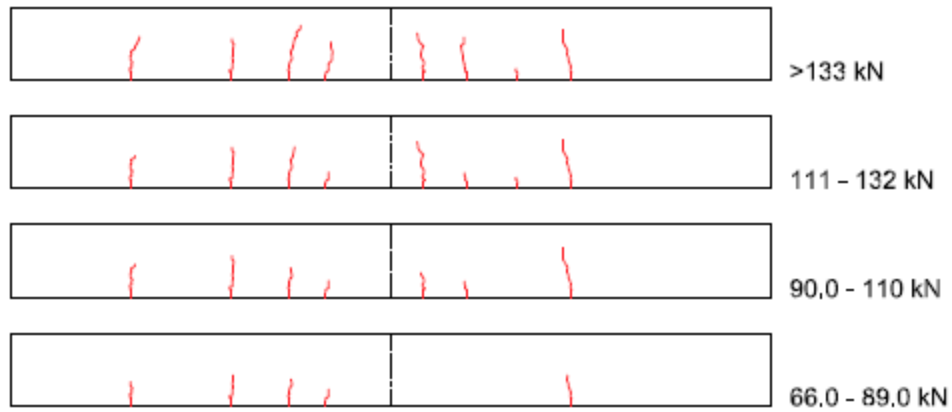
b) strain profile



c) \approx yield of A615 (43.6 kN-m)

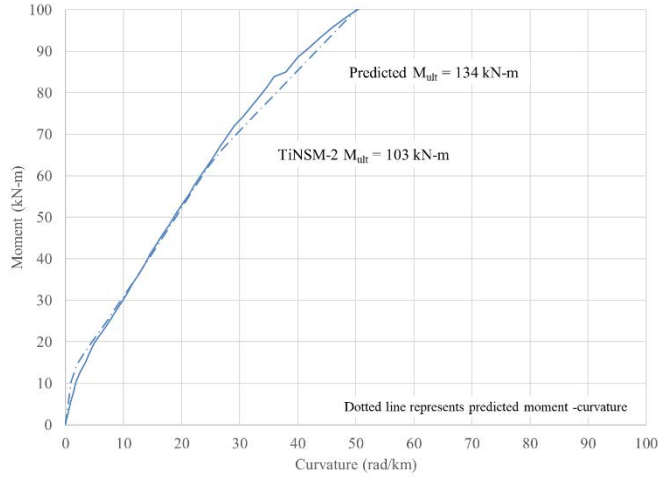


d) at ultimate load (95.7 kN-m)



e) observed crack development

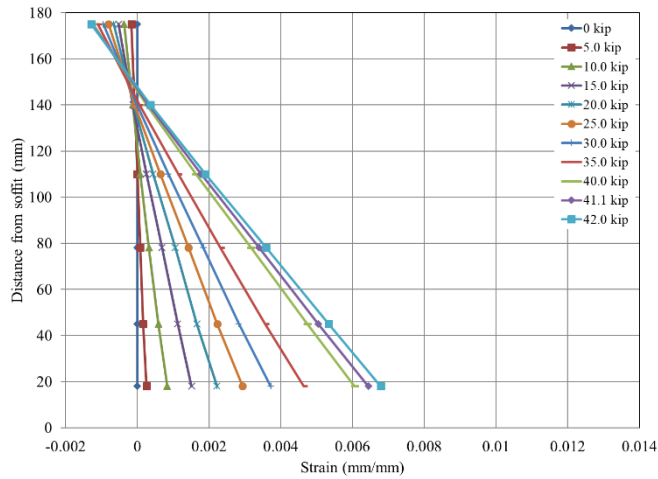
Figure 5.9 Summary of test results for TiNSM-1



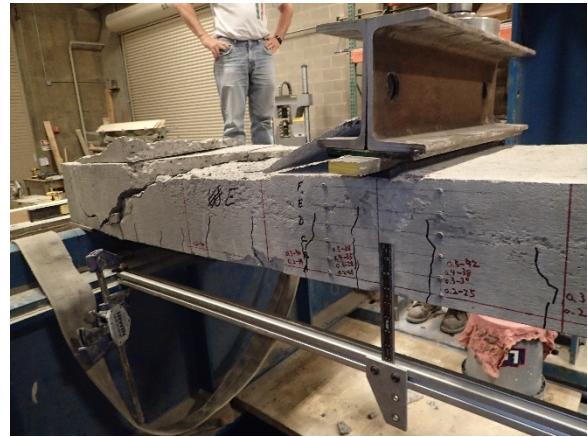
a) moment-curvature



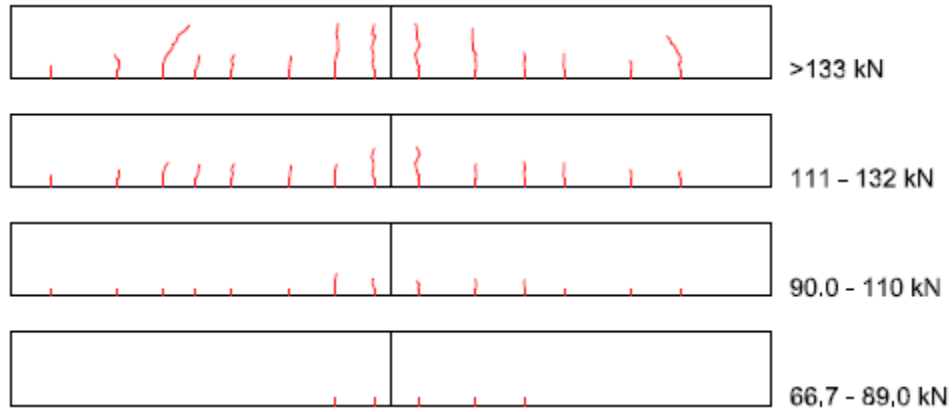
c) \approx yield of A615(55.3 kN-m)



b) strain diagram

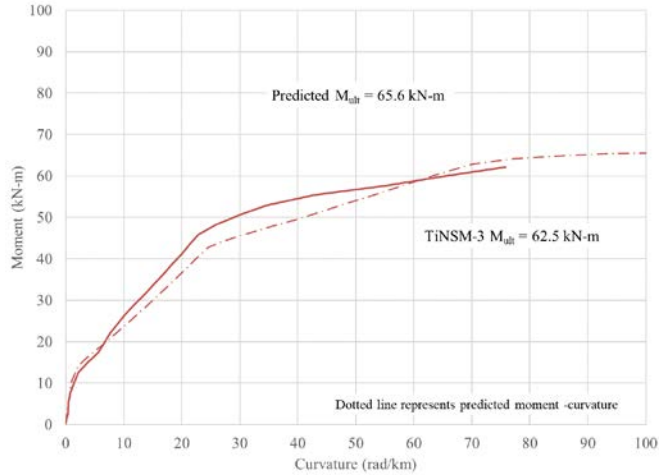


d) at ultimate load (103 kN-m)



e) observed crack development

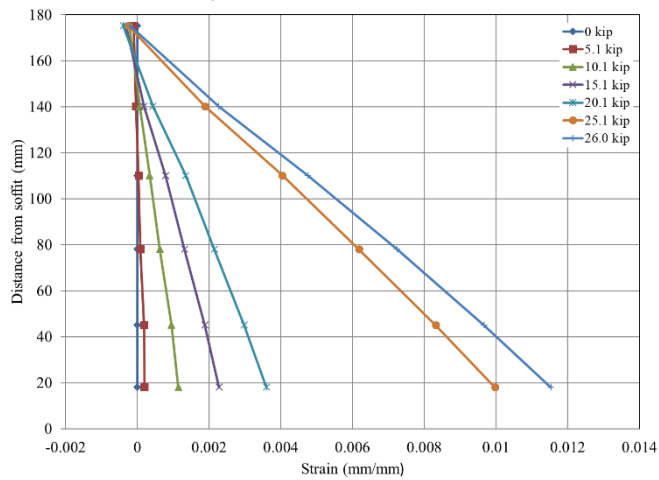
Figure 5.10 Summary of test results for TiNSM-2



a) moment-curvature



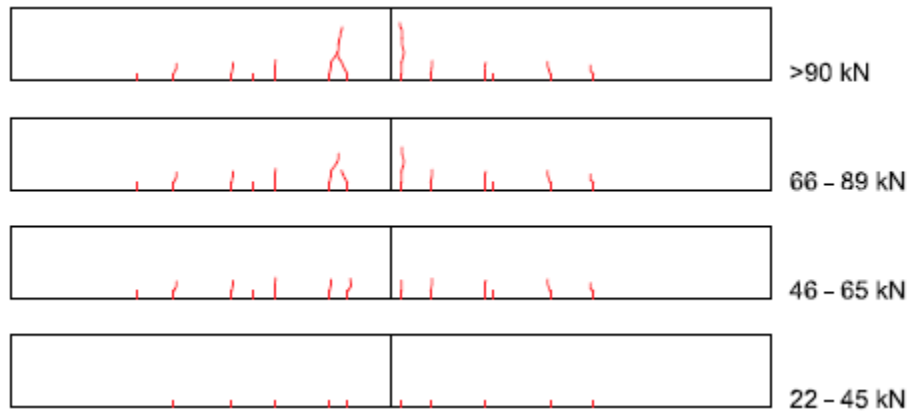
c) \approx yield of A615 (38.7 kN-m)



b) strain profile

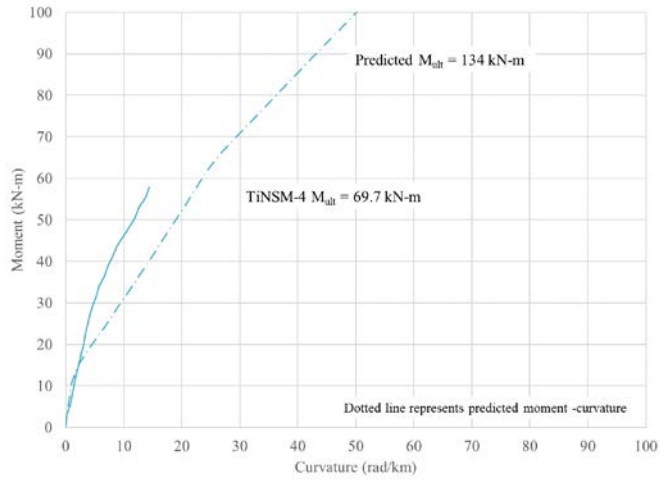


d) at ultimate load (62.5 kN-m)

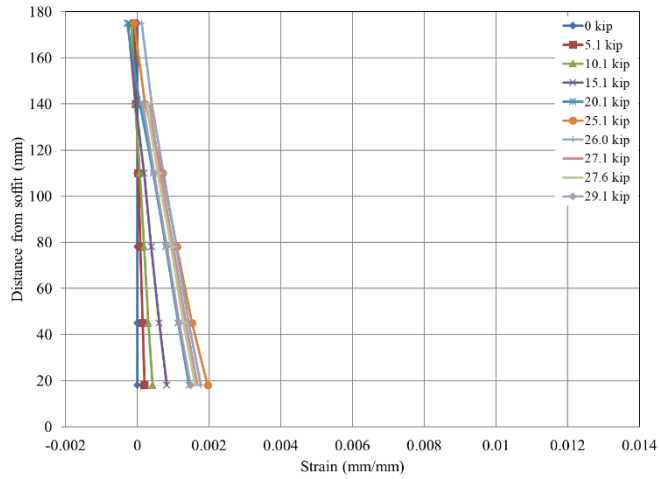


e) observed crack development

Figure 5.11 Summary of test results for TiNSM-3



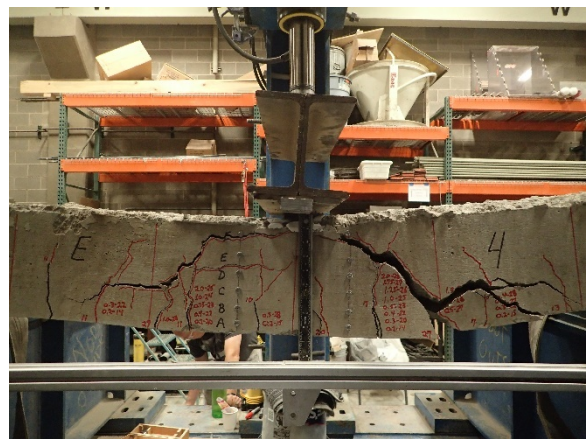
a) moment-curvature



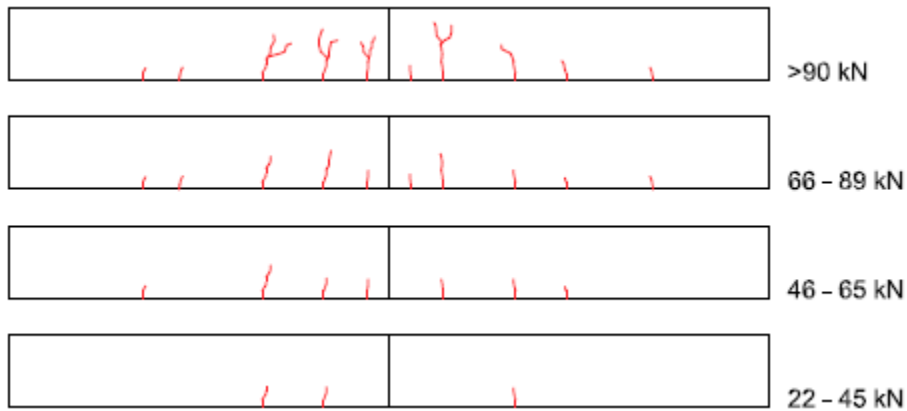
b) strain diagram



c) \approx yield of A615 (60.1 kN-m)



d) at ultimate load (69.6 kN-m)



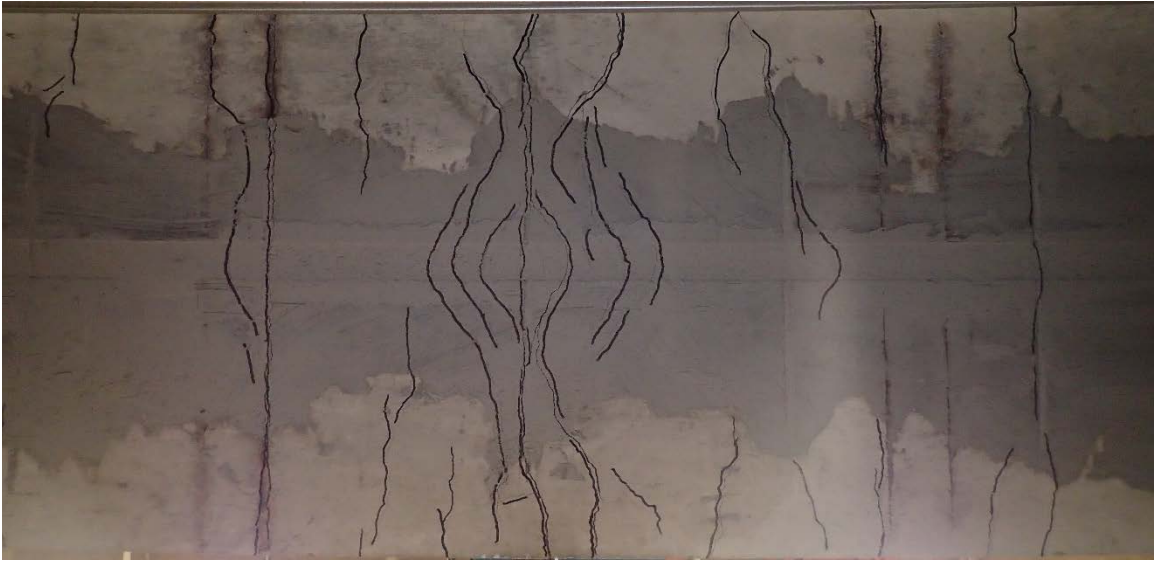
e) observed crack development

Figure 5.12 Summary of test results for TiNSM-4

5.1.4.1 Bar Slip of Slab TiNSM-1

Prior to failure, crack patterns were traced along the bottom of TiNSM-1 (Figure 5.13). As might be expected, Slab TiNSM-1, which consisted of a single full-length titanium NSM bar, exhibited cracking near the cuts that were used to eliminate the contribution of the existing two A615 steel reinforcing bars. The ‘fishbone’ cracking seen in Figure 5.13 is evidence of bond slip of the central NSM bar. Following failure, the slab was investigated closely and exhibited clear evidence of bond slip of the NSM bar (Figure 5.14). All slip occurred between the bar and epoxy. The bond between epoxy and surrounding concrete remained sound (Figures 5.14b and d). This behavior was not evident in the single staple repair, Slab TiNSM-3, where the bent bar anchorage resisted slip and slab failure was initiated at the outside edge of the hole drilled to accommodate the leg of the staple.

The slip of the single bar in TiNSM-1 indicates that it was unable to develop or maintain its capacity over the embedment provided. The development length of the NSM bar provided was 915 mm (36 in.), equal to 58 bar diameters. Using RESPONSE at the ultimate curvature of approximately 84.1 rad/km (2.14×10^{-3} rad/in.), the predicted stress is 1001 MPa = $1.0f_y$ in the NSM titanium bar and 487 MPa = $1.05f_y$ in the existing undamaged A615 Steel reinforcement. This result indicates that the $58d_b$ development was adequate to develop the NSM titanium bar although not without significant slip. The A615 bar is fully developed with 190-degree anchorages at both ends. Nonetheless, all reinforcing bars in TiNSM-1 were observed to yield; thus, the greatest theoretical capacity of the slab was attained (see Figure 5.8a).



a) prior to spalling



b) crack distribution near failure (fishbone crack pattern evident)

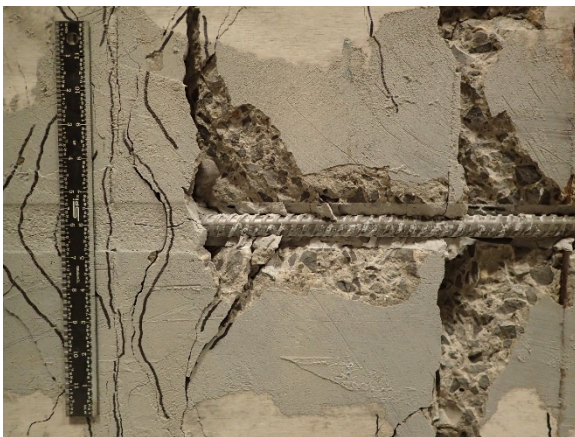
Figure 5.13 Crack distribution on the soffit of TiNSM-1



a) spalling at failure



b) good epoxy distribution – fishbone cracking of epoxy is evident



c) evidence of bar slippage



d) bar end showing clear plowing through epoxy by bar deformations



e) 8 mm gap at end of bar due to slippage

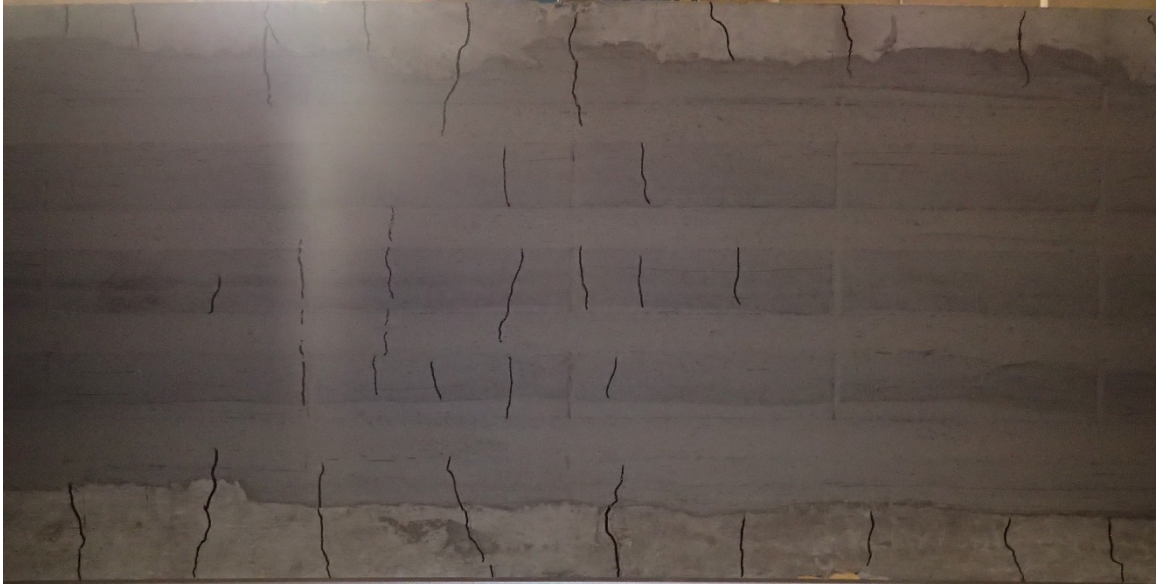


f) “plowed” epoxy built up along deformations

Figure 5.14 Bond performance of single straight bar NSM in Slab TiNSM-1

5.1.4.2 Slab TiNSM-2

TiNSM-2, having four straight NSM bars, exhibited the greatest capacity although did not achieve its theoretical flexural strength, ultimately failing in shear. Due to the large degree of strengthening in this case, the flexural capacity was increased to the extent that it exceeded the slab shear capacity. Relatively little flexural distress is seen in on the slab soffit (Figure 5.15a). The ultimate failure (Figures 5.15b-d) shows a classic shear failure characterized by a single large shear crack and delamination of the compression concrete. Figure 5.16 shows TiNSM-2 following removal of concrete in the midspan region. It is seen that very little damage occurred in the area surrounding the reinforcement. The titanium NSM bars spanning the cut internal steel bars have remained well bonded and effectively restored the capacity lost due to cutting the internal steel.



a) crack patterns on bottom of TiNSM-2



b) shear failure characterized by single dominant crack

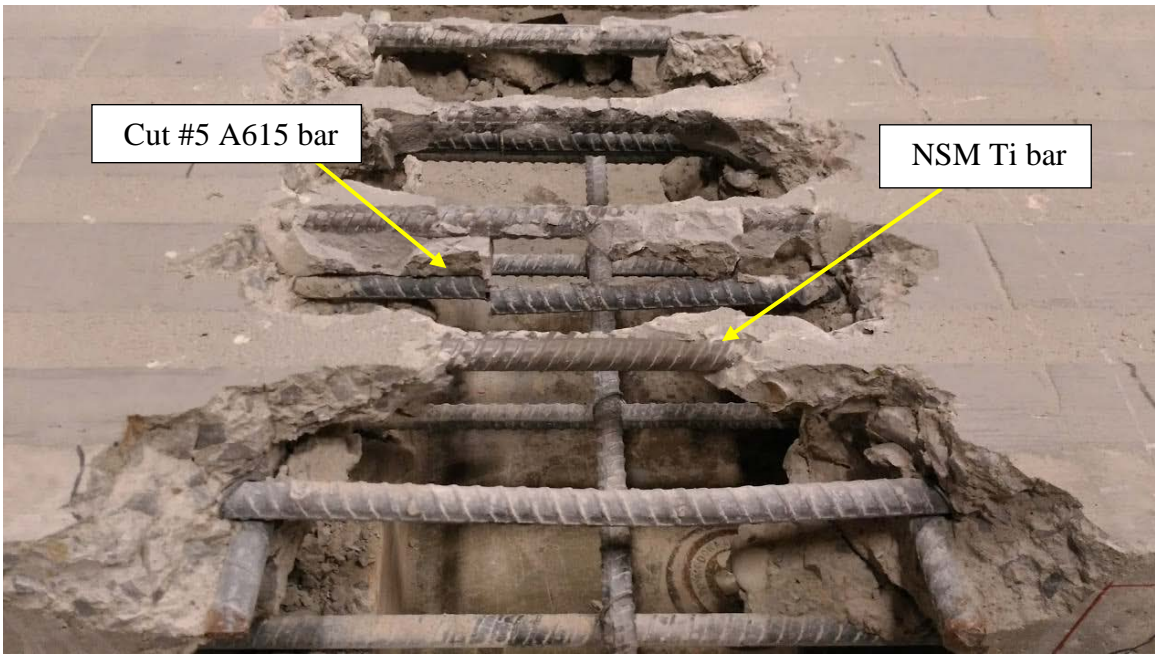


c) compression region delamination at failure



d) top reinforcement supporting slab

Figure 5.15 TiNSM-2 (4- #5 straight titanium bars)



cleared midspan showing cut existing bars

Figure 5.16 TiNSM-2 midspan (4 - #5 straight titanium bars)

5.1.4.3 Stapled slabs TiNSM-3 and TiNSM-4

Slabs TiNSM-3 and TiNSM-4 behaved in similar manners. Although TiNSM-4, having four staples was stiffer than TiNSM-3, having only one staple, both failed in a controlled manner and showed very little crack growth until near failure when large crack growth was observed near the locations of the vertical holes drilled to accommodate the legs of the staples. The staple legs, and change in slab stiffness at this location, therefore served as stress raisers and led to the ultimate failure of the slabs (Figures 5.17 and 5.18). As the slab began to fail, the larger cracks to either side of midspan (outside the DEMEC gauge length) increased allowing the cracks near midspan (within the gauge length) to stop opening and to close somewhat. This results in truncation of the curvature data available for these slabs. TiNSM-4 had a greater ultimate capacity and the failure was more brittle in nature.



a) bottom of TiNSM-3



b) side elevation of TiNSM-3 after removal from test frame



c) end of single staple



d) no slippage of staple

Figure 5.17 TiNSM-3 (1 - #5 titanium staple)



a) bottom of TiNSM-4



b) failed section at staple anchors following testing (staple anchors shown with arrows)
Figure 5.18 TiNSM-4 (4 - #5 titanium staples)

The slabs that were repaired using the staples had two of the four #5 ASTM A615 reinforcing bars cut midspan through the tension face of the slab. At this point the effective capacity of the slab dropped approximately 50% (Figure 5.5 and Table 5.4). The development length for the cut #5 bar is $l_d = 340$ mm (13.4 in.). Thus 340 mm to either side of midspan, the capacity of the cut #5 bars is theoretically restored [redeveloped]. The staples used were only 406 mm long and thus did not span the entire region of reduced capacity. Table 5.4 provides a summary of predicted responses and the resulting moment capacity envelopes (normalized to the predicted capacity of Slab A) are shown in Figure 5.19. The applied moments at failure are shown by the dashed lines. Clearly Slab A is critical at midspan. TiNSM-3 also predicts a midspan failure, although there is a relatively small margin at end of staple. The applied moment of TiNSM-4 is seen to intersect its capacity envelope at the end of the staples, rather than at the increased midspan capacity. Thus, the staples, in this case were too short to develop the predicted capacity of the repaired slab. The observed capacity of TiNSM-4 was considerably less than the predicted capacity of the slab (Table 5.4).

To mitigate the potential weak section at the staple anchorage, the anchorage should be located beyond the point where the cut bars have been fully redeveloped. That is, the staple length should exceed $2l_d$ (of the cut/damaged bars).

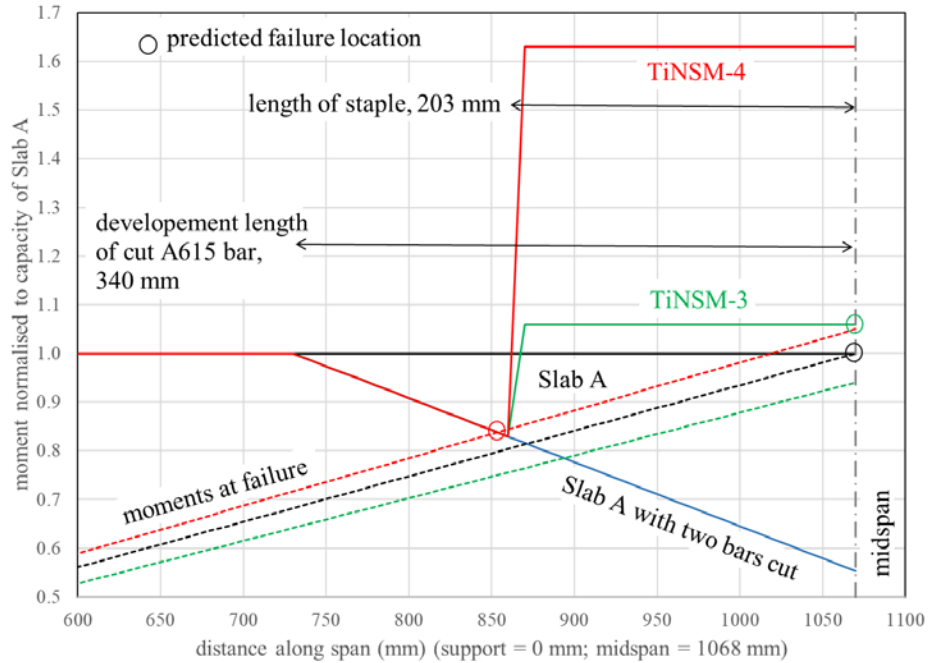


Figure 5.19 Generalized capacity envelope of the damaged slab with and without staple repair

5.2 SUMMARY OF SLAB TESTS

In this Chapter, the application of titanium NSM reinforcement was investigated through a pilot study using four steel-reinforced bridge deck slabs. The slabs and data for the control specimen, Slab A, was obtained from a previous study [McCabe 2013]. The slabs designated for Ti NSM repair had two of their four internal reinforcing bars cut – effectively halving the slab capacity. The objective of the NSM repair was to restore this capacity. The four Ti NSM-repaired slabs were divided into two groups based on a repairs that restore either the capacity ($A_s f_{ys} = A_{Ti} f_{yTi}$) or equivalent stiffness ($A_s E_s = A_{Ti} E_{Ti}$) of the cut bars. One slab from each group was repaired using a full-length straight bar while the other implemented a “staple” type repair, spanning only the location of the cut bars. Both straight bar repairs and the staple repair based on equivalent

stiffness restored the original slab capacity. The repair having the single titanium staple (TiNSM-2), theoretically sufficient to restore the capacity lost by cutting the internal reinforcement, restored only 94% of the original slab capacity. Slabs TiNSM-1 and TiNSM-3, each having only a single titanium bar, developed ductility similar to the undamaged control Slab A. Slabs TiNSM-2 and TiNSM-4 were both effectively over-reinforced leading increased capacity but decreased ductility. Slab TiNSM-2, having four full-length titanium NSM bars, failed upon reaching its shear capacity. TiNSM-4, having four titanium staples failed ‘prematurely’ in flexure at the section at the end of the staples; the staples were not long enough to develop the full theoretical capacity of this slab.

Both repairs however ultimately demonstrated some concerning issues with their failures. Although the titanium bar in TiNSM-1 appeared to yield, it experienced potential bond issues as there was evidence of significant bar slippage at the end of the bar. For TiNSM-3, the performance was nearly identical to that of the control slab, but the short staple length may have ultimately contributed to flexural failure at the end of the staple.

The remaining two slabs, TiNSM-2 and TiNSM-4 (four straight bars and staples, respectively, replacing two cut ASTM A615 bars), resulted in increased slab stiffness but reduced ductility. The resulting slabs were over-reinforced for flexure and ultimately a shear dominated failure was the result. TiNSM-2 experienced shear failure near the end of the developed length of titanium bars at one end of the slab span whereas TiNSM-4 failed along the transverse plane created by the end of the staples. It is hypothesized that if the staples had been designed to extend beyond the development length of the cut A615 internal reinforcing bars, the resulting performance of the NSM repairs would have been improved.

6.0 ANALYTICAL AND BENCHMARKING STUDY

Reinforced concrete design criteria are based on either strength or serviceability limit states. With the introduction of different reinforcing materials, consideration must be made as to how these materials impact extant design standards, or whether existing standards may be adopted for new materials at all. It has been shown that while the use of higher strength steel reinforcing bars is not prohibited, they greatly impact the performance and therefore the serviceability of a structure [e.g., Shahrooz et al. 2011]. Existing codes and standards must be re-evaluated to not only permit these newer and higher strength materials but must be adapted to embrace their performance characteristics.

The approach to flexural design of reinforced concrete is driven by fundamental mechanics and is based on Bernoulli beam theory simultaneously satisfying conditions of equilibrium and strain compatibility. That is, plane sections remain plane, and concrete strains are limited. For steel reinforced concrete, preferred designs are “under reinforced”, that is the steel yields and exhibits a degree of plastic deformation before the extreme compression concrete reaches its limiting compression strain of 0.003 [ACI 318-14]. Such behavior ensures ductility and is necessary for moment redistribution to occur in indeterminate structures. For cases that are not under reinforced, the designer is penalized with a reduced material resistance factor (ϕ). In GFRP-reinforced concrete, on the other hand, the reinforcement is brittle and must be “protected” from rupture. In this case, over reinforced members are used in which the concrete

reaches its limiting compression strain before the reinforcement reaches the limit of its (allowed) tensile behavior. Ductility is imparted, in this case, by the concrete crushing rather than reinforcement yielding [ACI 440.1R-15] and the designer is penalized otherwise. Table 6.1 summarizes flexure section design limits for steel and GFRP-reinforced concrete.

Table 6.1 Design paradigms for steel and GFRP-reinforced concrete

	steel-reinforced concrete (ACI 318-14 and AASHTO 2017)			GFRP-reinforced concrete (ACI 440.1R-15)		
	concrete	steel		concrete	GFRP	
under reinforced	$\epsilon_{cu} < 0.003$	$\epsilon_t > 0.005$ for $f_y \leq 552$ MPa $\epsilon_t > 0.008$ for $f_y \leq 827$ MPa	$\phi = 0.90$	$\epsilon_{cu} < 0.003$	$\epsilon_t > f_{fe}$	$\phi = 0.55$
interpolation permitted between limits						
over reinforced	$\epsilon_{cu} = 0.003$	$\epsilon_t < \epsilon_y$ for $f_y \leq 552$ MPa $\epsilon_t < 0.005$ for $f_y \leq 827$ MPa	$\phi = 0.65$	$\epsilon_{cu} = 0.003$	$\epsilon_t < 0.7f_{fe}$	$\phi = 0.65$
1 MPa = 0.145 ksi						

Deflection of reinforced concrete members is a function of $l/E_c I_e$ where E_c is the elastic modulus of the concrete. Calculation of short term deflection requires the determination of an average effective moment of inertia, I_e , for a cracked member. ACI 318 prescribes the Branson Equation for steel reinforced concrete:

$$I_e = \left(\frac{M_{cr}}{M_a}\right)^m I_g + \left[1 - \left(\frac{M_{cr}}{M_a}\right)^m\right] I_{cr} \leq I_g \quad (6.1)$$

Setting m equal to 4 accounts for the tensile contribution of concrete between cracks, referred to as ‘tension stiffening’, and gives an effective stiffness at the cracked section only. By setting m equal to 3, an average stiffness over the entire span is obtained which reflects the change in member stiffness, EI , along the length of the beam in addition to the tension stiffening effect of concrete [Bischoff 2005]. $m = 3$ is used by ACI 318.

Bischoff [2005] has pointed out that the Branson equation over estimates the average stiffness for concrete members with relatively small steel reinforcement ratios (when $\rho = A_{st}/bd$ is less than 1%) as well as underestimates short term deflections for very lightly reinforced members (where I_g/I_{cr} is large) [Gilbert 2006]. However, when GFRP reinforcement is used, which has a much lower modulus than steel, deflections increase rapidly in comparison to steel. This led to modifications of the Branson Equation by Benmokrane et al. [1996] where it was determined that the addition of a reduction factor when using GFRP would help to reduce the underestimation of deflection seen in Equation 6.1.

Building on the need for an accepted form of calculating the effective moment of inertia, ACI 440.1R-03 (Equation 6.3) introduced the parameter, β_d , which accounts for the bond properties and elastic modulus of FRP bars as given by Equation 6.4 where, α_b is a bond-dependent coefficient (can be taken as 0.5 for GFRP bars). Other studies determined that the relative reinforcement ratio also played a significant role in determining I_e . Experimental research conducted by Yost et al. [2003] further refined the bond-dependent coefficient to reflect the influence of the relative reinforcement ratio as shown in Equation 6.5.

Further modification would continue by ACI 440.1R-06 (Equation 6.6), Rafi and Nadjai [2009] (Equations 6.7 and 6.8), Bischoff [2005] (Equation 6.9), and the ISIS Canada Design Manual as presented by Mousavi et al. [n.d.] (Equation 6.10). These equations are presented in Table 6.2 and, while inconclusive, demonstrate the following:

- 1) Effective moment of inertia is affected by bond characteristics.
- 2) It is likely the bond characteristics of different FRP bars vary substantially since empirical parameters described in Table 6.2 are based on specific experimental data.

Table 6.2 Proposed calculations for the average effective moment of inertia

Benmokrane et al. [1996]	$I_e = \left(\frac{M_{cr}}{M_a}\right)^3 \frac{I_g}{7} + 0.84 \left[1 - \left(\frac{M_{cr}}{M_a}\right)^3\right] I_{cr} \leq I_g$	(6.2)
ACI 440.1R-03	$I_e = \left(\frac{M_{cr}}{M_a}\right)^3 \beta_d I_g + \left[1 - \left(\frac{M_{cr}}{M_a}\right)^3\right] I_{cr} \leq I_g$	(6.3)
	$\beta_d = \alpha_b \left(\frac{E_f}{E_s} + 1\right)$	(6.4)
Yost et al. [2003]	$\alpha_b = 0.064 \left(\frac{\rho_f}{\rho_{fb}}\right) + 0.13$	(6.5)
ACI 440.1R-06	$\beta_d = \frac{1}{5} \left(\frac{\rho_f}{\rho_{fb}}\right) \leq 1$	(6.6)
Rafi and Nadjai [2009]	$I_e = \left(\frac{M_{cr}}{M_a}\right)^3 \beta_d I_g + \frac{I_{cr}}{\gamma} \left[1 - \left(\frac{M_{cr}}{M_a}\right)^3\right] I_{cr} \leq I_g$	(6.7)
	$\gamma = \left(0.0017 \frac{\rho}{\rho_b} + 0.8541\right) \left(1 + \frac{E_f}{2E_s}\right)$	(6.8)
Bischoff [2005]	$I_e = \frac{I_{cr}}{1 - \left(1 - \frac{I_{cr}}{I_g}\right) \left(\frac{M_{cr}}{M_a}\right)^2}$	(6.9)
ISIS Canada	$I_e = \frac{I_g I_{cr}}{I_{cr} + \left[1 - 0.5 \left(\frac{M_{cr}}{M_a}\right)^2\right] (I_g - I_{cr})}$	(6.10)
<p>I_{cr}= moment of inertia of the fully cracked transformed section I_g= moment of inertia of the gross cross section M_{cr}= cracking moment M_a = applied moment at the critical section E_f = the elastic modulus of the FRP bars E_s = the elastic modulus of the reinforcing steel bars ρ_f = the reinforcement ratio ρ_{fb} = the balanced reinforcement ratio</p>		

As concluded in Chapter 4, the bond characteristics of titanium bars are indistinguishable to those for steel, however the modulus is approximately half that of steel. Depending on the design philosophy selected, this will impact both reinforcing ratio, ρ , and I_g/I_{cr} and therefore the calculation of effective moment of inertia. This will be discussed in Section 6.1.3.3.

6.1 DESIGN WITH TITANIUM REINFORCING BARS

As shown in Chapter 3, the stress-strain and other fundamental material behaviors of titanium are similar in form to those of steel. Like steel, titanium exhibits an elastic behavior to a proportional limit, a definable yield value followed by some degree of strain hardening and exhibits a great deal of ductility. Recognizing that titanium reinforcement has about one half the modulus of steel and twice the strength (Table 3.1), to use titanium with the same efficiency as steel in a strength-based design [ACI 318-14] requires tension strains approximately four times greater than in steel-reinforced members. Conversely, titanium has comparable strength and twice the modulus of GFRP bars; coupled with its elastic-plastic stress-strain behavior, titanium may be able to be used very efficiently in a design paradigm such as that used for GFRP-reinforced concrete [440.1R-15]. In either case, the low modulus and therefore high strains needed to engage the material will likely drive issues of serviceability such as cracking and deflections.

6.1.1 Design with Titanium

In terms of both strength and serviceability, steel reinforced concrete design contains a number of empirical and semi-empirical requirements. In many respects, ACI 318-14 is ‘calibrated’ for the use of steel reinforcement having a yield strength of between 275 and 550 MPa (40 and 80 ksi). Because all steel has essentially the same modulus, the modulus of steel, $E_s = 200$ GPa (29,000 ksi) is implicit in many design requirements. As a result, some strain-dependent design equations adopt reinforcing bar stress since this value is more ‘familiar’ to the designer.

The fundamental difference between titanium and steel reinforcement is that the modulus of titanium is approximately one half that of steel. For ease of discussion, the values of modulus and strength given in Table 6.3 will be adopted throughout this chapter. These result in modular ratios of steel : titanium : GFRP = 1 : 0.64 : 0.13 and strength ratios of 1 : 2.33 : 1.33. Although when considering strength, steel and titanium both exhibit elastic-plastic behavior while GFRP is linear to failure. Thus, the GFRP strength must be reduced. A more realistic usable strength ratio for design is steel : titanium : GFRP = 1 : 2.33 : 1.

Table 6.3 Reinforcing bar properties used in benchmark designs

property	Steel	Titanium	GFRP
modulus	$E_s = 200$ GPa	$E_{Ti} = 114$ GPa	$E_f = 41.4$ GPa
yield strength	$f_{sy} = 414$ MPa	$f_{Tiy} = 965$ MPa	-
tensile strength	$f_{su} > 586$ MPa	$f_{Tiu} = 1100$ MPa	$f_{fu} = 552$ MPa
elongation at rupture	$\epsilon_{su} > 0.150$	$\epsilon_{Tiu} > 0.100$	$\epsilon_{fu} = 0.013$
density	7900 kg/m ³	4430 kg/m ³	1200-2100 kg/m ³
1 MPa = 0.145 ksi			

6.1.2 Design for Flexural Strength

In conventional reinforced concrete design, flexural members are ‘under reinforced’ such that the reinforcing steel yields prior to concrete crushing. This ensures a ductile member response. Simultaneously satisfying equilibrium and strain compatibility requires providing a force in the tension reinforcing element, T , at a strain that is ultimately limited by concrete crushing strains. The force in the reinforcing element is conventionally given as the product of reinforcing bar area and stress in the bar, $T = A \times f$. While correct, this is more correctly written $T = A \times \epsilon E$ where the stress in the bar is in fact the product of bar strain and modulus. Therefore, to achieve comparable strength designs in steel and titanium, approximately twice the area of titanium is required. Alternatively, larger strains may be developed to achieve a comparable bar force; this leads to considerations of serviceability and perhaps, as discussed in Chapter 4.4, development of such bars.

6.1.2.1 Material Resistance Factors, ϕ

Recognizing that ϕ relates to the ductility inherent in a member and particularly the ability of statically indeterminate structures to redistribute moment, titanium reinforcement poses a problem. The yield strain of titanium is on the order of $\epsilon_y = 0.0085$, approximately four times that of mild steel. Applying similar ϕ -factors as shown in Table 4.1 results in a strength design ϕ ranging from $\phi = 0.65$ at $\epsilon_t = \epsilon_y$ to $\phi = 0.90$ at values approaching $\epsilon_t = 0.02$. Such strains are typically impractical, resulting in curvature, crack widths and deflections at least four times greater than conventional steel reinforced concrete. Additionally, such large curvature places greater demand on bar bond and may reasonably be expected to result in excessive slip. As a

result, such large strains may not even be attainable. From the perspective of structural performance, bar strains for titanium bars will likely need to remain below yield, resulting in over-reinforced sections and the use of $\phi = 0.65$.

6.1.3 Design for Serviceability

Serviceability of concrete is typically considered in terms of crack control and deflections. Both are affected by the axial stiffness (AE) of the reinforcing material and the bond characteristics of the bar. Assuming concrete is cracked, crack width, and therefore curvature and deflection, is a function of the axial stiffness of the reinforcing bar bridging the crack. Once again, bar area must be increased based on the modular ratio in order to achieve comparable crack control (i.e., limiting strain across cracks).

It is informative to consider the case of GFRP-reinforced concrete [ACI 440.1R-15]. High quality GFRP bars have a modular ratio E_{GFRP}/E_{steel} on the order of 0.20. Design of such members is most often governed by serviceability considerations. Furthermore, to result in 'practical' designs, serviceability requirements for GFRP-reinforced concrete are often relaxed from those for steel-reinforced concrete. In particular, achieving acceptable crack control in GFRP-reinforced members often requires more reinforcement than is required for strength and involves an iterative design step involving the selection of a maximum acceptable crack width (see Eq. 6.12, below).

6.1.3.1 Minimum Reinforcement Requirements and Crack Control

Minimum reinforcement is required for reinforced concrete members to ensure that they do not fail in a brittle manner immediately upon cracking. Conceptually, in steel reinforced concrete, we design to ensure that the nominal moment capacity exceeds 120% of the cracking capacity: $M_n \geq 1.2M_{cr}$ [ACI 318-14]. Additionally, minimum reinforcement is intended to provide crack control; that is, once a section is cracked, there is sufficient reinforcement to permit the development of additional (secondary, tertiary, etc.) cracks rather than all deformation being concentrated at a single primary crack. For steel-reinforced concrete, adequate crack control is achieved providing a reinforcing ratio of least 0.33% [ACI 318-14]. Based on a typical modular ratio, this implies approximately 0.60% bonded titanium reinforcement is required to provide a similar level of crack control. The 0.33% steel requirement implicitly assumes the use of deformed reinforcing bars having consistent bond characteristics equivalent to those achieved by meeting the deformation requirements of ASTM A615. Bars having poorer bond will exhibit greater slip and therefore larger crack widths. In such a case, more bar area is required to achieve the same level of crack control. The corollary is that bars exhibiting better bond characteristics, such as sand-coated GFRP, may improve crack control despite lower bar moduli.

A second means of crack control is given in the form of maximum permitted bar spacing, s_{max} . Both ACI 318-14 and 440.1R-15 prescribe adaptations of Frosch's equation for maximum bar spacing at the tension face of a member. In ACI 318-14 (Eq. 6.11), the maximum bar spacing is calibrated for a maximum crack width of $w = 0.018$ in. In the ACI 440.1R-15 approach (Eq. 6.12), the maximum crack width may be selected based on serviceability or durability considerations. Equations 6.11 and 6.12 are identical for steel reinforcement and $w = 0.018$ in.

Given the lower modulus and potential for permitting larger cracks, Equation 6.12 can be adopted for titanium reinforcement.

$$s_{max} = 380 \left(\frac{276}{f_s} \right) - 2.5c_c \leq 305 \left(\frac{276}{f_s} \right) \quad (6.11: \text{SI units})$$

$$s_{max} = 15 \left(\frac{40,000}{f_s} \right) - 2.5c_c \leq 12 \left(\frac{40,000}{f_s} \right) \quad (6.11: \text{US units})$$

$$s_{max} = 29 \frac{E_f w}{f_{fs} k_b} - 2.5c_c \leq 23 \frac{E_f w}{f_{fs} k_b} \quad (6.12: \text{SI units})$$

$$s_{max} = 1.15 \frac{E_f w}{f_{fs} k_b} - 2.5c_c \leq 0.92 \frac{E_f w}{f_{fs} k_b} \quad (6.12: \text{US units})$$

$$\text{where } d_c \leq \frac{E_f w}{2f_{fs} \beta k_b} \quad (6.13)$$

Where c_c = concrete clear cover

f_s = stress in extreme tension steel at service load (may be taken as $f_s = 0.66f_y$)

f_{fs} = stress in extreme tension GFRP at service load

w = maximum allowable crack width

k_b = bond dependent coefficient; $k_b = 1$ for bars having bond characteristics similar to steel reinforcing bars. $k_b < 1$ for bars having superior bond and $k_b > 1$ for bars having poor bond.

E_f = the elastic modulus of the FRP bars

d_c = thickness of concrete cover measured from extreme tension fiber to center of nearest bar

β = ratio of distance from neutral axis to extreme tension fiber to distance from neutral axis to center of tension reinforcement.

Finally, slabs require minimum reinforcement to resist the effects of temperature and shrinkage. This requirement, is also based on providing a minimum reinforcing bar stiffness to control temperature and shrinkage cracks. The requirement is effectively identical in both ACI 318-14 and 440.1R-15. The latter requirement is given in Eq. 6.14 and can be adopted for titanium reinforcement.

$$\rho_{min,TS} = 0.0018 \left(\frac{414}{f_{fu}} \right) \left(\frac{E_s}{E_f} \right) \geq 0.0014 \quad (6.14: \text{SI units})$$

$$\rho_{min,TS} = 0.0018 \left(\frac{60,000}{f_{fu}} \right) \left(\frac{E_s}{E_f} \right) \geq 0.0014 \quad (6.14: \text{US units})$$

6.1.3.2 Minimum Depth Recommendations

ACI 318 addresses deflections in a prescriptive manner: prescribing a minimum member depth based on span length. Provided the member is deeper than this minimum, relatively complex deflection checks are not necessary. That is, the section is ‘deemed’ to meet deflection criteria. Such minimum depths are tabulated in ACI 318-14 for members having steel reinforcement with $f_y \leq 414$ MPa (60 ksi). ACI 318-14 requires an adjustment for steel yield strengths greater than 414 MPa equal to a 10% increase in minimum depth per 69 MPa (10 ksi) greater than 414 MPa. This requirement is premised on the fact that developing the bar yield strength results in greater strains. So that curvature is not affected, a deeper member is required when developing higher stress (and strains) in the tension reinforcement. Following this argument – the need to restrict curvature – minimum depth recommendations should be further modified by the modular ratio $E_{steel}/E_{titanium}$ in order that the curvature limitation be respected. Clearly, this could result in impractical members two to four times as deep as those required for steel reinforced concrete.

Therefore, practical titanium reinforced members will require their deflections checked as described in Section 6.1.3.3.

ACI 440.1R-15 also provides prescribed member thicknesses above which deflections do not need to be checked. Due to the range of GFRP materials available, ACI 440.1R Eq. 7.3.2.1 provides an alternate basis for selecting a minimum slab thickness. When applied to titanium material properties, ACI 440.1R Eq. 7.3.2.1 also results in impractically deep sections; once again indicating that practical titanium reinforced members will require their deflections to be calculated, rather than being ‘deemed to comply’ as a result of exceeding a minimum depth requirement.

6.1.3.3 Calculations of Deflections

Deflections of cracked concrete members require the calculation of an effective moment of inertia, I_e which falls between the uncracked, gross moment of inertia, I_g of the section and the ‘fully cracked’ or minimum moment of inertia, I_{cr} . The calculated effective properties are treated as being equivalent to elastic properties allowing deflections to be calculated assuming an elastic flexural stiffness $I_e E_c$.

The value of I_e is given by ACI 318-14 as Branson’s equation (Eq. 6.15) and ACI 440.1R-15 uses a version of Bischoff’s equation (Eq. 6.16). Both yield very similar results for steel-reinforced concrete having a primary reinforcing ratio ($\rho = A_s/A_g$) between about 1 and 2%. Branson’s equation, however, is known to be a poor estimator, particularly for members having proportionally smaller effective reinforcing ratios ($E_f A_f/E_s A_g$) as is the case, for instance, for GFRP [Bischoff 2005 and Gilbert 2006]. Because titanium reinforced concrete is likely to have

effective reinforcing ratios differing from those of steel reinforced concrete the use of Eq. 6.16 is appropriate.

$$I_e = \left(\frac{M_{cr}}{M_a}\right)^3 I_g + \left[1 - \left(\frac{M_{cr}}{M_a}\right)^3\right] I_{cr} \leq I_g \quad (6.15)$$

$$I_e = \frac{I_{cr}}{1 - \left(1.72 - 0.72\left(\frac{M_{cr}}{M_a}\right)\right)\left(\frac{M_{cr}}{M_a}\right)^2 \left[1 - \frac{I_{cr}}{I_g}\right]} \leq I_g \quad (6.16)$$

Where:

M_a = applied moment at critical section; note that $M_a > M_{cr}$

M_{cr} = cracking moment of section: $M_{cr} = 0.62\sqrt{f'_c} I_g / y_t$ (SI units; $M_{cr} = 7.5\sqrt{f'_c} I_g / y_t$ in US units)

y_t = distance from neutral axis of gross section to extreme tension fiber of section

I_g = moment of inertia of gross concrete cross section

I_{cr} = moment of inertia of fully cracked transformed cross section; calculations for

I_{cr} for common section shapes are given in ACI HB-10 (11) and can be found in most reinforced concrete textbooks.

6.2 BENCHMARK DESIGN EXAMPLES

Established benchmark flexural design examples of steel-reinforced concrete and GFRP-reinforced concrete have been selected based, in part, on those reported in ACI SP-17 (based on ACI 318-14) and 440.1R-15. Each benchmark design was redesigned using steel, titanium and GFRP. The resulting set of benchmarks can then be compared for expected performance, constructability, and, to a limited extent, cost. All examples use the reinforcing bar properties given in Table 6.3 and assume the use of normal weight (2400 kg/m^3 (150 pcf)) concrete having a design compressive strength $f'_c = 34.5 \text{ MPa}$ (5000 psi) and modulus $E_c = 27.8 \text{ GPa}$ (4030 ksi).

To simplify gravity load design, only the ASCE 7-10 gravity load case, $1.2DL + 1.6LL$, is considered for the ultimate limit state design. Deflections are calculated assuming nominal loads, $DL + LL$.

6.2.1 One-way Slab Design

The reinforcement necessary to resist the negative moment at the face of the first interior span of a continuous slab is designed. The span length is 4.27 m (14 ft) and clear cover is assumed to be 19 mm (0.75 in.) for all cases. The simplified analysis method of ACI 318-14 §6.5 is used to determine design forces. Nominal applied loads are assumed to be the member self-weight (DL), 0.72 kPa (15 psf) superimposed dead load (DL), and 4.8 kPa (100 psf) live load (LL). This example is based on one presented in ACI SP-17.

6.2.1.1 Slab Design 1

Slab design 1 is shown in Table 6.4. The slab depth of the steel-reinforced concrete slab is selected so that deflection calculations may be neglected (it is seen upon calculation that the uncracked steel-reinforced slab has a predicted deflection of only $L/3200$). The titanium- and GFRP-reinforced slab depths were selected to be the same as the steel-reinforced slab. Each slab design was controlled by minimum reinforcement and remained uncracked.

6.2.1.2 Slab Design 2

Slab design 2 is shown in Table 6.5. These slabs were thinner than slab design 1. All slabs exhibit cracked behavior although deflections were generally acceptable. For the steel- and

titanium-reinforced slabs, the selection of reinforcing was controlled by the strength required. The GFRP-reinforced slab continued to be governed by the minimum reinforcement requirement.

6.2.1.3 Discussion of One-way Slab Designs

Slab design, in general, is governed by serviceability and crack control requirements. This is evident in design 1 (Table 6.4), in which conventional slab depths are selected and designs controlled by minimum reinforcement requirements. Thinner slabs (Table 6.5) are relatively easily designed to satisfy both strength and deflection criteria. Two issues become apparent when using titanium reinforcing bars:

- 1) For cracked members (Table 6.5), in order to satisfy reasonable crack control requirements, a larger number of smaller titanium bars is necessary.
- 2) Despite 1), crack widths and deflections in titanium-reinforced slabs are expected to be greater than those in steel-reinforced slabs.

In the 100 mm (4 in.) thick slab examples shown in Table 6.5, the steel reinforced example requires #4 bars spaced at 230 mm (9 in.) ($\rho = 0.0074$) to satisfy reinforcement ($\rho_{req} = 0.0072$) and maximum spacing requirements ($s_{max} = 290$ mm (11.5 in.)). In this case the maximum spacing requirements are calibrated based on a crack width of $w = 0.46$ mm (0.018 in.) The calculated cracked section deflections remain below the conventionally accepted limits of $L/240$ for DL + LL, and $L/360$ for LL only [ASCE 7-10]. The titanium-reinforced example requires #3 bars at 102 mm (4 in.) ($\rho = 0.0092$), almost twice the reinforcement required for strength alone ($\rho_{req} = 0.0044$), in order to provide a reasonable level of crack control. Nonetheless, the anticipated crack widths based on the 102 mm bar spacing will likely exceed w

= 0.76 mm (0.03 in.), twice that expected for the steel-reinforced case. Finally, deflections of the titanium-reinforced case will be 40% greater than the steel-reinforced case, although still generally within accepted limits. In order to achieve behavior of the GFRP example, the slab depth must be increased 150% to 153 mm (6 in.) and, still, the calibrated crack width will be close to $w = 1$ mm (0.04 in.).

Table 6.4 Comparable designs for one-way slab 1 (Section 6.2.1.1)

	A615 Steel	Titanium	GFRP
design by...	ACI 318-14	this paper	ACI 440.1R-15
minimum thickness not requiring explicit deflection calculation	ACI 318 7.3.1.1 $h > L/24$	see text of paper	ACI 440.1R 7.3.2.1 $h > L/17$
select slab depth	$h = 178$ mm	$h = 178$ mm	$h = 178$ mm
slab self weight	4.2 kPa	4.2 kPa	4.2 kPa
negative moment at first interior support $M_u = wL^2/14$	17.8 kNm/m	17.8 kNm/m	17.8 kNm/m
shear at first interior support $V_u = 1.15wL/2$	33.5 kN/m	33.5 kN/m	33.5 kN/m
shear check, $\phi V_c = 0.75 \times 0.17\sqrt{f'_c}db$	111 kN/m OK	111 kN/m OK	111 kN/m OK
assumed material resistance factor	$\phi = 0.90$	$\phi = 0.65$	$\phi = 0.65$ ($\rho \geq 1.4\rho_{fb}$)
reinforcement required for strength	$\rho = (0.85f'_c/f_y)(1 - (1 - 2R_u/0.85f'_c)^{1/2})$ $R_u = M_u/\phi bd^2$		$\rho_{fb} = 0.85\beta_1(f'_c/f_{fu})(E_f E_{cu}/(E_f E_{cu} + f_{fu})) = 0.0078$
	$\rho = 0.0021$	$\rho = 0.0012$	$\rho = 1.5\rho_{fb} = 0.0120$
			$f_f = 434$ MPa
			$\phi M_n = 71.5$ kNm
			redesign using ρ_{min} (below)
			$\phi = 0.55$ ($\rho < \rho_{fb}$) $\phi M_n = 28.2$ kNm
minimum reinforcement required	$(E_t/E_s)\rho_{min} = 0.25\sqrt{f'_c}/f_y \geq 1.38/f_y$		$\rho_{min} = 0.41\sqrt{f'_c}/f_{fu} \geq 2.28/f_{fu}$
temperature and shrinkage reinforcement	$\rho_{min} = 0.0035$	$\rho_{min} = 0.0026$	$\rho_{min} = 0.0043$
	$(E_t/E_s)\rho_{min TS} = 0.0018(414/f_y) \geq 0.0014$		
	$\rho_{min TS} = 0.0018$	$\rho_{min TS} = 0.0014$	$\rho_{min TS} = 0.0014$
maximum bar spacing	Eq. 1	Eq. 2	
	$f_s \approx 0.43f_y$ $s_{max} = 458$ mm ($w = 0.46$ mm)	$f_s \approx 0.33f_y$ $s_{max} = 127$ mm ($w = 0.46$ mm) $s_{max} = 254$ mm ($w = 0.71$ mm) $s_{max} = 356$ mm ($w = 0.96$ mm) $s_{max} = 458$ mm. ($w = 1.22$ mm)	$f_s \approx 0.45f_y$ $s_{max} = 41$ mm ($w = 0.46$ mm) $s_{max} = 89$ mm ($w = 0.71$ mm) $s_{max} = 137$ mm ($w = 0.96$ mm) $s_{max} = 185$ mm. ($w = 1.22$ mm)
reinforcement required	#3 @ 127 mm or #4 @ 240 mm	#3 @ 178 mm or #4 @ 305 mm	#3 @ 102 mm or #4 @ 190 mm
verify ϵ_t	$\epsilon_t = 0.043 \gg 0.005 \rightarrow \phi = 0.90$	#3 bars: $\epsilon_t > 0.02$ for $s > 152$ #4 bars: $\epsilon_t > 0.02$ for $s > 280$ $\rightarrow \phi = 0.90$	due to low applied load, tension control design is not penalising in this instance
final design	#4 @ 240 mm	#4 @ 300 mm	#3 @ 100 mm
deflection check			
M_{cr}	19.3 kNm/m $< M_u$	19.3 kNm/m $< M_u$	19.3 kNm/m $< M_u$
	section remains uncracked; $I_e = I_g$		
I_g	143 x 10 ⁶ mm ⁴	143 x 10 ⁶ mm ⁴	143 x 10 ⁶ mm ⁴
$\Delta \approx \rho L^4/185E_c I_g$ (LL only)	L/6472	L/6472	L/6472
$\Delta \approx \rho L^4/185E_c I_g$ (DL + LL)	L/3200	L/3200	L/3200

1 MPa = 0.145 ksi; 1 mm = 0.039 in.; 1 m = 39.4 in.; 1 kN = 225 lb; 1kNm = 8.85 kip-in

Table 6.5 Comparable designs for one-way slab 2 (Section 6.2.1.2)

	A615 Steel	Titanium	GFRP
design by...	ACI 318-14	this paper	ACI 440.1R-15
minimum thickness not requiring explicit deflection calculation	ACI 318 7.3.1.1 $h > L/24$	see paper text	ACI 440.1R 7.3.2.1 $h > L/17$
select slab depth	$h = 102$ mm	$h = 102$ mm	$h = 153$ mm
slab self weight	2.4 kPa	2.4 kPa	3.6 kPa
negative moment at first interior support $M_u = wL^2/14$	14.8 kNm/m	14.8 kNm/m	16.7 kNm/m
shear at first interior support $V_u = 1.15wL/2$	27.7 kN/m	27.7 kN/m	32.1 kN/m
shear check, $\phi V_c = 0.75 \times 2\sqrt{f'_c} db$	55.4 kN/m OK	55.4 kN/m OK	89.0 kN/m OK
assumed material resistance factor	$\phi = 0.90$	$\phi = 0.65$	$\phi = 0.65$ ($\rho \geq \rho_{fb}$)
reinforcement required for strength	$\rho = (0.85f'_c/f_y)(1 - (1 - 2R_u/0.85f'_c)^{1/2})$ $R_u = M_u/\phi bd^2$		$\rho_{fb} = 0.85\beta_1(f'_c/f_{fu})(E_f\epsilon_{cu}/(E_f\epsilon_{cu} + f_{fu})) = 0.0078$
	$\rho = 0.0072$	$\rho = 0.0044$	$\rho_{fb} = 0.0078$ (select 0.008)
			$f_f = 434$ MPa
			$\phi M_n = 49.6$ kNm/m
			redesign using ρ_{min} (below)
minimum reinforcement required	$(E_t/E_s)\rho_{min} = 0.25\sqrt{f'_c}/f_y \geq 1.38/f_y$ $\rho_{min} = 0.0035$		$\rho_{min} = 0.41\sqrt{f'_c}/f_{fu} \geq 2.28/f_{fu}$ $\rho_{min} = 0.0043$
temperature and shrinkage reinforcement	$(E_t/E_s)\rho_{min TS} = 0.0018(414/f_y) \geq 0.0014$		
	$\rho_{min TS} = 0.0018$	$\rho_{min TS} = 0.0014$	$\rho_{min TS} = 0.0014$
maximum bar spacing	Eq. 1	Eq. 2	
	$f_s \approx 0.69f_y$ $s_{max} = 292$ mm ($w = 0.46$ mm)	$f_s \approx 0.69f_y$ $s_{max} = 38$ mm ($w = 0.46$ mm) $s_{max} = 89$ mm ($w = 0.71$ mm) $s_{max} = 140$ mm ($w = 0.96$ mm) $s_{max} = 190$ mm. ($w = 1.22$ mm)	$f_s \approx 0.57f_y$ $s_{max} = 20$ mm ($w = 0.46$ mm) $s_{max} = 61$ mm ($w = 0.71$ mm) $s_{max} = 99$ mm ($w = 0.96$ mm) $s_{max} = 137$ mm. ($w = 1.22$ mm)
reinforcement required	#3 @ 127 mm or #4 @ 229 mm	#3 @ 203 mm or #4 @ 381 mm	#3 @ 127 mm or #4 @ 229 mm
verify ϵ_t	$\epsilon_t = 0.021 \gg 0.005 \rightarrow \phi = 0.90$	#3 bars: $\epsilon_t > 0.02$ for $s > 153$ #4 bars: $\epsilon_t > 0.02$ for $s > 279$ $\rightarrow \phi = 0.90$	due to low applied load, tension control design is not penalising in this instance
final design	#4 @ 230	#3 @ 100	#3 @ 100
deflection check			
M_{cr}	6.3 kNm/m	6.3 kNm/m	14.1 kNm/m
I_g	26.7×10^6 mm ⁴	26.7×10^6 mm ⁴	89.9×10^6 mm ⁴
I_{cr}	7.08×10^6 mm ⁴	7.08×10^6 mm ⁴	4.58×10^6 mm ⁴
I_e	12.1×10^6 mm ⁴ (Eq. 5)	8.74×10^6 mm ⁴ (Eq. 5) 7.91×10^6 mm ⁴ (Eq. 6)	16.2×10^6 mm ⁴ (Eq. 5)
$\Delta \approx pL^4/185E_cI_g$ (LL only)	L/551	L/395 or L/352	L/737
$\Delta \approx pL^4/185E_cI_g$ (DL + LL)	L/334	L/239 or L/213	L/388

1 MPa = 0.145 ksi; 1 mm = 0.039 in.; 1 m = 39.4 in.; 1 kN = 225 lb; 1kNm = 8.85 kip-in

6.2.2 Simple Flexural Beam Design

This design is based on Example 3 of ACI 440.1R-15. Design a singularly reinforced rectangular beam having a width, $b = 305$ mm (12 in.) to resist service load moments $M_{DL} = 76$ kNm (56 kip-ft = 672 kip-in.) and $M_{LL} = 47.5$ kNm (35 kip-ft = 420 kip-in.). Thus, the design moment is $1.2DL + 1.6LL = 167$ kNm (1478 kip-in.) and the service moment is 123.5 kNm (1092 kip-in.). The resulting designs are shown in Table 6.6.

The steel-reinforced example proceeds by selecting a reinforcing ratio, ρ less than the ratio corresponding to a steel strain, $\varepsilon_t = 0.005$. In this way, the beam is tension controlled and $\phi = 0.90$. The design is carried out accordingly and the capacity verified. The GFRP case proceeds similarly with the reinforcing ratio being selected so that the beam is compression controlled and $\phi = 0.65$. The first titanium case (design 1 in Table 6.6) is carried out based on the strength design approach of ACI 318 with a tension-controlled design resulting. As described in Section 6.1.2.1, a titanium strain of 0.02 is required to ensure tension-controlled behavior. This results in a very low reinforcing ratio, $\rho = 0.004$. Based on the discussion presented in Section 4.4, it is not clear how such bars would be developed.

When comparing the first three comparable designs in terms of serviceability, as expected the GFRP-reinforced beam has an effective cracked stiffness, I_e , approximately one third that of the steel-reinforced case. Expected crack widths, based on the crack control provided are also about three times greater than for the steel-reinforced case. The titanium design 1 case, also exhibits a very low cracked stiffness (also about one third that of the steel-reinforced section) and less effective crack control (cracks about twice the width of comparable steel-

reinforced design). Indeed, the titanium design 1 case performs very similarly to the GFRP-reinforced case.

Titanium design 2 was selected to achieve service performance more comparable to that of the steel-reinforced case. Knowing the design for the steel-reinforced case, the reinforcing ratio for the titanium case was selected to be approximately $\rho_{Ti} = \rho_s(E_s/E_{Ti})$ and the section dimensions were selected to be the same ($h \times b = 508 \times 305$ mm (20 x 12 in.)). As seen in Table 6.6, this results in a very over-reinforced section in which the titanium does not yield at the ultimate limit state. Indeed, in design 2, the titanium only reaches a stress $f_{Ti} = 600$ MPa (87 ksi), only 62% of yield; thus, the material is not being used efficiently and $\phi = 0.65$. The resulting effective cracked stiffness is however comparable to that of the steel-reinforced case and the crack control is only marginally less effective.

Table 6.6 Comparable designs for rectangular beam (Section 6.2.2)

	A615 Steel	Titanium		GFRP
design by...	ACI 318-14	this report		ACI 440.1R-15
design basis	tension-controlled	<i>design 1:</i> tension controlled based on strength	<i>design 2:</i> achieve stiffness comparable to ACI 318	compression controlled
select target reinforcing ratio	for $\epsilon_t \geq 0.005$ $\rho \leq \rho_t = 0.319\beta_1 f_c' / f_y$ = 0.0213	for $\epsilon_t = 0.02$ $\rho \leq \rho_t = 0.13\beta_1 f_c' / f_y$ = 0.004	select ρ for stiffness comparable to ACI 318	$\rho_{fb} = 0.85\beta_1(f_c' / f_{fu})$ $(E_f E_{cu} / (E_f E_{cu} + f_{fu}))$ = 0.0078
select ρ	$\rho = 0.010$ (typical value)	$\rho = 0.004$	$\rho = 0.015$	$\rho = 1.5\rho_{fb} = 0.012$ (typical initial design)
determine bd^2	-	-	-	$f_j = 448$ MPa
	$\rho = (0.85f_c' / f_y)(1 - (1 - 2R_n / 0.85f_c')^{1/2})$ in which $R_n = M_u / \phi b d^2$			
select d	$db^2 = 48.3 \times 10^6$ mm ³ $d = 399$ mm	$db^2 = 48.3 \times 10^6$ mm ³ $d = 411$ mm	select h for stiffness comparable to ACI 318	$db^2 = 52.6 \times 10^6$ mm ³ $d = 417$ mm
select h	$h = 508$ mm	$h = 508$ mm	$h = 508$ mm	$h = 508$ mm
select $A_{req} = \rho b d$	$A_{req} = 1213$ mm ²	$A_{req} = 503$ mm ²	$A_{req} \approx 2032$ mm ²	$A_{req} = 1523$ mm ²
	select 3 #7 bars ($A_s = 1161$ mm ²)	select 4 #4 bars ($A_s = 516$ mm ²)	select 4 #8 bars ($A_s = 2039$ mm ²)	select 3 #8 bars ($A_s = 1529$ mm ²)
determine d (assume 1.5 in. cover; #4 ties)	$d = 447$ mm	$d = 452$ mm	$d = 445$ mm	$d = 445$ mm
verify design (A_{prov}/bd)	$\rho = 0.008$	$\rho = 0.0037$	$\rho = 0.015$ over reinforced	$\rho = 0.011 = 1.45\rho_{fb}$
material resistance factor	$\phi = 0.90$ ($\rho \leq \rho_t$)	$\phi = 0.90$ ($\rho \leq \rho_t$)	$\phi = 0.65$	$\phi = 0.65$ ($\rho \geq 1.4\rho_{fb}$)
stress in bars	$f_s = f_y = 414$ MPa	$f_{Ti} = f_y = 965$ MPa ¹	$f_{Ti} = 600$ MPa	$f_j = 469$ MPa
moment capacity	$\phi M_n = 171 > 167$ kNm	$\phi M_n = 198 > 167$ kNm	$\phi M_n = 298 > 167$ kNm	$\phi M_n = 184 > 167$ kNm
ρ_{min}	$\rho_{min} = 0.0035 < \rho$	$\rho_{min} = 0.0026 < \rho$		$\rho_{min} = 0.0043 < \rho$
bar spacing	$s = 89$ mm	$s = 64$ mm	$s = 58$ mm	$s = 89$ mm
resulting implied crack width	$w < 0.46$ mm ($s_{max} = 286$ mm)	$w = 0.86$ mm	$w = 0.53$ mm	$w = 1.32$ mm
deflection check				
M_{cr}	47.9 kNm	47.9 kNm	47.9 kNm	47.9 kNm
I_g	3330×10^6 mm ⁴	3330×10^6 mm ⁴	3330×10^6 mm ⁴	3330×10^6 mm ⁴
I_{cr}	1096×10^6 mm ⁴	348×10^6 mm ⁴	1124×10^6 mm ⁴	358×10^6 mm ⁴
I_e	1227×10^6 mm ⁴ (Eq. 5)	523×10^6 mm ⁴ (Eq. 5) 372×10^6 mm ⁴ (Eq. 6)	1253×10^6 mm ⁴ (Eq. 5) 1181×10^6 mm ⁴ (Eq. 6)	383×10^6 mm ⁴ (Eq. 6)

1 MPa = 0.145 ksi; 1 mm = 0.039 in.; 1 m = 39.4 in.; 1 kN = 225 lb; 1kNm = 8.85 kip-in

¹ See Section 4.4; provision for developing this bar stress is uncertain

6.2.3 Repair/ Retrofit Examples

Established benchmark near-surface mounted (NSM) retrofit design examples have been selected from those reported in ACI 440.2R-17. Each benchmark design was redesigned using titanium bars having the properties given in Table 6.3 and assumes the use of normal weight (2400 kg/m^3 (150 pcf)) concrete having a design compressive strength $f_c' = 34.5 \text{ MPa}$ (5000 psi) and modulus $E_c = 27.8 \text{ GPa}$ (4030 ksi).

6.2.3.1 NSM Retrofit of Simple Span Beam

This example is based on Examples 16.3 and 16.4 in ACI 440.2R-17. A singly-reinforced simply supported $610 \times 305 \text{ mm}$ (24 x 12 in.) steel-reinforced concrete beam having three #9 bars ($d = 546 \text{ mm}$ (21.5 in.)) is located in an unoccupied warehouse and is subjected to a 50 percent increase in its live-load-carrying requirements – from 17.5 kN/m to 26.3 kN/m (1.2 kip/ft to 1.8 kip/ft). An analysis of the existing beam indicates that the beam retains sufficient shear strength to resist the new required shear strength and meets deflection and crack-control serviceability requirements. Its flexural strength, however, is inadequate to carry the increased live load. By inspection, the degree of strengthening is reasonable in that it meets the strengthening limit criteria specified in ACI 440.2R-17 Eq. 9.2. That is, the existing moment capacity without FRP, $(\phi M_n)_{w/o} = 361 \text{ kNm}$ (266 kip-ft), is greater than the unstrengthened moment limit, $(1.1M_{DL} + 0.75M_{LL})_{\text{new}} = 240 \text{ kNm}$ (177 kip-ft). The flexural retrofit design is summarized in Table 6.6.

The approach to retrofit design is that laid out in ACI 440.2R-17. This is an iterative approach in which a retrofit detail is selected, and the capacity of the retrofit section is determined. In the case shown, 2 #3 CFRP or titanium bars are selected. The similarity in

properties of the CFRP bars ($E_f = 133 \text{ GPa}$ (19230 ksi) and $f_{fu} = 1724 \text{ MPa}$ (250 ksi)) and those of the titanium ($E_{Ti} = 114 \text{ MPa}$ (16500 ksi) and $f_{yTi} = 965 \text{ MPa}$ (140 ksi)) result in very similar designs. The maximum allowable usable strain in the CFRP is $\kappa_m C_E \varepsilon_{fu} = 0.7 \times 0.95 \times 1724/133,00 = 0.0086$, while the yield strain of the titanium is $965/114,000 = 0.0085$.

Two titanium NSM designs are presented. The key differences are highlighted in the shaded cells of Table 6.7. In the first design, the titanium bar is assumed to be bonded into the NSM slots with no additional anchorage. In such a case, the NSM performance is a function of the substrate, concrete-NSM embedding material, and NSM material system. ACI 440.2R-17 recommends a ‘bond factor’, $\kappa_m = 0.7$, which limits the strain that may be achieved by the GFRP based on a debonding mode of failure. In the titanium example, the titanium response is limited to its elastic region (i.e., $\varepsilon_{Ti} \leq \varepsilon_{yTi}$). There is no known evidence that bonded NSM systems are able to develop plastic behavior in their embedded bars. Nonetheless, the elastic-plastic nature of titanium means no reduction in allowable strain is required.

In the second titanium case, mechanical anchorage of the titanium using 90-degree hooked anchorages into the core of the concrete section are assumed (as described in Chapter 5). In such a case, provided deformed bars are used, bond is the primary means of stress transfer at service levels but is not strictly required at ultimate capacity; the titanium can therefore be permitted to develop its plastic behavior. Additionally, the contribution of the NSM to the moment capacity does not need to be reduced by $\Psi_f = 0.85$ as in the bonded cases.

In comparing the solutions, the stress in the existing reinforcing steel at service loads are slightly greater and those in the NSM reinforcement are slightly lower in the titanium cases than in the CFRP cases; this reflects the difference in modulus of the materials. The strain in the

existing reinforcement (ϵ_s) at the ultimate capacity also remains well below values in which rupture is considered a concern.

There remains no agreed upon procedure for calculation deflections of externally retrofit concrete members. Nonetheless, curvature is a surrogate for deflection. Due to the similar behavior of the bonded CFRP and titanium cases, the curvature at the design section is the same (marginally lower in the titanium case due to the marginally lower limiting NSM strain). The second titanium case, in which the NSM titanium exceeds its elastic limit ($\epsilon_{NSM} = 0.0113 > \epsilon_{yTi} = 0.0085$) exhibits approximately 30% greater maximum curvature which would also be reflected in deflections. It must be noted that this example assumes effective bond at service level stresses between the points of anchorage; otherwise an unbonded reinforcing case should be considered.

Table 6.7 (part 1) Comparable NSM designs for rectangular beam retrofit (Section 6.2.3.1)

	existing beam
beam dimensions	$h \times b = 610 \times 305$ mm; $d = 546$ mm; $d_{NSM} = 602$ mm
reinforcing steel	3 #29 ($A_s = 1935$ mm ²)
existing moments	$M_{service} = M_{DL} + M_{LL} = 97.6 + 116.6 = 214$ kNm $M_u = 1.2M_{DL} + 1.6M_{LL} = 1.2(97.6) + 1.6(116.6) = 304$ kNm
existing capacity	$\phi M_n = \phi A_s f_y (d - 0.59 A_s f_y / b f_c') = 361$ kNm
existing soffit strain at M_{DL}	$\epsilon_{bi} = M_{DL}(d_f - kd) / I_{cr} E_c = 0.0006$ ($kd = 182$ mm and $I_{cr} = 2459 \times 10^6$ mm ⁴ determined from ACI HB 10)

Table 6.7 (part 2) Comparable NSM designs for rectangular beam retrofit (Section 6.2.3.1)

	retrofit beams		
required retrofit capacity	$M_{service} = M_{DL} + M_{LL} = 97.6 + 176.3 = 274 \text{ kNm}$ $M_u = 1.2M_{DL} + 1.6M_{LL} = 1.2(97.6) + 1.6(176.3) = 400 \text{ kNm}$		
	CFRP per ACI 440.2R-17	Ti ($\epsilon_{Ti} \leq \epsilon_{yTi}$)	Ti
NSM area	2 #3 bars: $A_{NSM} = 142 \text{ mm}^2$		
NSM anchorage	bond	bond	90° anchorage
NSM modulus	$E_f = 133 \text{ GPa}$	$E_{Ti} = 114 \text{ GPa}$	
NSM strength	$f_{fu} = 1724 \text{ MPa}$ $C_{E f_{fu}} = 1634 \text{ MPa}$	$f_{yTi} = 965 \text{ MPa}$	
NSM strain	$\epsilon_{fu} = 0.0130$ $C_{E \epsilon_{fu}} = 0.0123$	$\epsilon_{yTi} = 0.0085$	
allowable NSM strain	$\kappa_m C_{E \epsilon_{fu}} = 0.0086$	$\epsilon_{yTi} = 0.0085$	$\epsilon_{uTi} \approx 0.15$
iterative calculation of depth of compression block, c	select trial c effective strain at level of NSM: $\epsilon_{fe} = \epsilon_{cu}((d_{NSM} - c)/c) - \epsilon_{bi} \leq$ allowable NSM strain concrete strain corresponding to ϵ_{fe} : $\epsilon_c = (\epsilon_{fe} - \epsilon_{bi})(c/(d_{NSM} - c))$ steel strain corresponding to ϵ_{fe} : $\epsilon_s = (\epsilon_{fe} - \epsilon_{bi})((d - c)/(d_{NSM} - c))$ stress in steel: $f_s = E_s \epsilon_s \leq f_y$ stress in NSM: $f_{NSM} = E_{NSM} \epsilon_{fe} (\leq f_{NSM}$ for titanium) concrete stress block factors: $\epsilon_c' = 1.7f_c'/E_c$; $\beta_1 = (4\epsilon_c' - \epsilon_c)/(6\epsilon_c' - 2\epsilon_c)$ and $\alpha_1 = (3\epsilon_c' \epsilon_c - \epsilon_c^2)/(3\beta_1 \epsilon_c'^2)$ $c = (A_s f_s + A_{NSM} f_{NSM})/(\alpha_1 f_c' \beta_1 b)$ iterate on selection of c until equilibrium is achieved		
c	133 mm	131 mm	121 mm
ϵ_{fe}	0.0086	0.0085	0.0113
ϵ_s	0.0071	0.0070	0.0094
ϵ_c	-0.0023	-0.0022	-0.0027
f_s	414 MPa	414 MPa	414 MPa
f_{NSM}	1145 MPa	965 MPa	965 MPa
determine moment capacity	contribution from steel: $M_{ns} = A_s f_s (d - \beta_1 c/2)$ contribution from FRP: $M_{nNSM} = A_{NSM} f_{NSM} (d_{NSM} - \beta_1 c/2)$		
M_{ns}	397 kNm	397 kNm	403 kNm
M_{nNSM}	89 kNm	76 kNm	76 kNm
ϕM_n	$\phi(M_{ns} + 0.85M_{nNSM})$ $= 426 \text{ kNm}$	$\phi(M_{ns} + 0.85M_{nNSM})$ $= 416 \text{ kNm}$	$\phi(M_{ns} + M_{nNSM})$ $= 427 \text{ kNm}$
verify service level stresses	$kd = d \times \sqrt{\left(\rho_s \frac{E_s}{E_c} + \rho_{NSM} \frac{E_{NSM}}{E_c}\right)^2 + 2\left(\rho_s \frac{E_s}{E_c} + \rho_{NSM} \frac{E_{NSM}}{E_c} \frac{d_{NSM}}{d}\right) - \left(\rho_s \frac{E_s}{E_c} + \rho_{NSM} \frac{E_{NSM}}{E_c}\right)}$ $f_{ss} = \frac{\left[M_{service} + \epsilon_{bi} A_{NSM} E_{NSM} \left(d_{NSM} - \frac{kd}{3}\right)\right] (d - kd) E_s}{A_s E_s \left(d - \frac{kd}{3}\right) (d - kd) + A_{NSM} E_{NSM} \left(d_{NSM} - \frac{kd}{3}\right) (d_{NSM} - kd)}$ $f_{sNSM} = f_{ss} \frac{E_{NSM} d_{NSM} - kd}{E_s d - kd} - \epsilon_{bi} E_{NSM}$		
kd	192 mm	192 mm	192 mm
f_{ss}	282 MPa < $0.8f_y$	284 MPa < $0.8f_y$	284 MPa < $0.8f_y$
f_{sNSM}	137 MPa < $0.55f_{fu}$	119 MPa	119 MPa
curvature: $(\epsilon_{fe} - \epsilon_c)/d_f$	0.00046/in.	0.00045/in.	0.00059/in.

1 MPa = 0.145 ksi; 1 mm = 0.039 in.; 1 m = 39.4 in.; 1 kN = 225 lb; 1kNm = 8.85 kip-in

6.3 COST COMPARISON

The *perceived* significant cost premium associated with titanium is a barrier that must be overcome. Table 6.8 illustrates a simple comparison of both cost and design paradigm. With the exception of the titanium scenarios reported, the data in this table was prepared for the FHWA (Triantafillou 2012 and subsequently updated by Wong 2014) to compare costs of corrosion-resistant reinforcing bars for concrete bridge decks. The example is based on a prototype 54.9 x 24.4 m (180 x 80 ft) bridge deck having a thickness of 200 mm (8 in.). In this analysis, in-place cost of reinforcement is determined by adding a premium of \$0.40 per kg (\$0.88 per pound) to account for fabrication, transportation and installation. Actual costs fluctuate by size of project, location and market demand. Costs are normalized for the 200 mm thick 1340 m² (14400 ft²) bridge deck considered. The typical bridge construction unit cost for medium span bridges (in 2010) is \$989/m² (\$92/ft²) or \$1.325M for the prototype deck.

As expected, universal use of titanium bars results in a considerable cost premium. However, if designed by strength (rather than the AASHTO prescriptive design), as indicated in the shaded rows in Table 6.8, the premium is minimized. Two cases are shown that range between a cracked slab (Table 6.5) and cracked beam (Table 6.6). The ability to use the titanium bars more efficiently is improved for deeper sections and premiums approaching those already paid for solid stainless-steel bars are achievable. Indeed, the \$44/kg (\$20/lb) assumed price for titanium bars is based on present market prices and demand. If titanium reinforcing bars are adopted, like FRP bars, their price may fall, making them equivalent to stainless steel bars. The example shown in Table 6.8 assumes all steel in the deck is that shown; mixing corrosion

resistant bars in the top mat and black steel in the lower mat reduces the premiums paid considerably.

Finally, it is also noted that while titanium might represent a raw material cost 40 times that of steel, this equates to an in-place reinforcing bar cost about 4 times that of steel and a total cost only 32% greater than a steel-reinforced deck. Long term savings in maintenance for a non-corrosive deck can be leveraged to repay this initial cost premium.

Table 6.8 Cost comparison for typical bridge deck (US units are used for this example since these are native to the primary source material, Triantafillou 2012 and Wong 2014).

	in place unit cost	basis	mean rebar cost	mean bridge deck cost	premium
black steel	1.36 \$/lb	8 lb/ft ²	\$10.84/ft ²	\$90.35/ft ²	control
epoxy-coated steel (green)	1.56 \$/lb	8 lb/ft ²	\$12.44/ft ²	\$91.94/ft ²	+2%
epoxy-coated steel (purple) (2012)	2.04 \$/lb	8 lb/ft ²	\$16.28/ft ²	\$95.76/ft ²	+6%
galvanised steel	1.61 \$/lb	8 lb/ft ²	\$12.84/ft ²	\$92.36/ft ²	+2%
MMFX-2 steel – prescriptive design	1.82 \$/lb	8 lb/ft ²	\$14.52/ft ²	\$94.03/ft ²	+4%
Z-bar (2012)	1.98 \$/lb	8 lb/ft ²	\$15.80/ft ²	\$95.28/ft ²	+5%
solid 2205 stainless steel	3.42 \$/lb	8 lb/ft ²	\$27.32/ft ²	\$106.81/ft ²	+18%
Basalt FRP (BFRP)	2.01 \$/ft	8 ft/ft ²	\$16.04/ft ²	\$95.56/ft ²	+6%
GFRP	1.60 \$/ft	8 ft/ft ²	\$12.76/ft ²	\$92.29/ft ²	+2%
Gr. 5 Ti – AASHTO prescriptive design	\$20/lb	4.5 lb/ft ²	\$90/ft ²	\$169/ft ²	+87%
Gr. 5 Ti – steel equivalent strength (Table 6.5 cracked slab)	\$20/lb	5.7 lb/ft ²	114/ft ²	193/ft ²	+114%
Gr. 5 Ti – steel equivalent strength (Table 6.6 cracked beam)	\$20/lb	2.0 lb/ft ²	\$40/ft ²	\$119/ft ²	+32%
Gr. 5 Ti – steel equivalent stiffness (Table 6.6 cracked beam)	\$20/lb	7.9 lb/ft ²	\$158/ft ²	\$237/ft ²	+162%
1 lb = 0.45 kg; 1 ft ² = 0.093 m ²					

7.0 CONCLUSIONS AND RECOMMENDATIONS

7.1 CONCLUSIONS

The objective of this study was to ascertain the potential applications for 6Al-4V6 titanium (grade 5) reinforcing bar for concrete. Experimental evidence from this study clearly indicates potential for the use of titanium bars in reinforced concrete structures. To determine the overall performance of titanium reinforcing bars, several research programs were carried out. First, a two-year study evaluating the potential for galvanic corrosion to develop between titanium and [co-]existing steel reinforcement was carried out. Following the corrosion study, several research programs were completed to evaluate the geometrical and mechanical properties of the titanium reinforcing bars. Following this, an in-depth laboratory test program evaluated the bond characteristics of the titanium bars. A demonstration of near surface mounted (NSM) titanium bar repair of concrete highway bridge deck slabs was carried out. Finally, the information obtained from these programs was used to examine the implementation of titanium reinforcing bars into existing reinforced concrete design paradigms. The conclusions of each of these phases of this study are reiterated in the following sections.

7.1.1 Galvanic Corrosion Study

The objective of corrosion study was to assess the effects of combining titanium and black steel in typical concrete in which the materials will be effectively electrically coupled. The titanium was alternately 1) embedded in the concrete; 2) ‘potted’ in an epoxy resin prior to embedment in concrete; or 3) ‘potted’ in a cementitious repair mortar prior to embedment in concrete. The potted specimens are intended to better replicate conditions in a repair scenario in which the titanium will be used as NSM reinforcement. In order to place the use of titanium in context, duplicate specimens having stainless steel and CFRP reinforcing bars were also tested.

The comparison of interest in this study was as follows: does the presence of titanium accelerate or result in greater steel corrosion than other materials coupled with mild reinforcing steel; that is, does a galvanic cell develop? For the conditions tested, as expected (and intended), corrosion was present in all specimens. There was no evidence that the presence of 6Al-4V titanium reinforcing bars in close proximity to (or in electrical contact with) A615 steel reinforcing bars results in any change in the rate or nature of corrosion. Interestingly, the use of 2205 duplex stainless-steel bars with A615 steel did exhibit evidence of an active galvanic corrosion effect. Further study of this issue is warranted since stainless steel bars are presently used in some bridge applications in conjunction with black steel bars.

7.1.2 Titanium Bar Geometric and Material Properties

The geometric and experimentally determined material and mechanical properties of 6AL-4V titanium reinforcing bars and comparable properties of A615 steel bars were determined. All bars

are nominally #5 bars. The titanium bars can be fabricated to meet the deformation requirements of ASTM A615. The stress-strain and other fundamental material behaviors of titanium are similar in form to those of steel. Like steel, titanium exhibits an elastic behavior to a proportional limit, a definable yield value followed by some degree of strain hardening and exhibits a great deal of ductility. Titanium reinforcement has about one half the modulus of steel and twice the strength of conventional mild reinforcement. For design, the values of titanium yield strength and modulus were selected as: $f_{yTi} = 965$ MPa (140 ksi) and $E_{Ti} = 114$ GPa (16,500 ksi), respectively.

7.1.3 Bond Characteristics of Titanium Bars

Bond characteristics of the titanium bars were assessed through ASTM D7913 pull-out tests, ASTM A944 beam-end tests, and concrete prism tension tests. Both, the pull-out and beam-end tests are A-B tests that are best used to evaluate relative performance of reinforcing bars. The nature of reinforcing bar bond to concrete is such that deformed bars exhibited very similar patterns of bond stress-slip behavior. Provided adequate deformations are provided, the bond-slip relationship is dominated by concrete behavior. The bond performance of the titanium bars was similar to that of ASTM A615 steel bars and, as expected, affected by the rib ratio. The results presented reinforce the need to roll deformations such that the ASTM A615-implied lower limit for the rib ratio, $R_r > 0.05$ is satisfied. The implication of a similar bond-stress behavior is that existing bond relationships for steel-reinforced concrete apply to titanium bars provided they meet the deformation requirements of ASTM A615 – the standard for which steel reinforcing bars, and therefore their bond characterization – is calibrated. Both the pull-out and beam-end

test results reinforce the conclusion that bond behavior of titanium bars is essentially the same as that steel bars. The bond stresses, normalized to account for variation in concrete strength, are similar and the calculated development lengths are essentially in the ratio of yield strengths of the materials.

For a given strain in concrete, the resulting deformation is the sum of the crack widths. To ensure good serviceability, ductility and continued adequate bond, it is desirable to have a large number of small cracks. However, crack widths are a function of both bar modulus and bond characteristics. Crack width is proportional to modular ratio ($E_{steel}/E_{titanium}$), while spacing is inversely proportional to the stiffness of the initial bond-slip response. Therefore, a lower modulus bar will exhibit larger crack widths unless bond characteristics are improved proportionally.

Provided the deformations of a titanium reinforcing bar meet the requirements of ASTM A615, the bond behavior is similar to that of steel reinforcement and therefore the development length may be calculated in a similar manner (Eq. 4.2). However, due to lack of data it remains unclear whether the full yield capacity of the titanium can be obtained through conventional straight-bar development. Therefore, in the absence of further data, the stress developed by the titanium bar should be limited to the maximum yield stress for which the current development length equations are calibrated. In the case of Eq. 4.2 [ACI 318], the bar stress should be limited to 550 MPa (80 ksi); this is approximately $0.55f_y$ for the titanium bars considered. This limitation may impact design of titanium reinforced members (see discussion associated with Eq. 7.3, below). The ability of hooked or mechanical anchorages to develop titanium bars has not been studied in this work.

7.1.4 NSM Titanium Reinforcement of Slabs

A pilot study of four near surface mounted (NSM) repairs of highway bridge deck slabs was conducted. To create ‘damaged’ slabs, two of four internal A615 reinforcing bars were cut resulting in a loss of slab capacity of about 50%. The objective of this study was to evaluate the performance of replacing these two cut bars in an attempt to restore the original capacity of the slab. An undamaged specimen, Slab A, reported by McCabe [2013] was used as a ‘control’ specimen. The four Ti NSM-repaired slabs were divided into two groups based on repairs that restore either the capacity ($A_s f_{ys} = A_{Ti} f_{yTi}$) or equivalent stiffness ($A_s E_s = A_{Ti} E_{Ti}$) of the cut bars. One slab from each group was repaired using a full-length straight bar while the other implemented a “staple” type repair, spanning only the location of the cut bars.

Both straight bar repairs and the staple repair based on equivalent stiffness (4 staples) restored the original slab capacity. The repair having the single titanium staple, theoretically sufficient to restore the capacity lost by cutting the internal reinforcement, restored only 94% of the original slab capacity. The slabs having only a single titanium bar, developed ductility similar to the undamaged control Slab A although exhibited significant slip at its ultimate capacity. The slabs having four bars were both effectively over-reinforced leading to increased capacity but decreased ductility. The slab having four full-length titanium NSM bars, failed upon reaching its shear capacity whereas that having four staples failed ‘prematurely’ in flexure at the section at the end of the staples. The staples were not long enough to develop the full theoretical capacity of this slab. It is hypothesized that if the staples had been designed to extend beyond the development length of the cut A615 internal reinforcing bars, the resulting performance of the NSM repairs would have been improved.

7.2 DESIGN OF TITANIUM REINFORCED CONCRETE

A series of benchmark designs comparing comparable reinforced concrete flexural member designs using A615 steel, GFRP and the studied titanium reinforcing bars was presented. It was shown that titanium bars can be designed for ultimate limits states using a strength-based approach (ACI 318-14). This results in required reinforcement being reduced (as compared to steel reinforcement) by the ratio of yield stresses used in design:

$$\rho_{Ti}/\rho_{steel} = f_{ysteel}/f_{yTi} (= 0.42 \text{ in this study}) \quad (7.1)$$

However, due to the lower modulus, deflections at service load levels will be greater. An upper bound on the increase in predicted deflection is given in Eq. 7.2 although the actual value will be less due to the effect of bar stress on the calculation of the effective cracked moment of inertia of the section.

$$\Delta_{Ti}/\Delta_{steel} = E_{steel}f_{yTi}/E_{Ti}f_{ysteel} (= 4.1 \text{ in this study}) \quad (7.2)$$

On the other hand, titanium-reinforced sections can be designed to achieve the same serviceability behavior as steel-reinforced section if the amount on titanium is increased as given in Eq. 7.3. This however results in a significantly over-reinforced section in which the titanium is not efficiently utilized (titanium stress at ultimate capacity will be approximately the inverse of Eq. 7.3). However, due to possible limits on bond behavior described in Section 7.1.3, this ‘inefficiency’ may simply be a limitation of using titanium reinforcing bars.

$$\rho_{Ti}/\rho_{steel} = E_{steel}/E_{Ti} (= 1.76 \text{ in this study}) \quad (7.3)$$

Regardless of design approach, crack control using titanium bars requires that bars be placed closer together to achieve the same degree of crack control. This can lead to designs having a larger number of smaller bars or designs in which larger cracks will be accepted. In

practice (as with the use for GFRP bars) a combination of using more bars and accepting larger crack widths is likely.

7.2.1 Recommendations for ACI 318-compliant design using titanium reinforcing bars

Due to the lower modulus of titanium, the following deviations from ACI 318-14 design equations are suggested when using titanium reinforcing bars:

- 1) The material resistance factor calculation must be revised. Based on the limited data available, the following is proposed although considerably more research and reliability analysis calibration is required to establish appropriate values of the transition strain; arbitrarily selected in this study to be 0.02.

$$\begin{aligned} \phi_f &= 0.65 \text{ for } \varepsilon_{Ti} \leq \varepsilon_{yTi} \\ \phi_f &= 0.90 \text{ for } \varepsilon_{Ti} > 0.02 \end{aligned} \quad (7.4)$$

linear interpolation is permitted between $\varepsilon_{Ti} = \varepsilon_{yTi}$ and $\varepsilon_{Ti} = 0.02$

- 2) Maximum bar spacing, s_{max} , be given by Equation 6.12 (ACI 440.1R-15) which accounts for a tensile modulus different from steel and permits the designer leeway to assign an acceptable crack width, w , which may exceed the ‘default’ value of 0.46 mm (0.018 in.) implicit in the use of Equation 6.11 (ACI 318-14).

$$s_{max} = 29 \frac{E_f w}{f_{fs} k_b} - 2.5 c_c \leq 23 \frac{E_f w}{f_{fs} k_b} \quad (6.12: \text{SI units})$$

$$s_{max} = 1.15 \frac{E_f w}{f_{fs} k_b} - 2.5 c_c \leq 0.92 \frac{E_f w}{f_{fs} k_b} \quad (6.12: \text{US units})$$

- 3) Temperature and shrinkage reinforcement requirements for slabs should be modified as given in Equation 6.14 (ACI 440.1R-15).

$$\rho_{min,TS} = 0.0018 \left(\frac{414}{f_{fu}} \right) \left(\frac{E_s}{E_f} \right) \geq 0.0014 \quad (6.14: \text{SI units})$$

$$\rho_{min,TS} = 0.0018 \left(\frac{60,000}{f_{fu}} \right) \left(\frac{E_s}{E_f} \right) \geq 0.0014 \quad (6.14: \text{US units})$$

- 4) Once again to address the use of lower modulus material that may result in reinforcing ratios significantly different from 0.01, Bischoff's equation (Eq. 6.16) should be adopted for the calculation of effective moment of inertia for titanium-reinforced concrete members (ACI 440.1R-15).

$$I_e = \frac{I_{cr}}{1 - \left(1.72 - 0.72 \left(\frac{M_{cr}}{M_a} \right) \right) \left(\frac{M_{cr}}{M_a} \right)^2 \left[1 - \frac{I_{cr}}{I_g} \right]} \leq I_g \quad (6.16)$$

- 5) Based on the limited research, titanium bars should not be used in fatigue sensitive applications or in seismic applications without considerable further study.

7.2.1.1 NSM Applications

The similarity, in terms of material stiffness and working stress levels (f_{yTi} for titanium and $\kappa_m C_{E} f_{fu}$ for CFRP) suggest that near surface mounted (NSM) titanium bars may be designed in a manner similar to NSM CFRP bars as promulgated in ACI 440.2R-17. Straight NSM titanium deformed bars relying entirely on bond will exhibit very little difference in behavior from comparable CFRP and should be designed similarly. Titanium staples can be used to enhance anchorage and eliminate both the κ_m bond factor and Ψ_f 'FRP strength reduction factor'. While allowing the titanium to be utilized more efficiently, this comes at the cost of greater deflections.

REFERENCES CITED

AASHTO (2017) LRFD Bridge Design Specifications (7th edition), American Association of State Highway and Transportation Officials.

ACI 318-14 *Building Code Requirements for Structural Concrete*, American Concrete Institute

ACI 408.3R-09 *Splice and Development Length of High Relative Rib Area Reinforcing Bars in Tension*, American Concrete Institute.

ACI 440.1R-03 *Guide for the Design and Construction of Structural Concrete Reinforced with FRP Bars*, American Concrete Institute.

ACI 440.1R-06 *Guide for the Design and Construction of Structural Concrete Reinforced with FRP Bars*, American Concrete Institute.

ACI 440.1R-15 *Guide for the Design and Construction of Structural Concrete Reinforced with FRP Bars*, American Concrete Institute.

ACI 440.2R-17 *Design and Construction of Externally Bonded FRP Systems*, American Concrete Institute.

ACI 440.7R-10 *Guide for the Design and Construction of Externally Bonded Fiber-Reinforced Polymer Systems for Strengthening Unreinforced Masonry Structures*, American Concrete Institute.

ACI HB10 (2011) *314 Design Aids*, American Concrete Institute.

ACI SP-17 (2014) *The Reinforced Concrete Design Handbook – A companion to ACI 3187-14*, American Concrete Institute.

Adkins, J., & George, W. (2017). Titanium Finds a Home in Civil Engineering. *Concrete International*, 39(12), 51-55.

Aidoo, J. (2004) *Flexural Retrofit of Reinforced Concrete Bridge Girders Using Three CFRP Systems*, PhD dissertation, University of South Carolina.

Amneus, Barker and Higgins (2014) Flexural Anchorage Strengthening using Near-Surface Mounted Titanium in Reinforced Concrete Deck-Girders (RCDG), *Northwest Transportation Conference*, March 2014.

Askeland, D. R., & Wright, W. J. (2015). *Science and engineering of materials*. Nelson Education.

ASTM A370-14 *Test Methods and Definitions for Mechanical Testing of Steel Products*, ASTM International.

ASTM A615-16 *Standard Specification for Deformed and Plain Carbon-Steel Bars for Concrete Reinforcement*, ASTM International.

ASTM A706-15 *Standard Specification for Deformed and Plain Low-Alloy Steel Bars for Concrete*, ASTM International.

ASTM A944-10 *Standard Test Method for Comparing Bond Strength of Steel Reinforcing Bars to Concrete Using Beam-End Specimens*, ASTM International.

ASTM A1035-16 *Standard Specification for Deformed and Plain, Low-Carbon, Chromium, Steel Bars for Concrete Reinforcement*, ASTM International.

ASTM C39-16 *Standard Test Method for Compressive Strength of Cylindrical Concrete Specimens*, ASTM International.

ASTM C496-11 *Standard Test Method for Splitting Tensile Strength of Cylindrical Concrete Specimens*, ASTM International.

ASTM C876-09 *Corrosion Potentials of Uncoated Reinforcing Steel in Concrete*, ASTM International

ASTM D7913-14 *Standard Test Method for Bond Strength of Fiber-Reinforced Polymer Matrix Composite Bars to Concrete by Pullout Testing*, ASTM International.

ASTM E290-14 *Standard Test Methods for Bend Testing of Material for Ductility*, ASTM International.

ASTM E466-15 *Standard Practice for Conducting Force Controlled Constant Amplitude Axial Fatigue Tests of Metallic Materials*, ASTM International.

ASTM G102-89 *Calculation of Corrosion Rates and Related Information from Electrochemical Measurements*, ASTM International

Atlas Steels (2010) Galvanic Corrosion, Technical Note No. 7. <http://atlassteels.com.au>, accessed April 2016

Benmokrane, B., Chaallal, O., & Masmoudi, R. (1996). Flexural response of concrete beams reinforced with FRP reinforcing bars. *ACI Structural Journal*, 93(1), 46-55.

Bertolini, L., & Pedferri, P. (2002). Laboratory and field experience on the use of stainless steel to improve durability of reinforced concrete.

Bischoff, P. H. (2005). Reevaluation of deflection prediction for concrete beams reinforced with steel and fiber reinforced polymer bars. *Journal of Structural Engineering*, 131(5), 752-767.

Bomberger, H. B., Cambourelis, P. J., & Hutchinson, G. E. (1954). Corrosion properties of titanium in marine environments. *Journal of the Electrochemical Society*, 101(9), 442-447.

Boyer, Howard E. (1986). Atlas of Fatigue Curves. ASM International. Online version available at: <http://app.knovel.com/hotlink/toc/id:kpAFC00001/atlas-fatigue-curves/atlas-fatigue-curves>

Broendby (1999). Corrosion Aspects of Galvanic Coupling Between Carbon Steel and Stainless Steel in Concrete. *Arminox Research and Development Report*, 2007.

Choi, O. C., Hadje-Ghaffari, H., Darwin, D., & McCabe, S. L. (1990). *Bond of epoxy-coated reinforcement to concrete: bar parameters*. University of Kansas Center for Research, Inc.

Clark, A. P. (1946). Comparative bond efficiency of deformed concrete reinforcing bars. *ACI Journal*, 43(4), 381-400.

Clark, A. P. (1949). Bond of Concrete to Reinforcing Bars. *ACI Journal Proceedings* 46(11), 161-184.

Cochrane (1999). Efficient Use of Stainless Steel Reinforcement for Bridge Structure, *Infrastructure Regeneration and Rehabilitation Improving the Quality of Life Through Better Construction: A Vision for the Next Millennium*. (Swamy, editor), R.N. Sheffield Academic Press, Sheffield.

Collins, M. P., & Mitchell, D. (1997). *Prestressed concrete structures*. Toronto: Response Publications.

Cotton, J. B., & Downing, B. P. (1957). Corrosion resistance of titanium to sea water. *Trans. Inst. Marine Eng*, 69(8), 311-320.

CSA S806-12 *Design and construction of building components with fibre-reinforced polymers*, Canadian Standards Association.

Eligehausen, R. (1979). Overlap joints of tensioned ribbed bars with straight bar ends. <http://dx.doi.org/10.18419/opus-656>

EuroCode 2 (EC2) BS-EN 1992 *Design of concrete structures*

Farshadfar, O., Ajaam, A., Hano, M., O'Reilly, M., & Darwin, D. (2014). *Bond Strength of Reinforcing Bars with Deformation Spacings that Exceed Maximum Specified in ASTM A615*. The University of Kansas Center for Research, Inc.

Feldman, L. R., & Bartlett, F. M. (2005). Bond strength variability in pullout specimens with plain reinforcement. *ACI Structural Journal*, 102(6), 860.

Gilbert, R. I. (2006). Discussion of “reevaluation of deflection prediction for concrete beams reinforced with steel and fiber reinforced polymer bars” by Peter H. Bischoff. *Journal of Structural Engineering*, 132(8), 1328-1330.

Gonzalez, J. A., Andrade, C., Alonso, C., & Feliu, S. (1995). Comparison of rates of general corrosion and maximum pitting penetration on concrete embedded steel reinforcement. *Cement and concrete research*, 25(2), 257-264.

Gudonis, E., Kacianauskas, R., Gribniak, V., Weber, A., Jakubovskis, R., & Kaklauskas, G. (2014). Mechanical Properties of the Bond Between GFRP Reinforcing Bars and Concrete. *Mechanics of Composite Materials*, 50(4), 457-466.

Gulikers, J. J. W., & Van Mier, J. G. M. (1992). Accelerated corrosion by patch repairs of reinforced concrete structures. In *Proceedings Int'l. RILEM/CSIRO/ACRA Conference on Rehabilitation of Concrete Structures, Melbourne* (pp. 341-353).

Gulikers and Schlangen (1996). Numerical analysis of galvanic interaction in reinforcement corrosion. *Corrosion of Reinforcement in Concrete Construction* (Page et al., editors), Royal Society of Chemistry.

Helgason, T. and Hanson, J. M. (1974). Investigation of Design Factors Affecting Fatigue Strength of Reinforcing Bars – Statistical Analysis. *Abeles Symposium on Fatigue of Concrete*, ACI SP-41, American Concrete Institute, Detroit, pp 107-138.

Higgins, C., Amneus, D., & Barker, L. (2015). *Methods for Strengthening Reinforced Concrete Bridge Girders Containing Poorly Detailed Flexural Steel Using Near-Surface Mounted Metallics* (No. FHWA-OR-RD-16-02).

Hope (2001). *Some corrosion aspects of stainless steel reinforcement in concrete*. Final report of MTO special project Q900076.

Kasan, J. and Harries, K.A. (2009) Repair of Impact-damaged Prestressed Concrete Bridge Girders with CFRP, *Proceedings of the Asia-Pacific Conference on FRP in Structures* (APFIS 2009), Seoul, December 2009.

Kelly, D. J., Lepage, A., Mar, D., Restrepo, J. I., Sanders, J. C., & Taylor, A. W. (2014). Use of High-Strength Reinforcement for Earthquake-Resistant Concrete Structures. *Proceedings of the 10th National Conference on Earthquake Engineering*. Earthquake Engineering Institute. Anchorage, AK.

Klinghoffer et al. (2000). Practical and Economic Aspects of Application of Austenitic Stainless Steel, AISI 316, as Reinforcement in Concrete. *Corrosion of reinforcement in concrete: corrosion mechanisms and corrosion protection* (Mietz et al., editors).

Knudsen, A., & Skovsgaard, T. (2001). The optimal use of stainless steel reinforcement in concrete structures. In *CONSEC'01: Third International Conference on Concrete Under Severe Conditions* (pp. 1360-1367).

- Laque (1975). *Marine Corrosion: Causes and Prevention*, John Wiley and Sons, 332 pp.
- Lorrain, M. S., Caetano, L. F., Vale Silva, B., Gomes, L. E. S., Barbosa, M. P., & Silva Filho, L. C. P. (2010). Bond strength and rib geometry: a comparative study of the influence of deformation patterns on anchorage bond strength. In *PCI Annual Convention & 3rd International FIB Congress FIB, Washington, D C. Chicago: 3rd FIB International Congress FIB*.
- Maekawa, K., Okamura, H., & Pimanmas, A. (2003). *Non-linear mechanics of reinforced concrete*. CRC Press.
- Martin, H. (1973). Relationship between surface quality, bond and explosive effect of reinforcing steel under short-term loading. *German Committee for Reinforced Concrete*, (228).
- McCabe, M. (2013). *Structural Evaluation of Slab Rehabilitation by Method of Hydrodemolition and Latex Modified Overlay*. (Master's thesis), University of Pittsburgh, PA.
- McCabe, M., Harries, K.A. and Sweriduk, M. (2014). Evaluation of Concrete Bridge Deck Rehabilitation by the Method of Hydrodemolition and Latex-Modified Overlay. *Proceedings of 15th International Conference on Structural Faults and Repair*, London.
- Mousavi, S.R., Esfahani, M.R., & Arabi, M. (n.d.). An Equation for the Effective Moment of Inertia for FRP-Reinforced Concrete Beams. <https://www.iifc.org/>
- Osofero, A. I., Corradi, M., & Borri, A. (2014). Experimental Study of Bond Strength between Titanium Bar and Lime-Based Mortar. *Journal of Materials in Civil Engineering*, 04014182.
- Pérez-Quiroz, J. T., Terán, J., Herrera, M. J., Martínez, M., & Genescá, J. (2008). Assessment of stainless steel reinforcement for concrete structures rehabilitation. *Journal of constructional steel research*, 64(11), 1317-1324.
- Poursaei, A. (2011). Corrosion measurement techniques in steel reinforced concrete. *Journal of ASTM International*, 8(5), 1-15.
- Portland Cement Association (PCA) (1970) Corrosion of Nonferrous Metals in Contact with Concrete, *Modern Concrete*.
- Qu et al. (2003). Effects of galvanic coupling between carbon steel and stainless steel reinforcements. *NRCC 46634, National Research Council of Canada*, 27 pp.
- Rafi, M. M., & Nadjai, A. (2009). Evaluation of ACI 440 deflection model for fiber-reinforced polymer reinforced concrete beams and suggested modification. *ACI Structural Journal*, 106(6), 762.
- Sahamitmongkol, R., & Kishi, T. (2011). Tension stiffening effect and bonding characteristics of chemically prestressed concrete under tension. *Materials and structures*, 44(2), 455-474.

Seibert, P.J. (1998). Galvanic Corrosion Aspects of Stainless and Black Steel Reinforcement in Concrete. (Master's thesis), Queen's University, Kingston, Ontario.

Shahrooz, B.M., Miller, R.A., Harries, K.A. and Russell, H.G. (2011) Design of Concrete Structures Using High-Strength Steel Reinforcement, *NCHRP Report 679*, Transportation Research Board.

Soltani, A., Harries, K. A., & Shahrooz, B. M. (2013). Crack opening behavior of concrete reinforced with high strength reinforcing steel. *International Journal of Concrete Structures and Materials*, 7(4), 253-264.

Song, G., & Shayan, A. (1998). Corrosion of Steel in Concrete: Causes. *Detection and Prediction*.

Soretz, S., & Holzenbein, H. (1979). Influence of rib dimensions of reinforcing bars on bond and bendability. In *Journal Proceedings* (Vol. 76, No. 1, pp. 111-128).

Tepfers, R. (1973). *A theory of bond applied to overlapped tensile reinforcement splices for deformed bars*. Chalmers University of Technology.

Tepfers, R. (1979). Cracking of concrete cover along anchored deformed reinforcing bars. *Magazine of concrete research*, 31(106), 3-12.

Triantafillou, L (2012) Cost Comparison of Corrosion Resistant Reinforcing Steel – Deployment Considerations, *FHWA Office of Infrastructure Research and Development* retrieved 20 August 2015: http://www.dot.state.fl.us/statematerialsoffice/structural/meetings/crrb/12_deployment.pdf

Vos, E. (1983). *Influence of loading rate and radial pressure on bond in reinforced concrete: A numerical and experimental approach* (Doctoral dissertation). TU Delft, Delft University of Technology.

Webster (1997). *A Discussion on Cell Action as It Refers to Steels in Concrete*, COR-97-7810-N. CORRENG Consulting Service Inc., Downsview, Ontario, 1997.

Wight, J., Richart, F., MacGregor, J. (2012). *Reinforced concrete*. Upper Saddle River, N.J.: Pearson Prentice Hall.

Wong, W. (2014) Cost Comparison/Deployment Considerations of Corrosion Resistant Reinforcing Steel. FHWA PowerPoint presentation. [Waider.wong@dot.gov]

Yost, J. R., Gross, S. P., & Dinehart, D. W. (2003). Effective moment of inertia for glass fiber-reinforced polymer-reinforced concrete beams. *Structural Journal*, 100(6), 732-739.